VNIVERSITAT DE VALÈNCIA

FACULTAT DE CIÈNCIES BIOLÒGIQUES
Departament de Biologia Cel·lular, Biologia Funcional i Antropologia Física. BioTECMED

Doctorat en Biomedicina i Biotecnologia

Development of Bioimage Analysis tools for the study of neurogenesis and neurodegeneration

Pau Carrillo Barberà

Directors de la Tesi Doctoral
Isabel Fariñas Gómez
José Fco. Pertusa Grau
Jose Manuel Morante Redolat

València, gener 2021

Dña. Isabel Fariñas Gómez, catedrática de universidad, D. José Francisco Pertusa Grau, titular de universidad, y D. Jose Manuel Morante Redolat, profesor contratado doctor, como directores de la presente tesis, y D. Francisco Pérez Sánchez, titular de universidad, como tutor académico, todos del Departament de Biologia Cel·lular, Biologia Funcional i Antropologia Física y de la ERI en Biotecnologia i Biomedicina (BIOTECMED), de la Facultat de Ciències Biològiques de la Universitat de València,

INFORMAN QUE:

D. Pau Carrillo Barberá, graduado en Biología por la Universitat de València, ha realizado la tesis doctoral titulada "Development of Bioimage Analysis tools for the study of neurogenesis and neurodegeneration", y que hallándose concluida, autorizan su presentación a fin de que pueda ser juzgada por el Tribunal correspondiente para la obtención del grado de Doctor por la Universitat de València.

Y para que conste, en cumplimiento de la legislación, firman el presente informe en Burjassot, a 15 de enero de 2021.

Isabel Fariñas

José F. Pertusa Grau

Jose Manuel Morante Redolat

Francisco Pérez Sánchez (tutor académico)

Este trabajo de Tesis Doctoral ha sido posible gracias a un contrato predoctoral del Programa de Formación de Personal Investigador (FPI) con referencia BES-2015-075399, financiado por el Ministerio de Economía y Competitividad (MINECO) y asociado al proyecto SAF2014-54581-R. La investigación ha sido financiada por los siguientes proyectos de investigación a cargo de Isabel Fariñas:

- 2018 — 2020. Regulación del comportamiento de las células madre neurales por el medio sistémico: el nicho extendido. MINECO (SAF2017-86690-R).
- 2017 — 2021. Efectos directos y remotos de la respuesta inflamatoria sobre las células madre neurales. Generalitat Valenciana (Prometeo de Proyectos de Excelencia, PROMETEO/2017/030).
- 2017 — 2020. RETIC de Terapia Celular. ISCIII (Programa RETICS 2012, RD16/0011/0017). Programa de Investigación Cooperativa.
- 2015 — 2017. Regulación molecular de la quiescencia: células madre neurales. MINECO (SAF2014-54581-R).
- 2014 — 2018. Estudio de células madre en el ámbito de las investigaciones básicas en terapia celular. Fundación Botín-Banco de Santander.
- 2013 — 2017. Efectos del microambiente vascular en las células madre del cerebro adulto Generalitat Valenciana (Prometeo de Proyectos de Excelencia, PROMETEOII/2013/020).
- 2013 — 2016. RETIC de Terapia Celular. Ministerio de Economía y Competitividad/ISCIII (Programa RETICS de Investigación Cooperativa 2012, RD12/0019/0008).
- 2006 — vigente. CIBER en Enfermedades Neurodegenerativas (CIBERNED). ISCIII (Programa de Investigación Cooperativa, CB06/05/0086).

El desarrollo de la tesis doctoral ha incluido la realización de dos estancias en centros extranjeros. La primera en el *MRC Centre for Regenerative Medicine, University of Edinburgh* (Edimburgo, Escocia) de 4 meses de duración financiada por el Ministerio de Ciencia, Innovación y Universidades) y la segunda en el *Instituto de Investigação e Inovação, Universidade do Porto* (Oporto, Portugal) de 2 semanas de duración, financiada por una COST Action (CA15124) de la Red Europea de Analistas de Bioimagen (NEUBIAS).

Parece mentira que por fin acabe esta aventura que he compartido con tantas personas que me es imposible mencionarlas una a una. A pesar de ello, no quiero dejar pasar la oportunidad de agradecer a todas y cada una de ellas el haberme acompañado en este viaje.

Me gustaría comenzar dando las gracias a mis directores, sin los que nada de esto habría sido posible. A Isabel por darme la oportunidad de iniciar este proyecto y por haberme brindado siempre su confianza y su apoyo para hacer un trabajo, como mínimo, poco convencional. A Pepe por haberme introducido en el mundo del análisis de imagen, una senda que jamás me imaginé que acabaría recorriendo pero que ahora ya no podría—y lo más importante, ya no querría—abandonar. A Jose por haberme acogido desde el día que llegué al laboratorio y por haber contado con él no solo como director sino como amigo. No podría haber tenido mejor mentor.

He tenido la suerte de poder llevar a cabo mi trabajo rodeado de personas maravillosas. Por eso quiero dar las gracias a mis compañeros y compañeras de laboratorio por toda la ayuda que he recibido de su parte, pero sobre todo por hacer del laboratorio de Isabel un lugar que rebosa tanta alegría como talento. Hemos pasado grandes momentos juntos dentro y fuera del laboratorio y estoy seguro que todavía nos quedan muchos más por compartir.

Durante mi tesis he realizado dos estancias en las que he aprendido muchísimo, tanto a nivel científico como personal. Quisiera agradecer a Bertrand Vernay y a Anna Williams el haberme dado la oportunidad de pasar una temporada en el Centre for Regenerative Medicine de Edimburgo, donde trabajé codo con codo con Ana Rondelli en una colaboración que forma parte de este trabajo y que sigue en marcha. También quiero dar las gracias a Paula Sampaio y André Maia por haberme invitado a compartir unas semanas con ellos en el Instituto de Investigação e Inovação em Saúde de Oporto.

No puedo acabar esta sección sin antes agradecer a mi familia y mis amigos todo el apoyo y la comprensión que he recibido durante estos años. Sacar adelante un trabajo de este tipo requiere dedicación y ciertos sacrificios que de algún modo u otro afectan a las personas que más quieres. He tenido la fortuna de no recibir otra cosa que cariño y soporte de vuestra parte, por lo que solo puedo daros de nuevo las gracias.

Finalmente, debo hacer una mención especial a Ana Domingo y a Jose, sin la colaboración de los cuales la calidad de este trabajo estaría muy alejada de sus altos estándares de perfección. Desde el contenido al maquetado, pasando por las geniales ilustraciones de Ana, sin duda todo sería mucho menos bien parecido si no hubiese podido contar con su inestimable ayuda.

Table of Contents

List of abbreviations

bFGF	basic fibroblast growth factor
CC	corpus callosum
CLI	command line interface
CNS	central nervous system
CSF	cerebrospinal fluid
cuprizone	bis-cyclohexanone oxaldihydrazone
DL	deep learning
EGF	epidermal growth factor
EM	electron microscopy
EtBr	ethidium bromide
FACS	Fluorescence-Activated Cell Sorting
FS	freeze substitution
GIGO	garbage in garbage out
GIX	GI254023X
GUI	graphical user interface
HPF	high-pressure freezing
ICA-2K	IN Cell Analyzer 2000
IMB	inner myelin boundary
IsoMsIgG	isotype mouse immunoglobulins
LPC	lysophosphatidylcholine
LV	lateral ventricle
MBP	myelin basic protein

ML	machine learning
MMS	Methyl methanesulfonate
MS	Multiple Sclerosis
NaN	not a number
NA	numerical aperture
NB	neuroblast
NcadBlock	N-cadherin blocking antibody GC4
NC-L929	fibroblasts overexpressing N-cadherin
NEUBIAS	Network of European Bioimage Analysts
NSC	neural stem cell
OB	olfactory bulb
OPC	oligodendrocyte precursor cell
OS	operative system
OSI	open source initiative
QC	quality control
RMS	rostral migratory stream
ROI	region of interest
SEZ	subependymal zone
TEM	transmission electron microscope

Introduction

C:73
M:36
Y: 0
K: 0

R: 0
G:152
B:255

1. Image analysis as an emerging essential player in Life Sciences

State-of-the-art microscopes have become a primary source of quantitative data in biological research. Automation and standardisation of image data acquisition have utterly transformed microscopes, once mainly used for descriptive tasks and qualitative analysis. As a result, the data generated is getting bigger and more complex, hampering manual analysis. Besides, spatial and physical factors are gaining importance in the study of the regulation of cellular processes and their functions, hardly assessed without the application of imaging techniques. This has led to the upswing of bioimage analysis. Originated as a specialization of computer vision and image processing, bioimage analysis is a relatively new but growing field, whose chief task is to extract quantitative information from biological images (especially light or electron microscopy) by means of computational methods (Myers *et al.*, 2012; Meijering *et al.*, 2016).

The intrinsic properties of microscopy images make the bioimage analysis challenges different from those faced by other related fields traditionally focused on natural images. For example, in microscopy images the signal-to-noise ratio is often low, the diffraction artefacts might affect the images significantly and the resolution can be a limitation. Additionally, microscopes usually acquire multidimensional images which can combine several features: spatial dimensions (XYZ), time (T) and channels (C). Since automated microscopes are able to capture a large number of fields-of-view (F) from each sample, sometimes these are also considered an additional dimension. Fields-of-view may be isolated patches of the sample or overlapped tiles meant to build a composite view once stitched. Finally, when using multiwell plates, wells (W) may also be considered a dimension. Therefore, within the bioimage analysis field we can distinguish between two classes of big data. On one hand, large but relatively simple image datasets, such as those acquired by means of microscopy-based screening (in its simplest expression, XYFW, though usually XYCFW). On the other hand, datasets of complex multidimensional images, for example those captured by means of spinning disk or the even bigger ones from light-sheet microscopy (in its most complex expression, XYZCTFW).

As mentioned above, such datasets preclude visual analysis so are bound to require automated tools which, otherwise, also enable faster analysis of smaller datasets. Nonetheless, the use of software has a series of advantages beyond the improvement of efficiency. The increase of objectivity and reproducibility are the most remarkable achievements. Additionally, the use of bioimage analysis methods can also lead to unveil subtleties indistinguishable to the naked eye. However, software-based analyses are not devoid of difficulties, especially when visual object identification and manual analyses are

still considered 'the proper standard'. In fact, while software algorithms are impervious to misinterpretations and assumptions often made by our brain, human perception might sometimes easily discriminate what is (still) hard for algorithms. Therefore, fully-automated image analyses protocols require the implementation of control checkpoints to remove ill-quality images and/or inaccurately processed objects. Conversely, semi-automated tools that prompt for user intervention at specific steps in order to refine or amend the software processing are commonly used. Human-supervised protocols give up the fully-unbiased analysis of automated processes in return of an increase in object identification accuracy.

Although there are numerous software packages developed to perform image processing, there are also others specifically built to perform bioimage analysis. Regardless of the aim, both general and specific toolkits might be considered as collections of image processing and analysis algorithms (Miura *et al.*, 2017). An algorithm is a well-defined, unambiguous, finite sequence of instructions which may be given to a computer in order to solve a problem. Algorithm implementations available to be accessed within a software package may be considered as the collection components. It is important to note that a single component is not usually enough to extract meaningful data from biological images. Namely, users nearly always need to combine several algorithms (even from different collections) to solve a bioimage analysis problem. To this aim it is necessary to i) select the appropriate components, ii) fit them together in a purposeful order and iii) rightly accustom their functional parameters. In other words, one needs to build up a unique sequence of assembled algorithms combined with a specific parameter set, thereby obtaining a workflow that takes images as input and generates quantitative information and/or other images as output. As a side note, by definition, a workflow is just a longer algorithm. Also there are components which actually are workflow templates built to solve a common image processing issue.

How components are accessed by users may considerably change between collections (see **Table 1**). Therefore, among the most popular software packages used to analyse bioimages we can mainly distinguish between: i) those that include a graphical user interface (GUI), such as ImageJ (Rueden *et al.*, 2017), CellProfiler (Carpenter *et al.*, 2006; McQuin *et al.*, 2018) or ilastik (Berg *et al.*, 2019), and ii) those whose algorithms have to be accessed by means of a command line interface (CLI), such as Matlab (Higham & Higham, 2016), Python (Van Rossum & Drake, 2009) or R (R Core Team, 2016). Additionally, many bioimage analysis tools allow the use of one or more scripting or programming languages (see **Table 1**). Image processing libraries, such as ImgLib2 (Pietzsch *et al.*, 2012), OpenCV (Bradski, 2000) or VTK (Schroeder, Martin & Lorensen, 2006), are a different kind of collections interfaced for access by means of scripting or

programming in most of the cases. Although the direct use of those libraries by life scientists is unusual, both GUI and CLI can access image processing libraries in their back end, i.e., as a subordinate software which performs a specialized function without being directly accessed by the user. All the bioimage analysis tools previously described are referred to as collections regardless of their different interfaces.

Table 1. Summary of some commonly used bioimage analysis collections.

Software collection	GUI	CLI	Scripting	OS	Scripting Language	License
ImageJ / Fiji	Yes	Yes	Yes	All	ImageJ Macro, Javascript, Jython, JRuby, Beanshell, Groovy, Clojure	Public domain / GPL
CellProfiler	Yes	Yes	Yes	All	Python	BSD-3
ilastik	Yes	Yes	Yes	All	Python	GPL
Matlab	No	Yes	Yes	All	Matlab	Commercial
Python	No	Yes	Yes	All	Python	PSFL
R	No	Yes	Yes	All	R	GPL
OMERO	Yes	Yes	Yes	All	Python	GPL
Huygens	Yes	Yes	Yes	All	TCL	Commercial
Imaris	Yes	No	No	Win, OSX	Matlab	Commercial

GUI (graphical user interface), CLI (command-line interface), OS (operating system), GPL (General Public License), PSFL (Python Software Foundation License), BSD (Berkeley Software Distribution). Table modified from Miura, 2016.

A significant caveat of bioimage analysis is that each research project relying on imaging methods may require its own tailored workflow. On one hand, the underlying biological question to be asked is often unique. On the other hand, even when repeating a former established protocol, the features of the new image dataset might slightly change due to intrinsic experimental variability. It typically requires, at least, the readjustment of the parameters set. Accordingly, experts capable of building workflows from scratch are meant to have solid knowledge of both bioimage analysis concepts and the biological problem to be assessed. It is also important to have an understanding of the instruments and methods used to perform and capture a bioimaging experiment, from sample handling (i.e. culture medium and conditions, fixation process or labelling techniques) to microscope specifications, type of camera sensor and acquisitions settings.

Additionally, in order to assemble components, it is necessary to gain programming skills. Materialised in the creation of NEUBIAS (Network of European Bioimage Analysts), this has required the emergence of a new kind of specialists, known as bioimage analysts, which need to work closely with the other professional communities involved in bioimaging: life scientists, instrumentalists and developers. These new experts, beyond their interdisciplinary knowledge within the bioimaging field, have a central role in setting up workflows to conduct practical bioimage analysis.

During the last decade there have been substantial advances in the establishment of this professional figure. Despite the fact that there is still much to accomplish, reading the Myers' viewpoint from 2012, one realizes how different the situation was a few years ago:

> *"The field is still in its early days, and there is no such thing as a typical bioimage informatician: they are either computer vision experts looking for new problems, classic sequence-based bioinformaticians looking for the new thing or physicists and molecular biologists whose experiments require them to bite the informatics bullet. There are as yet no established large-scale forums for the work, both in terms of meetings and journals. Young people in the field present challenges to established academic evaluation committees. From my perspective, it is very reminiscent of the state of bioinformatics in the early 1980s: the exciting, somewhat chaotic free-for-all that is potentially the birth of something new."*

2. Common steps in bioimage analysis: from components to workflows

Before addressing the basic concepts and strategies of bioimage analysis, it is important to make some considerations about what we could consider "biological samples'' on the bioimage analysis field, i.e., the digital images. The quality of the measurements that can be extracted from an image is highly dependent on the image quality. Therefore, although the image acquisition (digitalization process) is not part of the bioimage analysis workflow, it provides the starting point, the raw data of an image-based experiment. Indeed, the output generated by means of bioimage analysis techniques relies on both experimental design and well-conducted imaging protocols. As synthesized in the Computer Science common concept 'garbage in, garbage out' (GIGO), the quality of the input data restricts the quality of the output data.

It is even more important to take into account how digital images are formed in order to properly understand how they can be manipulated and interpreted. An

initial consideration of chief importance is to acknowledge that the analogue-to-digital conversion involves a transition from a continuous world to a discrete one which implies an inescapable loss of information. For example, when acquiring an image by means of an 8-bit sensor, its range of intensity values will be limited to a 256 greyscale (0-255). The same happens with the space, constricted by the pixel (picture element) size, which determines the image resolution. Consequently, it must be assumed that digital images, and therefore the quantitative information extracted from them, are simplified representations of the infinite analogical world. Nonetheless, it is precisely in the discrete nature of digital images, where the basis of the image processing algorithms lies. A digital image, regardless of the digital-to-analogue conversion that computers perform in order to let us visualize it, is actually composed of an ordered matrix of numbers representing the intensity values of each pixel. Therefore, image processing was only possible after the arrival of digital images, and has been built upon its matrix-based structure.

Recognizing the "objects" that need to be quantified within an image dataset is the cornerstone of most bioimage analysis workflows. In order to do so, the objects must be separated from the background, i.e., the image region irrelevant for the biological question. In many cases, such a task may be intuitively accomplished by the human brain, which easily recognises patterns to categorize the different elements comprising the image. However, objects do not strictly speaking 'exist' in the matrix of numbers that comprise a raw digital image. So, when it comes to making the computer see what we see, one starts to realize the complexity of the problem. There are multiple approaches to quantify the information contained in image data. The most popular implementations in bioimage analysis software follow two philosophies: the filter-based and the machine learning (ML) paradigms. Each approach has its own advantages and caveats, so it will be crucial in determining the capabilities of the different software.

The filter-based paradigm consists in the detection and delineation of objects (e.g., cells, subcellular compartments...) or regions of interest (ROIs) by means of the application of small matrices (filters) which operate locally, taking into account the value of each pixel and their corresponding neighbours. Some examples of typical filtering operations are those used to reduce noise or suppress background, detect edges or sharpen the images. This approach requires prior knowledge on the design of the filtering strategy **(Sbalzarini, 2016)**. The ML paradigm is divided into two main approaches **(Kan, 2017)**. On one hand, supervised ML consists in the training of a classifier to recognise relevant patterns and then use them to classify entire images or sub-image regions (e.g., pixels, objects…) relying on those patterns. In order to train the software, a set of classes has to be pre-defined because the machine learns from those user annotations **(Shamir**

et al., 2010). On the other hand, unsupervised ML does not require neither classes nor classified examples given by the user. Unsupervised learning comprises a wide range of diverse tasks. A typical approach is to use predefined rules to subdivide the data into clusters. However, it has plenty of applications, from outlier detection (Grys *et al.*, 2017) to image restoration (Krull *et al.*, 2020).

On the whole, there is a great diversity of image processing algorithms, as well as varied paradigms and strategies aimed to conduct successful analysis of digital images. Likewise, there are countless biological problems suitable to be approached from a bioimage analysis perspective, aside from a wide range of microscopy techniques to assess them. As a consequence, presenting an ideal workflow which may serve as a model for any microscopy-based analysis is not an easy task. Even so, there are slightly different views of such a workflow (Meijering *et al.*, 2016; Pertusa & Morante-Redolat, 2019), which I have tried to homogenize below.

2.1. Preprocessing

Imaging is not a flawless process, rather the opposite. Any instrument, including optical systems and sensors, are limited by its own error. In fact, bioimage analysis workflows often include preprocessing steps aimed to reduce imaging artefacts. For example, uneven illumination or vignetting is a widely-extended issue, which usually appears as a fading of the illumination intensity as moving away from the centre of the optical axis. Although this is sometimes neglected, there is a typical variation on the illumination from the central to the outlying regions of 10-30 % (Smith *et al.*, 2014). Therefore, a series of methods have been described to address this effect. These algorithms are based on the application of arithmetic operations between the acquired images and correction functions. So the ultimate goal of shading correction techniques is to predict corrected images, an estimation of how the uncorrupted true image should be. The physical process of image formation, relating the true image I_{true} and the acquired image I_{acq}, is typically described by a linear model (Likar *et al.*, 2000; Peng *et al.*, 2017) which comprises a multiplicative term *F* and an additive term *D*.

$$I_{acq}(x,y) = I_{true}(x,y) \times F(x,y) + D(x,y)$$

F is a representation of the effective illumination variation across I_{acq}, which is known as flat-field. *D* is mainly due to the offset of the camera sensor and the thermal noise and is known as dark-field, due to its independence from the incident light, its effect is not as severe as the one resulting from the flat-field. A corrected image I_{corr} can be calculated inverting the image formation model after obtaining an estimation of the

flat-field F_{est} and the dark-field D_{est}.

$$I_{corr}(x,y) = I_{acq}(x,y) - \frac{D_{est}(x,y)}{F_{est}(x,y)}$$

Alternatively, correction functions may be used to identify image subregions with higher variations in effective illumination to discard them from the quantitative analysis (Jost & Waters, 2019). Depending on how these correction functions are predicted, we can distinguish between two main strategies for illumination correction: prospective methods and retrospective methods (Peng *et al.*, 2017; Caicedo *et al.*, 2017).

Prospective methods are based on the use of reference images, acquired throughout the same imaging system as the experimental dataset, to build the correction function. It may be accomplished acquiring flat-field images with no samples in the foreground. It is also possible to generate dark-field images with no light reaching the camera (Model, 2014; Singh *et al.*, 2014).

Retrospective methods build correction functions directly from the images acquired for the experiment, then leaving aside the additional effort of acquiring reference images throughout the imaging process. Among the retrospective methods we find two major approaches. On one hand, retrospective single-image methods compute a correction function for each image (Likar *et al.*, 2000; Babaloukas *et al.*, 2011). Since this approach generates diverse correction functions from image to image, it is especially useful when analysing datasets where the illumination pattern differs between images. On the other hand, retrospective multi-image methods may be deployed when batch processing an image dataset with a similar illumination pattern. This strategy takes advantage of the dataset size to compute a correction function which may be applied as a constant for the whole dataset (Singh *et al.*, 2014; Smith *et al.*, 2015; Peng *et al.*, 2017).

Another prominent example of image restoration is deconvolution, applied to enhance the blurring introduced by the diffraction limit of any optical system (Lauterbach, 2012; Hernández Candia & Gutiérrez-Medina, 2014). Time-lapse imaging may generate intensity artefacts as well. Lasting laser exposure may cause photobleaching, thus showing a baseline drift over time (Peng *et al.*, 2017). Moreover, the enhancement of the image contrast is a standard step, in this case by adjusting the image histogram. Due to its popularity, most of the image analysis software collections include an implemented function to normalize the histogram. Likewise, images are often pre-processed applying operations on the frequency domain.

Image quality control is a critical pre-processing step in imaging experiments precluding visual inspection, such as microscopy-based screenings. As already

mentioned, according to the GIGO concept, analysing ill-quality images will only generate ill-quality results. Therefore, a series of metrics for ill-quality image detection have been described. The most widely used metrics are focused on the detection of blurring and saturated artefacts (Bray *et al.*, 2012; Caicedo *et al.*, 2017). Blurring is typically found on out-of-focus images, e.g., due to an occasional failure of the autofocus algorithms commonly applied by automated microscopes. There are metrics commonly used to detect blurring: i) the ratio of the mean to the standard deviation of the image intensity, or inverse coefficient of variation (Bray *et al.*, 2012); the normalized variance of the intensity (Groen, Young & Ligthart, 1985); the image correlation (Haralick, 1979); and the power log-log slope (Field & Brady, 1997). Loss of the dynamic range, also known as clipping, must be avoided throughout the imaging process. Clipping causes an irreclaimable loss of the photon detection linearity, inevitably avoiding the quantification of fluorescence intensities. Saturation, caused by the limited capacity of camera sensors to accumulate photons, is the most prominent example of this effect. Once reached the maximum capacity of the sensor, newly arrived photons cannot be detected (Waters, 2009). Therefore, imaging set up must pursue the maximum use of the dynamic range while avoiding saturation (Brown, 2007). Assuming this has been accomplished, the detection of saturated pixels is most probably due to the presence of debris or aggregations as a consequence of the sample preparation process. Since such artefacts are often outstandingly bright, their presence may be revealed by looking for saturated pixels. Indeed, the percentage of saturated pixels is a simple metric which has shown to be the best option for the detection of saturation artefacts (Caicedo *et al.*, 2017).

Registration is also a frequently used method when initialising a workflow. It is defined as a process to map the spatio-temporal coordinates of each image to another (or to a model). It allows the use of the same coordinates system even for samples obtained from different sensors, specimens, time points… thus allowing its comparison through data analysis or visualization (Qu, Long & Peng, 2015). As automated microscopes enable the acquisition of large areas (e.g. for whole slide imaging), it may be the case that all the obtained tiles need to be overlapped in order to obtain a single image as output. This process, known as stitching, is usually preceded by a registration step aimed to enable a meaningful reconstruction. During registration, the multi-tile experiment set is sorted, establishing the spatial relation between the images to facilitate the prediction of the overlapping coordinates (Preibisch, Saalfeld & Tomancak, 2009).

2.2. Detection

At this point, the application of filters based on matrices is a common step aimed to reveal the presence of the objects of interest for the analysis (see **Figure 1**). The goal is to enhance or reduce image features to facilitate the subsequent segmentation step, when the different components of the image will be actually split from the background (Meijering e t al., 2016). Unlike point operations, which are equally and simultaneously applied to all the pixels in the image (e.g., arithmetic operations on an image or between images), filters are applied to each of the pixels in the image and yield a different result for each of them. This is because filtering implies the use of smaller matrices (or kernels) that delimit the number of neighbour pixels that will be included in the operation and, hence, will affect the output. Kernels may have any size, though quadratic filters are typically used to keep symmetry. It is also common, although not compulsory, to use odd numbers (e.g., 3x3, 5x5, 7x7…) in order to avoid interpolations. Filters are iteratively applied to each pixel as the kernel moves across the image. This approach generates smaller images, as certain pixels placed on the image edges cannot be computed according to the matrix due to the lack of some neighbours. Actually, in order to keep the original size, the missing pixels are usually added to the filtered images by means of

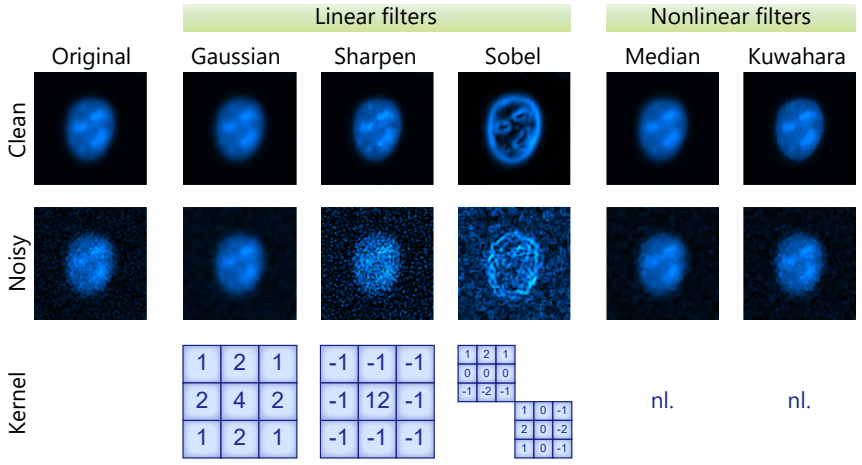

Figure 1. Effect of diverse 3x3 linear and nonlinear (nl.) filters on a nuclear counterstain image. Fiji's Gaussian, Sharpen (a variation of the Laplacian), Find Edges (Sobel), Median and Kuwahara filters were tested on a crop of a DAPI-stained nucleus, both the raw image (Clean) and after artificially adding Gaussian noise (standard deviation of 10) by applying the Add Specified Noise plugin (Noisy). For the Sobel filter, both kernels are used to generate vertical and horizontal derivatives and the final image is calculated as the square root of the sum of the squares.

different correction methods. However, one must be careful when it comes to interpret these peripheral pixels.

There are different ways to classify filter types. The most common distinction is between linear and nonlinear filters. Linear filters transform the input image applying linear combinations of the neighbouring pixels and the kernel values: first, the product of each kernel coefficient and the value of the pixel placed on its corresponding position is calculated; second, the value of the evaluated pixel is obtained as the weighted average of the products. Non-linear filters perform nonlinear operations with the neighbouring pixels such as sorting their pixel values to return the median, the maximum or the minimum values. These are known as the median, maximum and minimum filters, respectively **(Sbalzarini, 2016; Pertusa & Morante-Redolat, 2019)**. Please note that filtering is a handy strategy which is not only used for detection. Indeed, image-filtering techniques may be applied for diverse tasks beyond detection including preprocessing steps (e.g., deconvolution) and segmentation techniques.

Smoothing structures is a commonly used step for detection, especially in images with a low signal-to-noise ratio. Likely, such filters may be quite useful on relatively simple images, where there are clearly bright objects over a dark background or vice versa. Mean and Gaussian are prominent linear filters to smooth images. On one hand, the mean filter is the result of the weighted average of the neighbouring pixels, i.e., all the matrix coefficients of the kernel are equal to one. Conversely, in the Gaussian filter the central pixel has a higher weight, while neighbouring pixels take different values depending on their distance from the central pixel. These filters blur the image, reducing noise but also distorting edges. Median filter is a non-linear filter really effective removing random spot noise that, additionally, preserves the edges much better than the smoothing linear filters. Moreover, smoothing filters larger than the objects to be detected may be applied to calculate and subtract the image background. There are more complex nonlinear filters aimed to reduce the image noise preserving the edges, such as the Kuwahara filter **(Kuwahara *et al.*, 1976 Bartyzel, 2016)** or the anisotropic diffusion **(Perona & Malik, 1990)**.

There are also filters for edge detection, i.e., the transition from a dark region to a bright region, or vice versa. The Sobel operator is one of the most popular edge detectors. It uses two asymmetric, differently oriented, 3x3 kernels which look for strong changes on the first derivative, i.e., the gradients of the intensity function, on x- and y-direction. Moreover, in order to avoid noise interference, these kernels combine the differencing function along one axis with smoothing along the other one. The resulting images represent the horizontal gradient (G_x) and the vertical gradient (G_y), which must

be combined to obtain the gradient magnitude (G) at each point of the image. It is calculated as the square root of the sum of the derivatives squares:

$$G = \sqrt{G_X{}^2 + G_Y{}^2}$$

Actually, the Sobel operator uses the same kernels as the Prewitt operator, just doubling the value of the four direct neighbours of the central pixel. Laplacians are second-order edge detectors as they apply the second-order differencing, which can be estimated as the difference between two contiguous first-order differences. Basically, it is accomplished by computing the difference between the central pixel and the average of its four direct neighbours. Alternatively, it computes the difference between the central pixel and the average of all its eight neighbours, including those on the corners. The effect is a sharpened image, although Laplacian filters are also more susceptible to noise, as they contain no smoothing. Consequently, Gaussian smoothing is often incorporated to obtain the Laplacian of Gaussian (LoG) operator (Nixon & Aguado, 2012). It is also possible to detect different objects by means of their irregular textures, for what a wide catalogue of methods has been described (Di Cataldo & Ficarra, 2017). Whereas some workflows rely on a few filters to perform detection (or even none), some ML approaches use a large amount of them as features to train a classifier (Arganda-Carreras *et al.*, 2017; Berg *et al.*, 2019).

2.3. Segmentation

Arguably, the most challenging step in image analysis is segmentation, which consists in the partition of a digital image into different regions or segments. We can distinguish between two types of segmentation. On the one hand, semantic segmentation consists of assigning different classes to pixels. For instance, a typical fluorescent microscopy image can be segmented to distinguish between 'nucleus', 'cytoplasm' or 'background' pixels. However, this approach is not suitable to delineate the objects on the image since, following the same example, semantic segmentation can determine if a pixel belongs to a cell or to the background, but may not identify the different cells on the image as independent objects. In order to achieve this, instance segmentation goes further, allocating each pixel to the object instance it belongs to (see **Figure 2**). We can distinguish two main strategies to perform instance segmentation. On the one hand, the bottom-up approach consists of performing an initial semantic segmentation which is then used to group the selected pixels to form objects. On the other hand, the top-down approach first predicts bounding boxes containing individual objects which are then submitted to a semantic segmentation in order to define the object boundaries (Borenstein & Ullman, 2008).

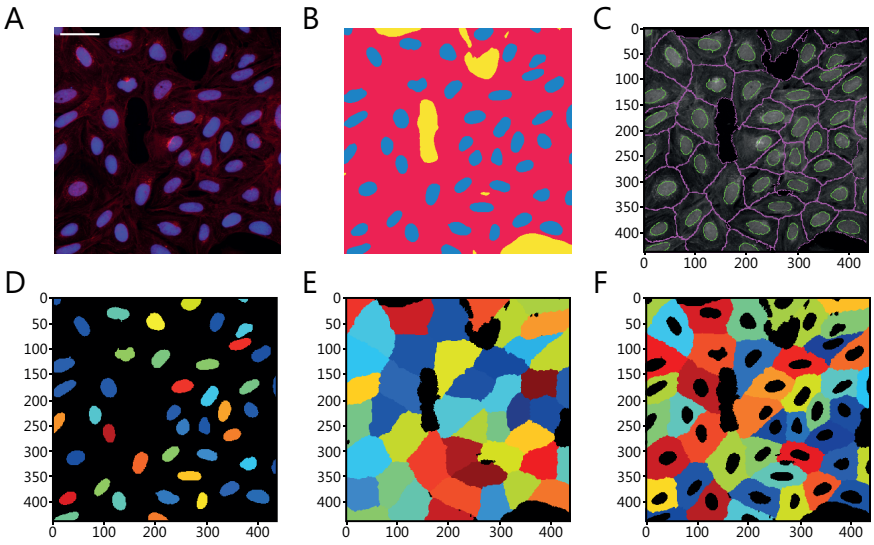

Figure 2. Semantic and instance segmentation. (A) Cells labelled with Hoechst 33342 (nuclei, blue), phalloidin (F-actin, red) and wheat germ agglutinin (WGA; Golgi apparatus and plasma membrane, red). Scale bar 50 µm. **(B)** Semantic segmentation of nucleus (blue), cytoplasm (red) and background (yellow) pixels performed in ilastik (Berg *et al.*, 2019). **(C)** Nuclei and cell outlines. (D-F) Instance segmentations of nuclei **(D)**, cells **(E)** and cytoplasms **(F)** performed in CellProfiler (Carpenter *et al.*, 2006; McQuin *et al.*, 2018). The segmentation output is represented as labelled images, where each object (instance) is represented with a different colour. For the example we used the image set BBBC022v1 (Gustafsdottir *et al.*, 2013), available from the Broad Bioimage Benchmark Collection (Ljosa, Sokolnicki & Carpenter, 2012).

Therefore, semantic segmentation is a crucial step in most of the bioimage analysis workflows, either following a bottom-up approach or applying a top-down strategy. One of the most popular methods to compute semantic segmentation on images is thresholding. This technique consists in the establishment of one or more threshold values among the image greyscale range, so pixels of interest are segmented from background pixels (Pertusa & Morante-Redolat, 2019). These values can be determined either manually or by means of dedicated algorithms, such as the famous Otsu (Otsu, 1979), which is based on minimizing the intra-class intensity variance. Bioimage analysis collections usually include a variety of methods to establish the threshold value based on the image histogram (Tajima & Kato, 2011). This approach is especially useful to find bright objects over a dark background, or vice versa. Other examples of methods to perform semantic segmentation are clustering (Zheng *et al.*, 2018) or pixel classification (Berg *et al.*, 2019). These methods are mainly based on the similarity between the greyscale values of pixels (pixel classification to a lesser extent), which can be severely affected during the pre-processing and detection steps.

Typically, the ultimate output of a segmentation process is a binary image. Also known as binary mask, it consists of a representation of the original image where the pixels of interest take the value 1 whereas the background pixels take the value 0. Alternatively, an instance segmentation process can generate a labelled image, where background pixels are labelled with 0 whereas each object instance is labelled with a different integer. Both binary and labelled images can be easily computed to quantify object features, such as those described on the next section. However, segmented images may still require to be corrected before proceeding to a quantification step. For example, since bottom-up approaches neglect whether a pixel is part of an object or not, they usually generate a certain amount of small, isolated objects which actually consist of background noise. Other typical mistakes are the segmentation of objects with holes, merging different objects into a single instance or, conversely, splitting single objects into diverse particles. These and other segmentation errors can lead to a biased result. Therefore, a series of methods can be applied on the binary mask to minimize the error.

Due to their binary nature, masks can be easily computed to enhance the segmentation output applying nonlinear operations by means of a series of techniques known as mathematical morphology (Serra, 1986). Erosion and dilation are common operations which modify the size of the objects. These operations can be combined to apply open or close operations, leading, e.g., to split or merge objects while avoiding severe effects on their size. In addition, watershed is a classic algorithm widely used to separate merged objects. The name is not accidental; the strategy emulates a flood filling a concave surface. It starts from specific markers on the objects, which can be determined by means of different methods. For example, to separate convex, overlapping objects it is common to iteratively erode the objects and use the ultimate eroded points as markers. Another typical approach is to use local maxima or minima (from the greyscale image). From these markers, the flood grows (dilates) until it reaches the object edge or the flood generated from a different marker, which causes the object partition. A different class of operations used to process binary images are the logical or Boolean operators. In this case, operations are applied between two binary images (i.e., AND, OR). A useful application of logical operators is to obtain the actual objects of interest by comparing intermediate segmentation results.

2.4. Feature extraction

Once objects have been segmented, the extraction of features (i.e., the quantitative information needed to solve the biological problem) is a straightforward step. There are plenty of quantitative descriptors to represent the object properties and that constitute

the raw information for the data analysis (Rodenacker & Bengtsson, 2003; Ferreira & Rasband, 2012). Some of the most common are morphometric, densitometric and texture features.

Morphometric features describe the size and shape of the objects as they are computed on the boundaries of the segmented particles. Therefore, morphometric quantification only requires the object mask but not a greyscale image. Size quantification includes basic metrics such as area or perimeter. Another examples of metrics which care about size are the major and minor axis of the fitting ellipse or the Feret's diameter, defined as the distance between two parallel tangents on opposed borders of a randomly oriented object. It is usual to keep just the maximum Feret's diameter (also known as maximum calliper), i.e., the longest distance between any two points along the object borderline. In some analysis, it may be very useful to obtain metrics based on the object topological skeleton, i.e., the medial axis of the objects obtained by applying mathematical morphology operations to iteratively remove pixels on the binary mask edges until objects are reduced to single-pixel-wide shapes. Once skeletonized, it is possible to compute metrics such as the number of end-points, the number and type of junctions (double, triple…), the count and length of individual branches or the Euclidean distance between end-points (Arganda-Carreras *et al.*, 2010). Shape descriptors are also powerful in morphometric analyses (Chaki & Dei, 2020). Some notorious examples of widely used shape descriptors are circularity, aspect ratio or solidity.

Circularity, *C*, is based on the idea that the circle is the most compact object. As a matter of fact, the circle is the geometrical figure which may enclose the bigger area *A* for any given perimeter *P*. This shape descriptor is a dimensionless comparison between area and perimeter which is equal to one for a circle (taking into account that a circle has an area of $\pi r2$ and a perimeter of $2\pi r$, where *r* is the radius), while it becomes smaller for less compact objects.

$$C = 4\pi \times \frac{A}{P^2}$$

Aspect Ratio, *AR*, is a measure of the elongation which is obtained from the fitted ellipse of the object. It is defined as the ratio of the major axis (*MA*) to the minor axis (*ma*). Thus, this relation is equal to one when a fitting ellipse is as high as its wide (i.e., a circle), and it becomes greater as the ellipse stretches.

$$AR = \frac{MA}{ma}$$

Solidity, *S*, allows to determine how much convex or concave an object is. It is calculated as the ratio of the object area *A* to its convex hull area A_{CH}. The convex hull

area is computed by the gift wrap algorithm (Jarvis, 1973). To visualize the convex hull of an object, one can imagine a rubber band tightly attached to the object, wrapping around its boundaries. A_{CH} from an already convex object is equal to *A*, hence solidity reaches its maximum value of one. The more concave the object, the less solidity.

$$S = \frac{A}{A_{CH}}$$

Densitometric features are intensity-based. Indeed, the absolute intensity values are decisive for densitometric analysis, so it is important to obtain measurements as standardised and normalised as possible. These include statistics which may be computed from the image histogram such as mean, median, maximum and minimum, mode, standard deviation, variance, skewness and kurtosis. Additionally, the integrated density sums the values of all the pixels forming the object. Likewise, the centre of mass is a descriptor which should not be confused with the centroid, as it is calculated as the brightness-weighted average of the x and y coordinates of all the pixels in an object. Sometimes densitometric measurements may be restricted to subregions of the objects, e.g., differentiating the inside border zone from the rest of the object. It is also common to compute intensity metrics from the outside border zone of the objects. It may be easily accomplished applying dilation or erosion operations.

Texture features comprehend a series of diverse metrics which try to measure the appearance and feel which suggests the vision of any surface (e.g., its smoothness or roughness). They are based on the patterns of intensities within the objects, i.e., the spatial arrangements between different types of pixels. Indeed, sometimes objects are more eminent by their texture than by their borders. As the relation between two or more pixels at a time needs to be computed, most texture analysis methods use higher-order statistics. Haralick texture features are widely used. These are based on the use of grey level co-occurrence matrices (GLCM) and include metrics such as correlation or entropy (Haralick, Shanmugam & Dinstein, 1973; Löfstedt *et al.*, 2019). Gabor filters are also typically used to assess image textures (Clausi & Ed Jernigan, 2000).

Additionally, it may be sometimes interesting to obtain context features, which depict spatial relationships between objects and other metrics describing their microenvironment. Some population context features are local cell density, population size, distance between neighbours or position within the cell colony, e.g., distance from cell-colony edge (Snijder *et al.*, 2009; Snijder *et al.*, 2012).

2.5. Data analysis

Once quantification has been performed, it may be considered that the bioimage analysis workflow is done since the sought quantitative data has already been extracted from the biological images comprising the experimental dataset. Nonetheless, data analysis is to be performed in order to finally answer the biological question. It is possible to directly carry out the statistical processing of the extracted data. However, an alternative option is to compute a large number of descriptors in order to classify the objects by means of pattern recognition methods. This approach is commonly used in high-content screening assays (Bray *et al.*, 2016). Bioimage analysis workflows may also include an object-level quality control based on the quantification output. Some issues that may prevent the inclusion of objects in the data analysis are, e.g., inaccurate segmentations or errors derived from sample preparation such as staining artefacts. Object quality control is often based on outlier detection. However, it may also be a dangerous approach, as it is possible to end up removing data representing interesting samples, such as minority cell phenotypes (Caicedo *et al.*, 2017).

2.6. Other common steps

Live cell imaging is becoming a common approach to assess complex biological problems. In such experiments, in addition to the segmentation, a tracking step is necessary. At this stage, each moving object must be interrelated between frames in order to determine their trajectories and, in that way, perform a meaningful extraction of quantitative data and even lineage reconstruction (Tinevez *et al.*, 2017; Wolff *et al.*, 2018). Regarding semi-automated workflows, human supervision is required at some steps. In such cases, users can interactively visualize the output in order to inspect and correct it when necessary. Actually, there are workflows whose main goal is just to visualize the image dataset, rather than to obtain quantitative information. Annotation, an essential step to train pattern recognition models, is often performed manually by experts, and therefore may also depend on visualization (Bankhead *et al.*, 2017). Basically, annotation consists of labelling instances, e.g., images or objects. A common application of annotation is to assign classes in order to feed a supervised ML algorithm.

3. Microscopy-based screening: the paradigm of bioimaging automation

The evolution of microscopy hardware, e.g., inclusion of auto-focus or motorized plate positioning, along with the advances on bioimage analysis software has led to major advances on imaging automation. About 20 years ago, this process of microscopy 'industrialization' crystallized with the birth of the image-based screening field (Taylor, Woo & Giuliano, 2001), mainly focused on the automated study of cells. For example, the identification of cell phenotypes or the understanding of molecular processes such as gene regulation have been addressed by means of these methods (Boutros, Heigwer & Laufer, 2015; Mattiazzi Usaj *et al.*, 2016). Nowadays, cell-based assays are routinely used to screen large libraries of small molecules, assess RNA interference or evaluate genetic perturbations, among many others. Indeed, these methods are especially associated with the biopharma industry due to its utility for the identification of potential drug candidates. However, microscopy-based screening is also used to assess a wide spectrum of biological questions such as the identification of stem cell markers, gene functions, differentiation pathways… As a matter of fact, the field is no longer limited to a 'cell-centric' perspective, as it has been adapted to other imaging modalities such as light-sheet microscopy for the study of more complex specimens, e.g., 3D cell culture models (i.e., organoids and spheroids) or tissues (Li *et al.*, 2016; Glaser *et al.*, 2019; Eismann *et al.*, 2020).

Microscopy-based screening techniques can be subdivided into two main classes (Boutros, Heigwer & Laufer, 2015). On the one hand, high-throughput screening experiments are generally limited to the quantification of a single metric on a large amount of samples. The typical readout of a high-throughput screening is a fluorescent signal resultant from, e.g., the expression of a reporter gene, the binding of small molecules or an enzymatic reaction. Despite being cell-based, high-throughput measurements are typically averaged over all cells for each microplate well. Therefore, since no complex bioimage analysis is needed it can be performed on-the-fly. On the other hand, high-content screening relies on a larger number of measurements to identify different phenotypes in individual cells. For example, these analyses often include both densitometry and morphometry data either from cells or from one or more sub-cellular compartments. Additionally, many other features can be extracted from each individual cell. As a consequence, the bioimage analysis step of such assays becomes a complex process so it is typically decoupled from image acquisition. Additionally, the wealth of the data obtained has led to the combination of high-content imaging with ML methods in order to look for deeper patterns within the samples. Indeed, the improvement of high-content imaging methods has required novel bioimage data analysis approaches

(Bray *et al.*, 2016; Caicedo *et al.*, 2017).

In order to improve the throughput of the assay, high-content microscopes often include their own bioimage analysis software. These collections usually include predefined workflows for the analysis of typical high-content imaging assays that, in some cases, can even be coupled to the image acquisition process. All these features aim to provide a quick and straightforward analysis. Naturally, these tools are programmed to recognise the image formats generated by their corresponding high-content microscope, a built-in process which becomes an additional step when using any other bioimage analysis collection. However, the system also has its limitations. As a proprietary software, it is not usually open-source. Therefore, the possibility of deploying customized workflows to assess a specific biological question is quite restricted, if available. Moreover, the use of such software is often restricted to a single workstation. Even when purchasing several licenses for its use on different computers, this may lead to overbooking issues. This may interfere even with the image acquisition, since both microscope and image analysis software are usually installed on the same workstation. As a consequence, we decided to create open-source software adapted to our scientific needs and suited for the image format generated by the high-content imaging system available on our imaging facility.

4. Open-source software for bioimage analysis

There is a wide range of software packages available to analyse bioimages (Eliceiri *et al.*, 2012; Miura *et al.*, 2016). To overview all of them is an overwhelming effort which is beyond the scope of this work. For this reason, just the main collections applied throughout the course of this thesis are presented below. Please note that this work has been carried on using exclusively free, open-source software. The fundamental basis of the open-source software is that its code is publicly available, which perfectly fits with gold standards of science such as the scientific method and the validation of results throughout a peer review system. Indeed, transparency is one of the layers of the Open Source Initiative (OSI) model, formed in 1998 for the promotion of collaborative software development. Another important founding principles are affordability (allowing end users to be independent of commercial software), flexibility (making possible the enhancement of the code by an entity other than the original developer, even its maintenance in order to ensure its perpetuity) or security (users may fully understand the code and its functionality). A relevant factor for the present thesis is that the open-source approach advocates for interoperability, i.e., enables to develop interfaces for

communication between different software (Guiet, Burri & Seitz, 2019), enabling the combination of components from different collections.

Nonetheless, it does not mean that the use of commercial software should be avoided since it sometimes provides unique solutions. Besides, it is increasingly common for the companies to bundle its own bioimage analysis software within microscopes, which can be interesting for some applications. However, it is important to make some considerations. The proprietary, opaque nature of the code opposes elementary principles of science, as it prevents researchers from knowing how their data are actually analysed. The commercial approach also limits scientists from modifying the strategy of the algorithms composing the collection, bracketing its potential development. For all this, as I stated before, this thesis is based on the use of free, open-source, bioimage analysis software.

4.1. Fiji is (not) just ImageJ

ImageJ (Schneider, Rasband & Eliceiri, 2012) is one of the most popular software for scientific image analysis. This old-timer software has remained faithful to the philosophy of its original creator over more than two decades: to be an affordable image analysis software for any average bench scientist and to enable its deployment by the users themselves. This is how, from Wayne Rasband's hands, NIH Image was born at the US National Institutes of Health (NIH) in 1987. However, NIH was limited to the Mac operating system. After the creation of Java (1995), an operating-system-agnostic platform, Rasband started a conversion from NIH Image to ImageJ (the 'J' was added after its new Java foundation).

Since then, ImageJ has become a widely used program in life sciences, amongst many other fields. This is not surprising given the long list of benefits of using ImageJ: is free, open-source, easily installable in the main operating systems, it has an easy-to-use GUI and an extensible plugin architecture to add functionality, besides a macro language whose commands are even recordable, all of this combined with advanced image analysis solutions. It has allowed contributions coming from professional developers to users with no programming experience at all. Indeed, ImageJ was mostly developed by scientists for scientists. At a certain point, however, it became a technical limitation, since the architecture of ImageJ was not built over up-to-date software-engineering principles, which could preclude handling the requirements to support modern imaging paradigms. Moreover, in spite of the many advantages of the ImageJ ecosystem, it also promoted the overpopulation and redundancy of plugins.

Fiji (Fiji is just ImageJ) was born as a distribution of ImageJ focused on bioimage analysis, a new open-source project to deal with the limitations mentioned above (Schindelin *et al.*, 2012). Fiji maintains compatibility with ImageJ and an identical GUI, while the new project updates the original architecture using modern software engineering practices. Thus, Fiji adds functionality in order to make the system more attractive for computer scientists which may develop solutions for cutting-edge image analysis. Indeed, Fiji supports a broad range of scripting languages (Jython, Clojure, Javascript, JRuby and Beanshell). Moreover, it incorporates a series of organized softer libraries (e.g., ImgLib, ITK/VTK, VIGRA…) to allow a rapid transformation of newly described algorithms into implementations to conduct practical bioimage analysis. Fiji also incorporates a curated selection of plugins for specific bioimage analysis tasks. Furthermore, anybody can add their plugins, libraries or scripts to the Fiji source code and the code is reviewed for its curation and integration within the Fiji package. Besides, it is also possible to provide new tools to the Fiji community through a secondary update site. For example, research groups can set up their own update site, allowing users to customize a Fiji installation suited to their bioimage analysis requirements by selecting the secondary update sites of their interest. Indeed, all the Fiji tools implemented on this work are provided throughout the NeuroMol Lab update site.

Fiji has a robust, straightforward distribution system, designed to ensure that any change on the source code or the Fiji update sites reaches its users worldwide by means of the Fiji Updater. The software is refined thanks to the fluent feedback from users and other developers. As a matter of fact, the Fiji project accentuates the importance of the communication between the different parts of its interdisciplinary ecosystem, promoting collaboration between computer and life scientists to solve biological questions by means of practical bioimage analysis, as well as emphasising the importance of extensive documentation of the installation, maintenance, programming and usage of the software (https://fiji.sc/). Last but not least, as an open-source project, Fiji aims to interconnect with other bioimage analysis collections that may outpace Fiji on an arbitrary task. For example, there are interfaces to integrate Fiji with Matlab or ilastik. Fiji became the outer, application-oriented layer of a very close project, ImageJ2 (Rueden *et al.*, 2017).

4. 2. CellProfiler and CellProfiler Analyst

CellProfiler (Carpenter *et al.*, 2006) was initially developed for high-content analysis from microscopy-based screening datasets to identify cell phenotypes, as its

name suggests. Therefore, it has been constructed to easily batch process thousands of images, though it is also used for smaller-scale projects. Subsequent versions added new analysis methods, e.g., for cell tracking, measuring neurons, worms or tissue samples, analysing 3D stacks… (Kamentsky *et al.*, 2011; McQuin *et al.*, 2018). Originally, CellProfiler was implemented in MATLAB but later on rewritten in Python. Since its inception, it was designed to offer a modular approach to build bioimage analysis workflows, known as pipelines among the CellProfiler community. To assemble a pipeline, one just has to sort individual modules to process images in a sequential order. CellProfiler modules do not reach a hundred, which have been carefully curated before its inclusion in the collection. These modules and its settings are limited, avoiding superposition of functionalities in an attempt to not overwhelm users. Most of these modules are templates of image processing algorithms designed to fulfil a particular function. For example, nuclei segmentation is often performed looking at them as primary objects, i.e., objects that can be identified without relying on another object type as a reference. The module intended for such a task includes a series of settings to perform the segmentation, e.g., thresholding and watershed methods, options for object size selection or exclusion of the objects touching the edges… Classic secondary objects are cells, typically much more clumped than nuclei, so taking as a reference its corresponding nuclei eases its instance segmentation. CellProfiler includes many other components for advanced image processing, from illumination correction to feature extraction modules. Additionally, CellProfiler provides an interactive, straightforward test mode to assess how the pipeline is performing throughout its arrangement. It is possible to activate/deactivate the pipeline modules, adjust settings and check the output on selected images. Indeed, researchers can also customize which intermediate results they wish to visualize, checking the pipeline step by step. This, combined with its extensive documentation (https://cellprofiler.org/) and an intuitive GUI, makes CellProfiler a powerful, easy-to-use collection, even for non-programmers.

Analysis and exploration of data generated through a CellProfiler pipeline is a challenging task, due to the wealth of cytometry data that can be extracted from an image-based screening. As a consequence, CellProfiler Analyst (Jones *et al.*, 2008) was born as a companion software for CellProfiler. Thus, CellProfiler Analyst includes tools for data visualization, such as histograms or scatter plots, and to explore relations among data, such as brushing. However, probably the most remarkable trait of the software is its implementation to train supervised ML classifiers to score cell phenotypes (Jones *et al.*, 2009). In this approach, the researcher annotates segmented cells to recognise different cell phenotypes according to the large amount of single-

cell features extracted throughout a CellProfiler pipeline. During the training process, CellProfiler Analyst fetches random cells to be annotated by the user, who assigns labels of different predefined categories (phenotypes of interest for the experiment). The software provides iterative feedback to assess and enhance the classifier. Once a satisfactory performance is achieved, rules can be rapidly applied to automatically score all the cells on the screening.

4.3. ilastik

ilastik is a collection which includes a series of ML implementations to perform bioimage analysis (Berg *et al.*, 2019). Its user-friendly GUI and concise documentation (https://www.ilastik.org/) allows ilastik to reach end users without prior experience in computer science, not by a long shot ML technical knowledge. This tool provides templates of workflows for automated segmentation, classification, tracking and counting. These workflows necessitate example annotations from the user, i.e., ilastik is based on a supervised ML paradigm. Accordingly, a sum of features of pixels or objects are taken into account by the classifier, a nonlinear algorithm which performs the workflow parametrisation based on the training data provided by the user. The training mode provides real-time feedback of the algorithm class assignment, allowing an interactive improvement of the classifier. Once the classifier has been trained on a representative subset of the data, it can be used to automatically batch process a larger number of images. ilastik is able to handle microscopy multidimensional images, although it is important to note that ilastik can load any basic image format (TIF, PNG, JPG) or the ilastik preferred HDF5 files, but not all the proprietary formats typically loaded within Fiji by means of the Bioformats plugin (Linkert *et al.*, 2010).

ilastik only provides predefined workflows. Although it may be enough to solve many bioimage analysis problems, others may require pre- and/or post-processing steps within other software packages, as will be stated below. Indeed, ilastik workflows can be further 'imported' to other tools such as the ones mentioned above, e.g., for specific post-processing or analysis tasks. Therefore, ilastik can be combined with other bioimage analysis collections to build powerful workflows. The ilastik team has developed an ImageJ plugin which allows to import and export ilastik format files (HDF5) and to run pre-trained workflows summoning ilastik from Fiji, e.g., embedding an ilastik classifier within an ImageJ script.

Pixel classification is the most commonly used workflow provided by ilastik.

Indeed, all the other workflows within ilastik can (or even need to) be preceded by pixel classification. It consists of a semantic segmentation and, as a supervised approach, users must provide examples for each semantic class. This is done just by painting brushstrokes on the raw input images. To predict the probability for a pixel to belong to each class, ilastik uses the output of image processing filters as features. Users are able to set different filter kernels (for colour/intensity, edge-ness and texture) with a potential wide range of different radius sizes (σ) which may be applied in both 2D and 3D. As a classification algorithm, ilastik uses a Random Forest **(Breiman, 2001; Geurts, Irrthum & Wehenkel, 2009)**. As output, pixel classification workflows generate probability maps, where every pixel takes the numerical values of its probability to belong to each of the user-defined classes. In detail, it generates a multichannel image (one channel per user-defined class) whose sum projection should be 1 for each pixel. Alternatively, it is possible to obtain a segmented image taking the highest probability as the output class for each pixel. It is important to note that pixel classification separates the image into classes but not compute connected components. It is to say, semantic segmentation does not carry on the partition of an image into individual objects. This so called instance segmentation for connected components analysis must be applied on other ilastik workflows which use probability maps as input (e.g., object classification, tracking) or outside ilastik (e.g., Fiji, CellProfiler). Indeed, for the analysis of considerably overlapped objects it is necessary to post-process the pixel classification workflow applying, e.g., watershed-based algorithms in order to obtain individual objects.

The object classification workflow computes connected components, i.e., separates the image into individual objects. In this case, ilastik assigns a tag to each individual object according to several user-defined classes. Objects may be obtained either from an ilastik pixel classification workflow or from a different bioimage analysis collection. To perform instance segmentation, the workflow uses a single semantic class (either from a probability map or a segmented image). For example, one may: i) use pixel classification to separate an image into the semantic classes ‘nucleus’ or ‘background’ and, then, ii) use object classification segment nuclei as individual instances and classify them as ‘mitotic’ or ‘non-mitotic’. User example annotations to train the classifier are provided just by mouse clicking on the objects to assign the different labels. Object-level classifier computes object features comprising size, intensity distribution statistics (both within the object and its vicinity), convex-hull shape descriptors, skeleton-based metrics and location information.

5. Bioimage analysis applied to the study of tissue maintenance and repair in the mammalian nervous system

Elucidating the complexity of the mammalian brain is probably one of the major challenges of modern biological research and neuroscience heavily relies on image data as a primary source of information to unravel the intricacy of a highly complex organ. Advancements in microscopy have contributed to the generation of a wealth of structural and functional image data that need to be objectively, efficiently, and reproducibly analysed beyond what the human eye can notice. Relevant data in the analysis of the nervous system is collected both at the light and electron microscopy levels using either *in vitro* or *in vivo* experimental setups. Although some methods and software tools have already been developed to this end, the parallel improvement of computing techniques, including artificial intelligence, continually offer new opportunities for further developments. In this thesis, we have focused on two mammalian neural systems that could greatly benefit from the development of new bioimage analysis tools or the sophistication of the ones already in use, especially if they can be applied to microscopy-based screenings. One is the quantitative assessment of the adult neural stem cells (NSCs) basic properties as key elements for understanding the neural tissue maintenance and regeneration and the other is the oligodendrocyte-progenitor-driven process of myelination. Both topics are somehow interconnected and can be studied using both *in vitro* and *in vivo* models. The first one was chosen because NSCs can be cultured *in vitro*, either as floating 3D clones or on adherent substrates using well-established protocols (Ferrón *et al.*, 2007; Belenguer *et al.*, 2016) which enables the study of their properties and behaviour in microscopy-based screening assays that differ in complexity. The second one was selected because, despite being a process classically addressed using bioimage analysis and the existence of powerful *in vivo* models to study the remyelination process that follows demyelination (Merrill, 2009; Franklin & Ffrench-Constant, 2017), current tools are somehow either over simplistic or excessively complex for being routinely used by life scientists. Besides, the *in vivo* approach limits the throughput of the analysis taking into account that these experiments involve the manual analysis of medium-size datasets of electron microscopy images. Consequently, the analysis step often becomes a bottleneck when it comes to getting quantitative data.

5.1. Adult neurogenesis in the mammalian brain: NSCs and neurosphere cultures

The generation of new neurons occurs beyond development in the subependymal

zone (SEZ; also known as ventricular-subventricular zone or V-SVZ) located in the walls of the lateral ventricles (LVs) and in the subgranular zone (SGZ) of the dentate gyrus of the hippocampus (Bond, Ming & Song, 2015; Chaker, Codega & Doetsch, 2016). The SEZ (**Figure 3**) is the largest and most active neurogenic niche, responsible for the continued production of olfactory neurons throughout the mouse lifespan (Obernier *et al.*, 2018). Originated from fetal radial glia, subependymal NSCs, also known as B1 cells, retain a characteristic apico-basal polarity (Doetsch *et al.*, 1999; Doetsch, 2003; Kriegstein & Alvarez-Buylla, 2009; Fuentealba *et al.*, 2015; Furutachi *et al.*, 2015; Chaker, Codega & Doetsch, 2016). This polarity is defined by the extension of two processes from the apical and basal regions of the NSC body. A short apical process, that ends in a primary cilium, breaks through the ependymal layer, thus reaching the cerebrospinal fluid (CSF). Specifically, the process pierces the centre of pinwheels, structured rosettes of multiciliated ependymal cells. A longer basal process contacts the specialized vascular plexus that irrigates this niche (Mirzadeh *et al.*, 2008; Tavazoie *et al.*, 2008; Fuentealba, Obernier & Alvarez-Buylla, 2012; Chaker, Codega & Doetsch, 2016).

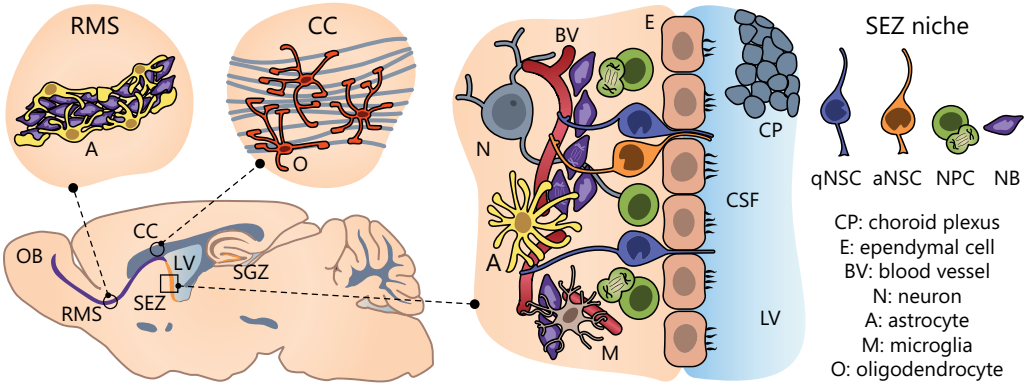

Figure 3. The adult subependymal zone (SEZ) niche. Schematic representation of the adult mouse brain (sagittal view) where the subependymal zone (SEZ) is magnified. The SEZ niche has a particular cytoarchitecture where signals coming from different niche cells contribute to the maintenance of neural stem cells (NSC) and the production of their progeny. The rostral migratory stream (RMS) serves as the main highway towards the olfactory bulb (OB) for newly produced neuroblasts (NB) with the aid of astrocytes (A), while oligodendrocytes (O) incorporate into the corpus callosum (CC). LV: lateral ventricle; SGZ: subgranular zone; CSF: cerebrospinal fluid; qNSC: quiescent NSC; aNSC: activated NSC; NPC: neural progenitor cell; NB: neuroblast.

Coexisting NSCs show heterogeneous proliferative states which can be grouped into two main conditions, quiescence or activation. These states differ both phenotypically and transcriptionally (Pastrana, Cheng & Doetsch, 2009; Daynac *et al.*, 2013; Codega *et al.*, 2014; Giachino *et al.*, 2014; Mich *et al.*, 2014; Llorens-Bobadilla *et al.*, 2015;

Dulken *et al.*, 2017; Basak *et al.*, 2018; Morizur *et al.*, 2018; Belenguer *et al.*, 2020). Activated NSCs produce transit-amplifying progenitor cells (Doetsch, García-Verdugo & Alvarez-Buylla, 1997; Doetsch *et al.*, 1999), which rapidly perform 3-4 symmetrical divisions before progressing into neural progenitor cells called neuroblasts (NBs). Then, NBs migrate anteriorly away from the SEZ, and together form the rostral migratory stream (RMS) to the olfactory bulb (OB) (**Figure 3**). In the RMS, newborn NBs migrate tangentially and organised in chains surrounded by gliotubes formed by astrocytes (Doetsch & Alvarez-Buylla, 1996; Lois *et al.*, 1996; Lalli, 2014). NBs still divide once or twice before they differentiate into OB neurons (Chaker, Codega & Doetsch, 2016).

Specifically, NBs differentiate into mature interneurons that integrate into the granule and the glomerular cell layers of the OB (Doetsch & Alvarez-Buylla, 1996), thus contributing to the neural plasticity for the processing of olfactory information and the odour-reward association process (Lledo & Saghatelyan, 2005; Livneh, Adam & Mizrahi, 2014; Chaker, Codega & Doetsch, 2016; Lledo & Valley, 2016; Obernier & Alvarez-Buylla, 2019). After an injury, such as ischemic stroke, proliferation increases on the SEZ and newly-born NBs can divert from the RMS path and instead migrate towards the injury site, although most of them seem to have a short lifespan (Arvidsson *et al.*, 2002). Although to a lesser extent, subependymal NSCs also contribute to the production of astrocytes and oligodendrocytes. While newly-born astrocytes migrate to the RMS and the corpus callosum (CC), oligodendrocytes migrate to the CC to collaborate in myelination (**Figure 3**) (Menn *et al.*, 2006; Sohn *et al.*, 2015). Although subpendymal NSC-based gliogenesis is not as frequent as neurogenesis under homeostatic conditions, it significantly increases after injury. Therefore, newly-generated astrocytes and oligodendrocytes migrate towards the lesion site and play an active role in tissue repair (Nait-Oumesmar *et al.*, 1999; Picard-Riera *et al.*, 2002; Benner *et al.*, 2013).

The niche cytoarchitecture is essential for the NSC function, which is subtly regulated by both niche-intrinsic factors and foreign factors reaching the apico-basal processes from the bloodstream and CSF. Regarding these extrinsic elements, the apical process receives factors secreted by the choroid plexus to the CSF, whereas the basal process participates in the NSCs regulation by means of systemic factors traveling throughout blood vessels. Moreover, the interplay with other cells present within the niche, also capable of secreting soluble factors, play a major role in NSC regulation. This includes the NSCs themselves, their differentiated progeny, glial cells (i.e., parenchymal astrocytes) or ependymal cells. In addition, it has been demonstrated that other cell types, such as microglia or neurons, can also participate on this complex setup (Porlan *et al.*, 2013; Silva-Vargas *et al.*, 2016; Morante-Redolat & Porlan, 2019; Obernier & Alvarez-Buylla, 2019; Sirerol-Piquer *et al.*, 2019).

The isolation and expansion of NSCs from the SEZ of adult mice is possible under defined culture conditions. A proliferative state is induced by growing disaggregated cells under non-adhesive conditions in serum-free medium containing basic fibroblast growth factor (bFGF) and/or epidermal growth factor (EGF) as mitogens. During the first days of the primary culture most of the cells die. Nonetheless, a small population of cells not only survives, but begins to proliferate forming floating, clonal aggregates known as neurospheres (**Figure 4, top**). Primary neurospheres can be dissociated to subculture the obtained individual cells, thus propagating the culture with the formation of secondary neurospheres. Moreover, cultured onto an adhesive substrate in the presence of serum, neurosphere cultures can be induced to differentiate (Ferrón *et al.*, 2007; Belenguer *et al.*, 2016). Initial neurosphere experiments provided the first *in vitro* evidence that self-renewing and multipotential stem cells were present within the adult mammalian brain (Reynolds & Weiss, 1992). Although individual NSCs do not seem able to generate

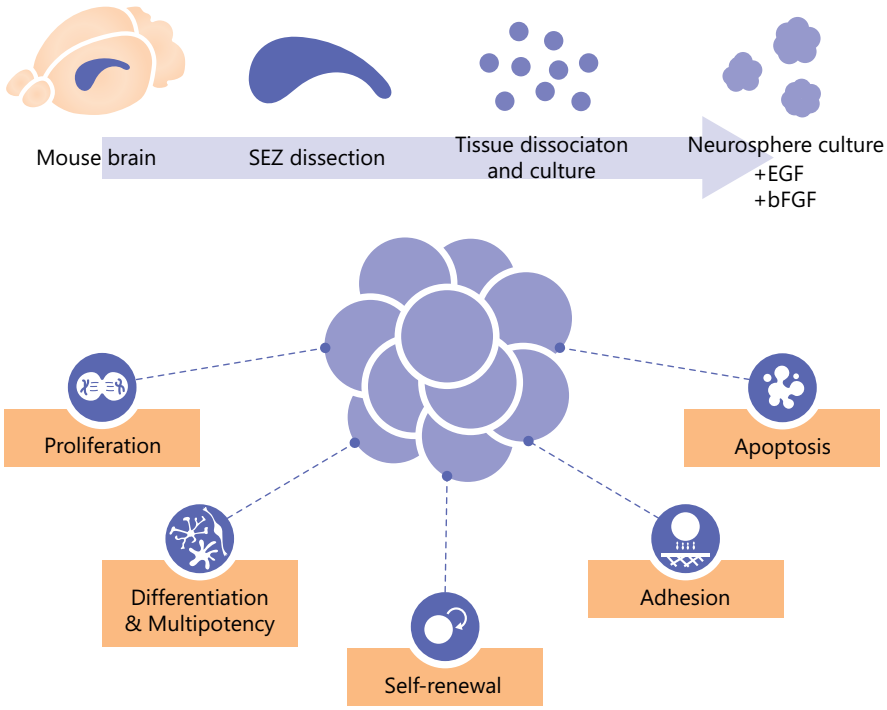

Figure 4. NSCs *in vitro* culture and applications. Graphic representation of neural stem cells (NSC) culture establishment and versatility. Subependymal zone (SEZ) homogenates are cultured in the presence of mitogens EGF and bFGF to generate floating clonal aggregates named neurospheres. Once established, neurosphere cultures can be used to study multiple traits of adult NSC, such as proliferation, differentiation and multipotency, self-renewal, adhesion and apoptosis.

both neurons and glia *in vivo* (Ortega *et al.*, 2013), cultured NSCs are multipotent *in vitro*. Indeed, cultured NSCs retain the capability to differentiate into the three neural lineages, i.e., neurons, astrocytes and oligodendrocytes (Menn *et al.*, 2006; Bond, Ming & Song, 2015; Sohn *et al.*, 2015).

Neurosphere cultures have become a central technique for the study of adult NSCs in a highly controlled environment (**Figure 5, bottom**). During the last three decades, a great effort has been made in order to standardise proper methods for the isolation and propagation of NSCs (Reynolds & Weiss, 1992; Richards, Kilpatrick & Bartlett, 1992; Weiss *et al.*, 1996; Rietze & Reynolds, 2006), as well as for the assessment of self-renewal and multipotency on the *in vitro* culture (Singec *et al.*, 2006; Wachs *et al.*, 2003). Indeed, the coexistence of different protocols diverging on experimental variables (e.g., cell density, media composition, elapsed culture time…) has sometimes led to the generation of inconsistent results (Reynolds & Rietze, 2005; Singec *et al.*, 2006; Pastrana, Silva-Vargas & Doetsch, 2011). Therefore, the use of standardised protocols is critical for the generation of meaningful results and the reproducibility of the experiments.

Despite the fact that neurosphere cultures are a powerful tool for the study of NSCs, it is also important to be aware of the inherent limitations of this *in vitro* approach. The major one is the heterogeneity of the cell populations present in the culture derived from the selective expansion of proliferative cells in a given culture medium. Apart from the NSCs, transit-amplifying progenitors also appear capable of forming neurospheres, albeit their clonal capacity is limited to a few passages. Additionally, *in vitro* cultured NSCs continuously generate committed progeny and even differentiated cells. Therefore, neurosphere cultures are characterized by the co-existence of NSCs and their progeny (Doetsch *et al.*, 2002; Reynolds & Rietze, 2005). As a consequence, only a fraction of the cultured cells behave as *bona fide* NSCs. Indeed, the combination of surface markers and fluorescent reporters for the prospective isolation of pure NSCs from the SEZ, crucial for the detection of quiescent NSCs populations, showed that the strong mitogenic stimulation promotes the selective expansion of activated NSCs on the neurosphere culture. However, slowly-cycling NSCs are also retained in *in vitro* cultures and are able to form neurospheres, although at a slower pace (Belenguer *et al.*, 2020). The combination of *in vitro* culture methods with novel cytometry-based strategies for the prospective isolation of specific subpopulations from the SEZ niche is a promising approach to overcome some of these limitations (Belenguer *et al.*, 2016).

5.2. Remyelination in the central nervous system

Oligodendrocytes are the myelinating cells of the central nervous system (CNS). They extend their processes around axons to form the lipid-rich insulating layer known as myelin sheath (**Figure 5**). The two major functions of CNS myelin are to provide metabolic support to the underlying axons and to empower the rapid transmission of action potentials along the axon (Smith K.J., Blakemore W.F. & McDonald, 1979; Nave, 2010; Frühbeis *et al.*, 2013). On the one hand, oligodendrocytes provide lactate as a substrate for the citric acid cycle, thus supporting the axonal production of ATP (Lee *et al.*, 2012; Fünfschilling *et al.*, 2012; Morrison, Lee & Rothstein, 2013). On the other hand, oligodendrocytes provide an electric insulation of axons. As a consequence, voltage-dependant Na^+ channels localised in the gap between myelin sheaths (referred to as nodes of Ranvier) enable a fast, saltatory conduction of nerve impulses (Arancibia-Carcamo & Attwell, 2014; Rasband & Peles, 2015). In the adult mammalian brain, mature myelinating oligodendrocytes are generated by oligodendrocyte precursor cells (OPCs)

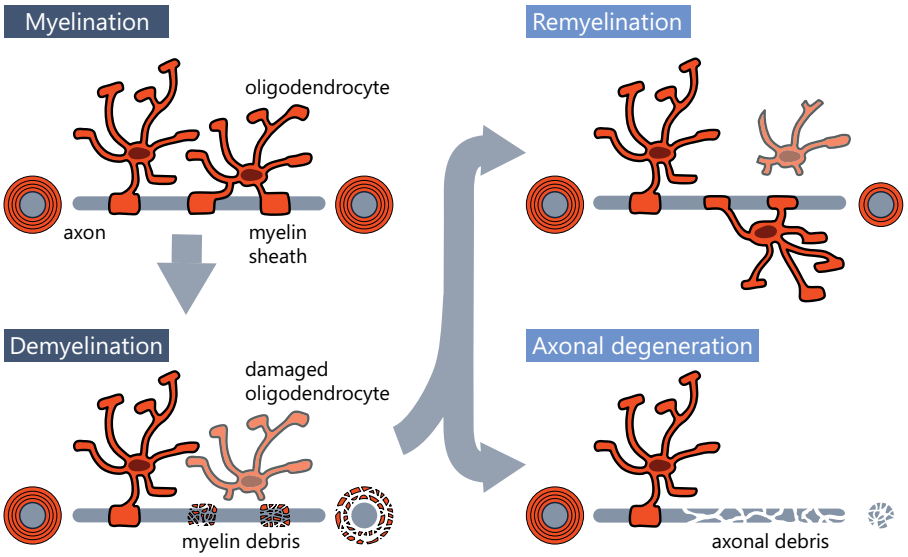

Figure 5. Role of oligodendrocytes in the de/remyelination process. Oligodendrocytes form the myelin sheath that surrounds and protects neuronal axons. Severe damage to oligodendrocytes causes the loss of the myelin sheath, thus leaving underlying axons exposed. This enables newly produced oligodendrocytes to naturally activate the regenerative response of remyelination in order to generate new sheaths. If remyelination fails, the supportive role of the myelin is lost and, consequently, axons degenerate. Adapted from Franklin and ffrench-Constant, 2017.

residing in the brain parenchyma (Gensert & Goldman, 1997; Fancy, Zhao & Franklin, 2004) and by subependymal NSCs (Nait-Oumesmar *et al.*, 1999; Picard-Riera, 2002; Menn *et al.*, 2006). Parenchymal OPCs are locally recruited, as they seem to migrate short distances (Franklin, Gilson & Blakemore, 1997), whereas subependymal NSCs are able to generate oligodendroblasts which migrate to the CC (Menn *et al.*, 2006; Xing *et al.*, 2014; Samanta *et al.*, 2015; Kazanis *et al.*, 2017).

Demyelinating diseases, involving the loss or thinning of the myelin sheaths, are characterised by extensive loss of oligodendrocytes or their impaired functioning. Among these progressive disorders, the most common is Multiple Sclerosis (MS), which is predominantly an autoimmune disease (Ludwin, 2000, Compston & Coles, 2008; International Multiple Sclerosis Genetics Consortium, 2011). Since the axons remain unharmed, CNS demyelinating lesions can be followed by a regenerative response for the formation of new myelin sheaths, a process known as remyelination (Franklin, 2002; Franklin & ffrench-Constant, 2008, 2017; Zawadzka *et al.*, 2010; Plemel *et al.*, 2017; Baaklini *et al.*, 2019) (**Figure 5**).

The disruption of tissue homeostasis caused by demyelination insults induce the activation of adult progenitors that subsequently proliferate to form new oligodendrocytes (Levine & Reynolds, 1999; Fancy *et al.*, 2004; Moyon *et al.*, 2015; Zhao *et al.*, 2015). Additionally, activation can also imply the recruitment of progenitors to the injury site (Messersmith *et al.*, 2000; Murtie *et al.*, 2005; Dehghan *et al.*, 2012; Hughes *et al.*, 2013). Once recruited, OPCs differentiate and mature to provide newly-formed myelin sheaths to denuded axons (Tripathi *et al.*, 2010; Zawadzka *et al.*, 2010; Crawford *et al.*, 2016). For the compaction of the myelin membrane, differentiated oligodendrocytes produce myelin basic protein (MBP), among others (Kimura *et al.*, 1989; Watanabe, Toyama & Nishiyama, 2002; Polito & Reynolds, 2005; Snaidero *et al.*, 2014). Myelin sheaths formed during a remyelination process are often thinner than the ones established during development, a useful feature when it comes to distinguish between areas where remyelination has occurred from those retaining normally myelinated fibres (Blakemore, 1974).

Despite undergoing spontaneous remyelination, with MS progression this regenerative process loses efficiency over time and eventually fails. As a consequence, chronically demyelinated axons are prone to degeneration due to the deficiency on myelin metabolic support, often resulting in subsequent neuronal degeneration (Nave, 2010; Franklin *et al.*, 2012). Indeed, like other regenerative processes, remyelination losses efficiency with ageing (Shields *et al.*, 1999; Hampton *et al.*, 2012; Pfeifenbring *et al.*, 2015), leaving demyelinated axons exposed for longer periods and increasing their

susceptibility to irreversible axonal degeneration (Mei *et al.*, 2016).

The use of different animal models based on chemical-induced demyelination has become a common strategy to unveil the molecular mechanisms underlying remyelination and for the pharmacological assessment in search of drugs to treat demyelinating diseases. The most commonly used toxins are lysophosphatidylcholine (LPC; also known as lysolecithin), ethidium bromide (EtBr) and bis-cyclohexanone oxaldihydrazone (cuprizone). LPC is usually injected into the white matter of the CC or the spinal cord, either in mice or rats. The injection of EtBr into cerebellar peduncles is common in rats, whereas it is also administered into the spinal cord in both rats and mice. Conversely, cuprizone is dispensed by means of oral administration in mouse models. The major advantages of using these models for quantitative assays are: i) the temporal separation between demyelination and remyelination, ii) the dissociation of the demyelination event from the complications derived from the autoimmune process and iii) the localization of the produced lesions on anatomically distinct areas (the latest to a lesser extent in the cuprizone model) .

Objectives

C: 0
M:50
Y:93
K: 0

R:255
G:148
B: 0

Background

The synergistic combination of high-content imaging methods with automated bioimage analysis is emerging as a cutting-edge approach to address many biological questions. However, there are many fields where these techniques are not yet implemented and, instead, they still rely on visual inspection and manual analysis, which unavoidably limit the reachable throughput and are more prone to introduce the investigator bias.

In the present thesis, we have aimed to develop and apply automated bioimaging methods to the study of the adult brain, in particular in the areas of the NSC biology and the process of axon remyelination. Adult NSCs can be cultured *in vitro* and different assays have been developed in the last decades to specifically assess their basic properties, which have greatly advanced our knowledge about adult neurogenesis and neural tissue maintenance and regeneration. Nonetheless, the potential of these *in vitro* models in the form of bigger-scale microscopy-based screenings has not been exploited. Conversely, most of the current analyses are typically performed manually or, at most, software-aided but depending on user supervision. The study of axon remyelination, on the other hand, has classically relied on high resolution electron microscopy images followed by manual annotation for quantification. A few bioimage analysis protocols have been deployed over the years to quantify the myelin ensheathment *per* axon in the form of the well known g-ratio index. However, although some of them attain a certain degree of automation, its use has not spread among scientists. Moreover, all these tools focus on the g-ratio, but none measures the inner tongue, a key element in the (re) myelination process.

Hypothesis

Thereby, we considered as a general hypothesis that the application of bioimage analysis methods and, when possible, the adoption of microscopy-based screening strategies could greatly benefit these two fields of study by increasing both throughput and standardisation of the analysis. In order to address the hypothesis, we selected specific scenarios of varying complexity that combined an experimental setup, image acquisition, and development and implementation of bioimage analysis strategies.

Objectives

With the former consideration, the specific goals that we aimed to achieve were:

1. To deploy a high-throughput screening assay for the *in vitro* assessment of NSC adhesive properties and regulation in 2D cultures.
2. To develop a high-content screening assay for the single-cell analysis of NSC proliferation and apoptosis in 2D cultures.
3. To establish a high-content screening assay for the evaluation of NSC self-renewal and clonal-capacity through population analysis of 3D neurospheres.
4. To build a semi-automated workflow to enhance the bioimage analysis throughput of *in vivo* remyelination models using a novel parameter in electron microscopy.

Material and Methods

C: 5
M: 0
Y:89
K: 0

R:254
G:237
B: 0

High-content imaging system

All the microscopy-based screening assays on this thesis have been set up using the high-content imaging system IN Cell Analyzer 2000 (GE Healthcare), hereinafter referred just as ICA-2k. It consists on a fluorescence, widefield imaging system configured with: i) four lasers along with standard polychroics and filter set, ii) transmitted light imaging, iii) four objective lenses with numerical apertures (NA) fitted for imaging plastic-bottom microplates (4x / 0.2 NA; 10x / 0.45; 20x / 0.45 NA; 40x / 0.6 NA), iv) hardware (i.e., laser) and software autofocus, v) automated objective, correction collar and polychroic changing, vi) large chip CCD camera (2048 x 2048 pixels), vii) environment control and liquid handling modules, viii) retrospective multi-image restoration software. Additional modules such as hardware for 3D imaging or stitching software are not available in our ICA-2k configuration. The system enables imaging different types of microplates (96, 384 or 1536 wells) and includes a module to handle slides.

ICA-2k stores image data within a single folder (with no subfolders) where each image is saved as a single 12-bit, 2D, TIF file. Moreover, all the images are automatically tagged following a fixed naming pattern which includes: the correlative well (row and column) and field-of-view (code that identifies the specific position of the image the well), as well as the corresponding channel (depending on the excitation/emission wavelengths selected during the acquisition). The system also includes its own image analysis software (IN Cell Investigator and IN Cell Developer Toolbox), decoupled from image acquisition, that recognizes and organizes all the captured wells and fields-of-view in each of them, and offers different analysis tools. However, as already mentioned, we decided to design our analysis tools using free open-source programs that can easily handle ICA-2k files although cannot directly interpret the information in the filename to reconstruct the original plate. In order to do so, we had to implement a customized metadata interpretation step in our workflow development.

Neurosphere cultures: establishment of primary cultures, subculture and propagation

Neurosphere cultures were obtained from the SEZ of mice between 2-4 months old as described by **Belenguer *et al.* (2016)**. All the cell cultures were obtained from the C57BL/6J mice strain, bred and housed at the animal housing facility (Universitat de València, Servei Central de Suport a la Investigació Experimental, Burjassot) according to the European Union 2010/63/UE and Spanish RD-53/2013 guidelines and under

official veterinary supervision. Housing established 12 h periods of light/darkness, room temperature of 20-22 °C and free accessible diet of pellets and water. Litters were weaned 21 days after birth. All experimental procedures were approved by the Ethics Committee of the Universitat de València (CEEA: 2015/VSC/PEA/00132 and 00133).

Mice were sacrificed by cervical dislocation and the brain was carefully extracted in order to avoid tissue damage. Brain was kept on cold sterile commercial Dulbecco's Phosphate Buffered Saline without magnesium or calcium (DPBS) until the dissection of the SEZ. For the dissection, brains were moved to a cell culture room and SEZs isolated under a dissecting microscope using micro-scalpels as described in Belenguer *et al.* (2016). SEZ fragments from each brain were put into a 15 mL sterile tube and moved into a laminar flow cabinet in order to keep strict sterile conditions. Then, tissue was enzymatically disaggregated. A papain solution was used to this aim, and tubes were incubated 30 min at 37 ºC to digest the tissue. Then digestion was stopped by diluting papain with control medium (see **Tables 2,3**).

Table 2. Preparation of NSC control medium.

Reagent	Working conc.	Stock conc.	Provider	Cat. nr.
DMEM/F12 (1:1) with L-Glutamine	1x	1x	Gibco, BRL	11320-074
D(+)-Glucose	0.6 %	30 %	Panreac	141341
Sodium bicarbonate	0.1 %	7.5 %	Biowest	L0680-500
HEPES	5 mM	1 M	Biowest	L0180-100
L-Glutamine	2 mM	200 mM	Gibco, BRL	25030-081
Antibiotic / Antimycotic	1x	100x	Gibco, BRL	15240-062
Hormone mix	1x	10x	Homemade (Table 3)	
Heparin sodium salt	0.7 U/mL	350 U/mL	Sigma	H3149
Bovine Serum Albumin (BSA)	4 mg/mL	powder	Sigma	B4287

DMEM/F12 (Dulbecco's Modified Eagle Medium / Ham's F12 Nutrient Mixture); conc.(concentration); Cat. nr. (catalogue number).

Table 3. Preparation of 10x hormone mix.

Reagent	Working conc.	Stock conc.	Provider	Cat. nr.
DMEM/F12 (1:1) with L-Glutamine	1x	1x	Gibco, BRL	11320-074
D(+)-Glucose	0.6 %	30 %	Panreac	141341
Sodium bicarbonate	0.1 %	7.5 %	Biowest	L0680-500
HEPES	5 mM	1 M	Biowest	L0180-100
Apo-transferrin	1 mg/mL	Powder	Sigma	T2252
Bovine insulin	0.05 mg/mL	8.3 mg/mL	Sigma	I6634
Putrescine	160 µg/ml	96.5 mg/mL	Sigma	P7505
Progesterone	0.2 nM	2 µM	Sigma	P6149
Sodium selenite	0.3 µM	3 mM	Sigma	S9133

DMEM/F12 (Dulbecco's Modified Eagle Medium / Ham's F12 Nutrient Mixture); conc.(concentration); Cat. nr. (catalogue number).

Tubes were centrifuged at 100 xg for 2 min and the supernatant was carefully removed. Tissue was gently dissociated in control medium. After another centrifuge step (200 xg for 10 min), supernatant was removed, the pellet resuspended on growing medium (see **Table 4**) and seeded on 48 microwell plates. Finally, plates were incubated at 37 ºC within a 5 % CO_2 humidified incubator for 7-10 days to allow progenitors to proliferate. Although neurosphere NSCs cultures keep their proliferative potential over tens of passages, we have observed that after 9-10 passages cultured cells undergo telomere shortening and show signs of stress (Ferrón *et al.*, 2009). Therefore, our NSC cultures are only maintained and exploited for research purposes at most until the eighth passage.

Table 4. Preparation of NSC growing medium.

Reagent	Working conc.	Stock conc.	Provider	Cat. nr.
Control medium	1x	1x	Homemade (Table 2)	
EGF	20 ng/mL	4 µg/mL	Gibco, BRL	53003-018
bFGF	10 ng/mL	25 µg/mL	Sigma	F0291

EGF (epidermal growth factor), bFGF (basic fibroblast growth factor).

NC-L929 cell line

L929 cells proceed from C3H/An mouse areolar adipose and subcutaneous tissue. L929 fibroblasts overexpressing N-cadherin (NC-L929) are derived from the L929 fibroblasts and were generously loaned by Dr Robert Kypta from CiCBiogune (Bilbao). These cells grow as a monolayer under adherent conditions on plastic plates and in DMEM supplemented with 1% L-glutamine and 10% fetal bovine serum (see **Table 5**; Porlan *et al.*, 2014). Cells were subcultured when a 80-90 % confluence was reached to avoid overgrowth. This was done by dilution after treatment with trypsin-EDTA (ethylenediaminetetraacetic acid).

Table 5. Preparation of cell line medium.

Reagent	Working conc.	Stock conc.	Provider	Cat. nr.
DMEM high Glucose (1:1) without L-Glutamine or Sodium Pyruvate	1x	1x	Biowest	L0101
Fetal Bovine Serum (FBS)	10 %	100 %	Biowest	S1810
L-Glutamine	4 mM	200 mM	Gibco, BRL	25030-081
Sodium Pyruvate	1 mM	100 mM	Gibco, BRL	11360-039
Penicillin/Streptomycin	1x	100x	Sigma-Aldrich	P4458

DMEM/F12 (Dulbecco's Modified Eagle Medium / Ham's F12 Nutrient Mixture); conc. (concentration); Cat. nr. (catalogue number).

Focal demyelinating lesions

In order to assess remyelination, mice were first submitted to focal demyelinating lesions on the CC by means of stereotactic injection of the myelin toxin LPC, following the protocol described by Rittchen *et al.* (2015).

Transmission electron microscopy: sample preparation

An intraperitoneal injection of a ketamine/medetomidine mixture (75 mg/kg and 1 mg/kg body weight, respectively) was administered to anaesthetise the mice. Then, blood was flushed out from the vasculature with ice-cold PBS before proceeding to the

intracardiac perfusion of 4 % PFA and 2 % glutaraldehyde in 0.1 M phosphate buffer (pH 7.4; PB). Finally, brains were extracted and post-fixed in the aforementioned fixation solution for 2-16 hours at 4 °C. Brains were washed in PB and coronal 1-mm thick sections were obtained with a vibratome. Sections anterior and posterior containing the LPC-focally-injected side of CC were further dissected, keeping only a small portion of cortex and CC, and trimmed to a right-angle at the midline of CC. Finally, sections were cut in trapezoid shape, in order to aid orientation at the resin embedding stage, and post-fixed in 1 % glutaraldehyde in PB at 4 ^{0}C. Sections were processed for embedding in the resin T031 TAAB 812 premix kit-medium strength, as per manufacturer's guidelines. Blocks were trimmed to expose the tissue and sagittal 1 µm semithin sections were cut. In order to determine presence or absence of demyelinating lesions in CC, sections were stained with 1 % toluidine blue in 2 % sodium borate solution. Presence was assessed based on a series of indicators, such as: i) cell accumulation, ii) crude cell morphology, iii) anatomical location along the anterior posterior axis of the CC and iv) reduction of myelin staining. Assessment was validated by two blinded observers. Once identified, selected areas from tissue blocks containing a demyelinated lesion were cut into ultrathin 60-nm thick sections with an ultramicrotome and collected into formvar-coated copper grids. Ultrathin sections were stained with uranyl acetate and lead citrate and imaged by means of transmission electron microscopy (TEM).

Semithin sections with lesions were selected and imaged using an AxioScan Slide Scanner with a 40x objective in order to generate a map of the lesion location. The map enabled the orientation of ultrathin sections with respect to lesion location at the TEM. Then, representative images were acquired throughout a JEOL JEM-1400 Plus TEM, coupled to a GATAN One View camera, at 7.1 K magnification (8.62 µm x 8.62 µm image size).

Expert annotations

Neurosphere formation assay images (as whole reconstructed wells) were manually annotated using QuPath **(Bankhead *et al.*, 2017)** by two experts in order to generate two independent, redundant annotation sets. Annotations were made using the brush tool to label each neurosphere as a single object, as long as neurospheres remained clearly distinguishable from each other, even if clumped together. Neurospheres of diverse sizes and shapes were annotated, but not individual cells or those cells forming small clusters rather than actual neurospheres. Once completed, QuPath annotations were converted into ImageJ ROIs (ZIP files) for their comparison with the segmentation results. The annotation set from one expert was established as ground truth, whereas

the set annotated by the other expert was used to assess the variability between human operators. For the annotations of fibre components on remyelination models, three ROI sets were manually annotated *per* TEM image. Annotations were made by a single expert with Fiji's freehand selection tool, generating ground truths for the segmentation of the fibres, the inner myelin boundaries and the axoplasms. Each ROI set was saved as an independent ZIP file. Since the segmentation assessment is performed on binary masks, touching objects were annotated with a separation from each other enough to keep them as independent objects setting an 8-connected particle tracing.

Metrics for the assessment of instance segmentation

For the evaluation of the instance segmentation we applied an object-based metric that scores every object as correctly segmented or not. The score is based on the establishment of a threshold for the minimum area coverage between overlapping objects. The area coverage is calculated as the intersection over union (*IoU*) between the target (*T*), i.e., the ground truth, and the prediction (*P*) masks:

$$IoU(T,P) = \frac{T \cap P}{T \cup P}$$

The intersection (T⋂P) is the sum of the pixels shared by both the target and the prediction masks (i.e., Boolean operator AND), whereas the union (TUP) is the sum of the pixels found either on the prediction or the target masks (i.e., Boolean operator OR). The per-object *IoU* was computed using a customised ImageJ macro included in the NeuroMol Lab update site within Fiji **[NeuroMol Lab > Assess Segmentation > Instance Segmentation]**. Requirements, installation and usage documentation, as well as an example image dataset is to be found in GitHub (https://github.com/paucabar/assess_segmentation). The macro uses region connection calculus **(Landini *et al.*, 2019)** to identify overlapping objects. This way, *IoU* is only computed for those target objects that overlap to any extent with any object on the prediction mask. As a result, if the ground truth contains *n* true objects and the prediction *m* estimated objects, the macro generates a $C_{n \times m}$ matrix where only the pairs with an *IoU* above an established threshold are set as one. Conversely, the vast majority of pairs are set as zero, since they represent pairs with an *IoU* below the established threshold, including those which do not share any pixel at all (see fig ...). According to our segmentation method, pixels can only be assigned to a single object, so objects from the same mask (i.e., either axoplasm, IMB or fibre mask) cannot overlap each other. Therefore, by establishing an *IoU* threshold above 0.5 we ensure that for each neurosphere on the ground truth there is no more than one matching neurosphere on the prediction mask. Once filled, the $C_{n \times m}$ matrix is

used to score each comparison as true positive (TP), false negative (FN) or false positive (FP) result. A TP is obtained when a target mask n_x has a corresponding prediction mask m_y, i.e., $C(x, y) = 1$. A FN is obtained when a target object has no corresponding prediction mask, whereas a FP is obtained when a prediction mask does not match any target object. From this data the macro calculates the *F1* score, an index based on two metrics, *precision* and *recall*:

$$F1 = 2 \times \frac{precision \times recall}{precision + recall}$$

On the one hand, *precision* determines the proportion of predicted objects that had a match on the annotated ground truth:

$$precision = \frac{TP}{TP + FP}$$

On the other hand, *recall* determines the proportion of target objects that had a match on the prediction mask:

$$recall = \frac{TP}{TP + FN}$$

Hardware

Bioimage analysis workflows described on this thesis have been performed on a HP OMEN 15-DC0000NS laptop with an Intel® Core™ i7-8750H processor, 16 GB of RAM and an NVIDIA® GeForce® GTX 1060 graphic card.

Results

C:53
M: 0
Y:66
K: 0

R:105
G:255
B:141

Foreword

Taking into account the variety of experimental paradigms that have been addressed from the bioimage analysis point of view in the present thesis, for the sake of clarity, the results section has been divided into four different chapters. They are presented ordered according to the increasing complexity of the bioimage approaches and include:

1. Bioimage analysis for the study of NSC adhesion (relates to **Objective 1**).
2. Bioimage analysis for the study of NSC proliferation and apoptosis (relates to **Objective 2**).
3. Bioimage analysis for the study of NSC clonal capacity and self-renewal (relates to **Objective 3**).
4. Bioimage analysis for the study of (re)myelination (relates to **Objective 4**).

We have considered four main topics to organise the content in each chapter: i) the description of the biological problem to be solved, ii) the experimental and imaging setup established to generate the raw data, iii) the detailed exposition of the development and use of the proposed bioimage analysis workflow and iv) the results obtained in its application in an experimental case study or, alternatively, the assessment of its segmentation performance. Please note that not all the chapters necessarily include these four sections. This is mainly due to the fact that, although all the addressed biological questions have implied an extensive bioimage analysis development, only chapters 1 and 3 include as well work on the optimization of the experimental/imaging setup. Chapter 2 has also involved the necessary experimental work to generate a full image dataset for the development of the analysis workflow, but using standard well-established methods. Therefore, the details regarding the experimental development are provided in the corresponding chapters whereas the general information about the materials and methods can be found in a separated section. Finally, chapter 4 is the result of a collaboration carried on during my 4-month stay at Anna William's Laboratory (MRC Centre for Regenerative Medicine, University of Edinburgh). This chapter does not include an experimental/imaging setup section because the work only involved the development of a bioimage analysis strategy to analyse existing image datasets.

Emphasis is given to the public access to the scripts of the developed tools, which are available for anybody keen on their use. Installation of the workflows implemented in Fiji is straightforward, since are provided through a Fiji update site. Other workflows, implemented either in ilastik or CellProfiler, are provided as projects or pipelines which can be directly loaded within the corresponding software for their use. Additionally, documentation and example image datasets are also provided along with all the tools.

CHAPTER 1. BIOIMAGE ANALYSIS FOR THE STUDY OF NSC ADHESION

1. Biological background: the role of N-cadherin mediated adhesion in the SEZ

Cadherins are type-1 transmembrane proteins that establish calcium-dependent homophilic, cell-to-cell, adherens junctions through their extracellular domain. Members of this family of cell adhesion molecules play critical and varied roles during development and in adult homeostasis. This variety of functions is accomplished because, besides their role as anchorage mediators, they also behave as signal transducers involved in several pathways such as proliferation and apoptosis (Leckband & de Rooij, 2014; Yulis, Kusters & Nusrat, 2018). Interestingly, they have been related to the regulation of the quiescence-activation cycle in several stem cell niches (Marthiens *et al.*, 2010; Chen *et al.*, 2013; Porlan *et al.*, 2014; Cho *et al.*, 2019; Porlan & Morante-Redolat, 2019). In the murine adult SEZ, loss of E-cadherin (cadherin 1, *Cdh1*) leads to overactivation of transit-amplifying progenitors (Karpowicz *et al.*, 2009). In 2014, our laboratory demonstrated that adhesion of the subependymal B1 NSCs to the ependymal layer through N-cadherin (cadherin 2, *Cdh2*) contributes to maintain the structural organization of the neurogenic niche and regulates NSC quiescence. Furthermore, we described that this role is dynamic since the N-cadherin regulated cleavage by MT5-MMP, a membrane-type metalloproteinase (MMP) encoded by the *Mmp24* gene, promotes the activation of B1 cells under physiological and regenerative conditions (Porlan *et al.*, 2014). However, the mechanisms underlying adhesion-mediated quiescence have not been fully elucidated. Therefore, we decided to explore the possible implication in the regulation of NSC adhesion of another member of the MMP family, the adamlysin ADAM10. This sheddase, as other ADAM members, contains disintegrin and metalloprotease domains and has been reported to cleave N-cadherin in neurons (Lo Sardo *et al.*, 2012). In fact, it is one of the most highly expressed proteases in the adult brain, including the SEZ (Kärkkäinen *et al.*, 2000; Guo *et al.*, 2016).

In order to investigate the effects and regulation of the N-cadherin mediated adhesion of NSCs and characterize putative niche secreted factors involved in its cleavage, we have developed a functional *in vitro* cellular assay that models the anchorage of subependymal cells mediated by N-cadherin and automated its analysis by adopting a high-content imaging strategy and developing a bioimage analysis tool for the extraction of the relevant quantitative data. Since some of our preliminary *in vivo* results suggested that ADAM10 could be involved in the cleavage of the N-cadherin present

at the NSC membrane (unpublished data), we applied our strategy to quantitatively address the role of ADAM10 on the regulation of the N-cadherin-mediated adhesion of NSCs in culture.

2. Experimental and imaging setup: microscopy-based high-throughput screening assay to assess N-cadherin anchorage

Cell adhesion assays aim to quantify the anchorage of isolated cells to either surfaces coated with purified ligands/matrix components or to other cells usually in the form of monolayers. Protocols deployed for this purpose may be divided into two main approaches: static and dynamic assays (Butler *et al.*, 2009; Humphries 2009; Mobley *et al.*, 2001). Static assays consist of evaluating the capacity of cells in suspension to attach to adhesive surfaces (e.g., a coated multiwell plate), whereas dynamic assays are flow-based, so cells are perfused over the adhesive surface (e.g., a glass capillary coated with an immobilized adhesion molecule). Dynamic systems are suited for live cell imaging, which may be really helpful when addressing some specific questions, but also reduces the throughput due to a more complex setup and analysis. Therefore, for our microscopy-based screening assay we chose a static approach. In addition, to mimic as much as possible the *in vivo* conditions, instead of a purified recombinant protein as coating, the adherent substrate was provided by a pre-grown monolayer of live cells overexpressing the ligand of interest.

As depicted in **Figure 6**, in our assay neurospheres are mechanically disaggregated, in order to preserve the integrity of the N-cadherin extracellular domains, and deposited onto a confluent monolayer of NC-L929 fibroblasts overexpressing N-cadherin (Porlan *et al.*, 2014). In case the interrogated NSCs are not intrinsically fluorescent (i.e. obtained from transgenic reporter mice or derived from genetically modified cultures), they are labelled with the DDAO-SE cell tracer to facilitate their detection. Additionally, in order to include a specificity control, part of the cells are pre-incubated with the N-cadherin blocking antibody GC4 (NcadBlock) to reduce their N-cadherin-mediated adhesion or with isotype mouse IgG (IsoMsIgG) as control (Porlan *et al.*, 2014). Once left to attach for a controlled time, non-adhered cells are thoroughly washed out, and cultures are fixed for further analysis. Finally, nuclei are counterstained with DAPI in order to visualize the subjacent monolayer cells and images are acquired throughout a high content microscope. Any experimental scenario leading to alterations in the levels of extracellular N-cadherin (i.e. pre-treatment with soluble factors or genetic modifications) might be evaluated by this assay.

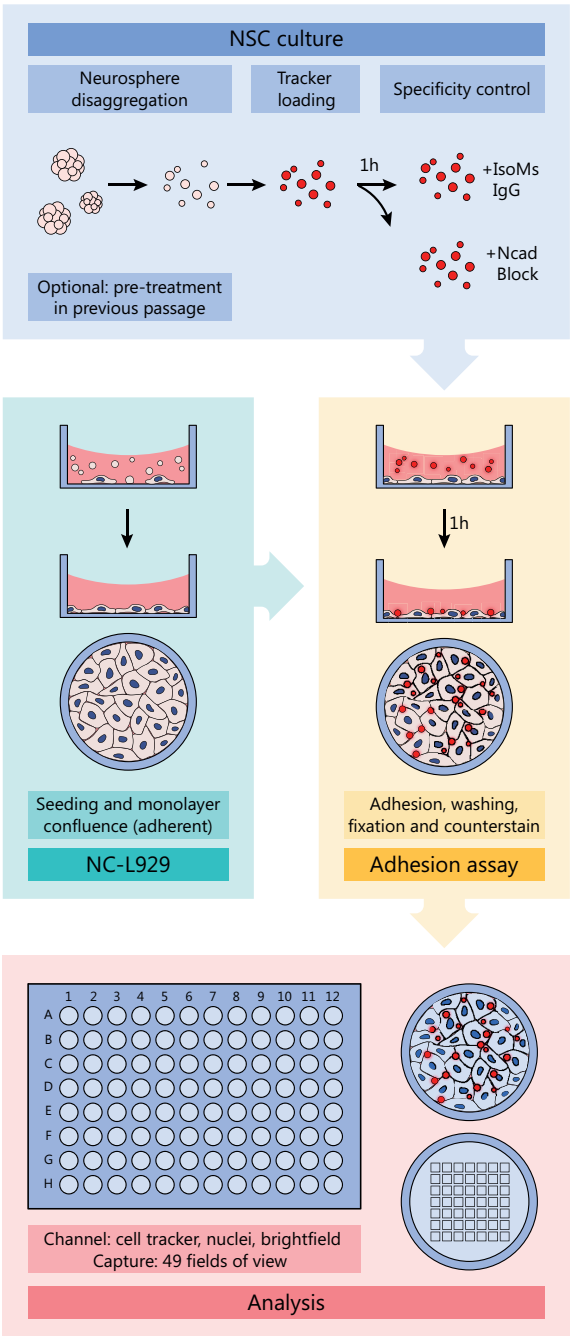

Figure 6. Schematic representation of the main steps of the experimental and imaging setup of the N-cadherin-mediated NSC adhesion assay.

In order to get quantitative data, we aim at devising an analysis protocol that should perform two different tasks: estimate the percentage of culture surface occupied by the N-cadherin expressing monolayer, and detect and count the number of labeled NSCs attached to it. As has already been discussed, bioimage analysis protocols greatly benefit from having properly optimized the image acquisition process. The idea is to obtain image datasets that suit the analyses requirements while keeping the file size as small as possible. This allows to save large amounts of memory space (see **Table 6**), which is especially important in high-throughput assays and also reduces considerably the required computation time. In our case, where precise cell morphology is not required to achieve the aforementioned tasks, we observed that it was sufficient to capture low resolution images. Indeed, imaging conditions have been set up to reach a compromise between reducing the image size to the minimum and still be able to efficiently detect the objects of interest (tracer-positive cells). Simplifying the Nyquist-Shannon sampling theorem, if the object size is above the Abbe's diffraction limit, a good rule of thumb is to sample

objects with a minimum length of 5-10 pixels.

Table 6. Effect of binning and bit-depth on file size.

Bit-depth	Binning 1x1	Binning 2x2	Binning 4x4
8-bit	4 MB	256 KB	16 KB
16-bit	8 MB	512 KB	32 KB
32-bit	16 MB	1 MB	64 KB

Taking as example an image whose dimensions are 2024 x 2024 pixels we observe that: i) file size doubles when bit-depth doubles, as both are directly proportional; ii) conversely, applying a 2x2 binning downsizes the image to a 1/4 of its original size (512x512 pixels), while the file size experiences a 16-fold reduction. The effect is even sharper when applying a 4x4 binning, reducing the image dimensions to its 1/16 fraction (128x128 pixels) while cutting down 256 times the file size. MB (Megabyte), KB (kilobyte). 1 MB is equal to 1024 KB.

We set up our ICA-2k imaging system to sample objects close to the lower limit of this range. For NSCs *in vitro* cultures, this can be achieved using the 40x objective with a 4x4 binning. Alternatively, it is possible to use a lower binning and downsize the dataset on a post-acquisition step. We sample a minimum of 49 non-overlapping fields-of-view *per* well distributed along the whole well surface, keeping the positions constant between wells in the same experiment. Counterstain and DDAO-SE channels are acquired with the ICA-2k pre-set DAPI and Cy5 wavelengths, respectively. Automatic focus is performed on the DAPI channel in all the captured fields-of-view by means of the built-in Laser Autofocus system, alone or combined with the Software Autofocus option. However, since the fibroblast monolayer and the adhered NSCs are expected to be in slightly different focal planes, the focus offset is adjusted for each channel.

3. Bioimage analysis

We have developed a bioimage analysis workflow that has been automated in an ImageJ macroinstruction. Like all the ImageJ scripts described in this thesis, the macro used in the present chapter can be downloaded just by adding the NeuroMol Lab update site by means of the Fiji updater. Requirements, installation and usage documentation, as well as an example image dataset, can be found in GitHub (https://github.com/paucabar/cell_adhesion_assay).

The workflow has been assembled in a single macro, although some additional macros may be needed to perform optional pre-processing steps. In its design, we have taken into account the following considerations:

- As mentioned above, we have optimised the image acquisition in our assay to get images where cells are within the range of about 5-10 pixels of length, so the macro is designed to detect such object size. This implies that any image dataset containing larger objects must be previously downsized in order to make it optimally analysable by the macro. To help with this step, we have developed an optional separate preprocessing macro (see **3.1**).

- Image acquisition has been performed throughout the high-content microscope ICA-2k. We take advantage of the fact that metadata information is provided following a standardised naming convention along the filenames to retrieve and use it during the automated analysis. As a consequence, the workflow requires the proper metadata extraction of the dataset for its correct interpretation (see **3.2**).

- In spite of following the same protocol, each performed experiment generates an image dataset that is bound to be unique and display a different degree of particular features. Therefore, most probably it would be necessary to adjust the set of analysis parameters from one experiment to the next. For that purpose, the macro enables to adjust key settings of the workflow in order to suit the analysis for different datasets. Indeed, the macro includes a test mode, which allows the user to tweak the parameters and check the output easily. Moreover, the parameter set can be saved and imported in future analyses (see **3.3** and **3.6**).

- In order to favour unsupervised analysis, we have included the measurement of different image metrics to serve as a quality control. It is important to note that the macro only calculates the quality parameters and does not remove ill-quality images from the dataset. Rejection of problematic fields-of-view is performed *a posteriori* as part of the data analysis either at the user's personal criteria or by applying methods to detect outliers (Caicedo ***et al.***, 2017) or supervised machine-learning approaches (Lou ***et al.***, 2012) (see **3.4**).

- The main goal of the assay is to quantify the number of adhered cells. However, since we are measuring adhesion over a cell-formed monolayer which may sometimes be incomplete or severed, the macro obtains the cell count per monolayer surface (mm^2). In order to do so, it works independently with the counterstain channel (monolayer) and the tracer

channel (adhered NSCs) images segmenting them with a filter-based approach which rapidly batch processes large datasets. However, proper segmentation and object extraction of each of the two components entails its own difficulties. Regarding the cell monolayer, NC-L929 fibroblasts let to grow till confluence are usually well spread over the well surface leaving no empty spaces between them. Nevertheless, since samples are nuclei counterstained, monolayer images show only isolated nuclei surrounded by unstained areas, actually occupied by the non-visible cytoplasm of fibroblasts. As a consequence, segmentation of these images is straightforward but further processing is required in order to artificially fill the empty spaces between the nuclei as an estimation of the real cell monolayer surface. On the contrary, cell tracers stain the whole cytoplasm so NSCs are easily spotted on images but occasionally appear forming small clumps. These aggregates, despite their small size, often reach overlapping levels that greatly hinder cell individualization. Additionally, it is not strange to find highly fluorescent precipitates derived from the labelling process, which also sediment on the monolayer. These two features combined posed a great challenge for designing an effective segmentation strategy. In the end, we opted for a method based on the detection of local maxima that includes a clump-breaking operation based on the voronoi algorithm and a size threshold to avoid precipitated debris (see **3.5**).

3.1. Downsizing and/or illumination correction (if required)

We have included in the NeuroMol Lab collection a macro built to resize a set of images **[NeuroMol Lab > other macros > Post-Acquisition Binning]**. However, it is important to point out that resizing may have severe consequences on the images, especially when interpolation methods are required. In order to prevent non-expert users from dealing with this, the macro only allows to group neighbouring pixels within squared blocks. The binning of the pixels is performed averaging their numerical values. The 2x2 binning reduces each image to a 1/4 of its size, the 3x3 binning to 1/9 and the 4x4 binning applies a scale factor of 1/16 (see **Table 6** in **section 2**). To exemplify the need of this preprocessing step, the image dataset provided to test the adhesion macro in the aforementioned Github site contains objects much bigger than the 5-10 pixels and must be downsized in advance.

In order to decide whether to use binning or not and, if needed, the proper

resizing factor, researchers should first estimate the average size of their cells. This can be roughly accomplished by manually drawing a couple of straight lines for several cells representing the major and minor axis with the selection tools provided within Fiji, and measuring their lengths in pixels.

On the other hand, the quantification of this assay is based exclusively on object count and only relies on intensity values for segmentation. Therefore, unless the uneven illumination of the images harshly affects segmentation, its correction is not required. Anyway, in case it is necessary, the NeuroMol Lab collection also includes a macro to perform retrospective multi-image illumination correction, which will be documented in the next chapter. In case this preprocessing step is needed, it would be advisable to place it on the top of the bioimage analysis workflow, even before downsizing.

3.2. Metadata extraction

The script extracts metadata from the image filename assuming the naming pattern produced by the ICA-2k, which in a static acquisition contains the well code, the field-of-view number and the channel information. The well code is an alphanumeric tag consisting of a 6-character substring formed by a capital letter (row) and a two-digit number (column) separated by a hyphen escorted by two blank spaces (e.g., B - 03 corresponds to the well placed on the second row and the third column). This string always occupies the filename indexes 0 to 5. The field-of-view code and channel information are placed between parentheses immediately after the well code and is followed by the file format. Inside the parenthesis it is first found the field-of-view code formed by a three-digit number introduced by the substring 'fld '. Therefore, it fills the filename indexes 11 to 13. Finally, the channel information (excitation and emission wavelengths) is separated from the field-of-view by a blank space and is introduced by the substring 'wv '. Instead of the specific numerical value in nanometres, the ICA-2k acquisition software labels wavelengths using alphanumeric characters that spell the name of the most common corresponding fluorochrome (e.g. DAPI, FITC, Cy3, etc.). Both excitation and emission labels are included in the filename separated by a hyphen that is escorted by two blank spaces. It is important to highlight that not all the channel alphanumeric labels are of equal length, so the channel substring is not found filling the same indexes in all the images. As an example, *C - 09(fld 011 wv DAPI - DAPI).tif* would be the complete filename of the TIF file corresponding to the DAPI image of the eleventh field-of-view captured in the well placed on the third row and the ninth column of the microwell plate).

In case of having acquired the image dataset with an imaging system different from the ICA-2k, it is still possible to analyse the experiment. However, it will be necessary to recode the images in order to meet the metadata extraction step. To this aim, the NeuroMol Lab update site includes a macro which converts the files generated by means of other imaging systems into a dataset suited to be analysed by our macro **[NeuroMol Lab > other macros > IN_Cell_Analyzer_rename]**.

3.3. Parametrisation

The output of the macro highly depends on the parameters set by the user. Therefore, a GUI based on the use of sequential windows has been deployed to guide the user on these decisive choices. In the main dialogue window, our cell adhesion macro offers two different workflows. On one hand, the pre-analysis mode allows to test different sets of parameters by running the analysis on single images selected by the user. Instead of obtaining quantitative data, the aim of this mode is to easily visualise the result of the segmentation while tweaking the parameters. On the other hand, the analysis mode is designed to perform the full analysis as it batch processes and extracts the quantitative data from all the images. The user also has to specify the path of the folder to be analysed. Both pre-analysis and analysis modes allow to save the defined parameter set as a project file, so the main window offers the possibility to load this preset. If so, a specific window will pop-up to browse the project file. Additionally, the user can also save the ROIs generated after the segmentation of the adhered, tracer-positive cells (note that it only works for the analysis mode).

The next dialog box is the one which really allows tweaking the workflow settings. In case a project file has been loaded, the pre-selected values will be displayed. As NSCs and monolayer cells might be visualized using different tracers and counterstains, it is necessary to indicate which channel corresponds to the counterstain (monolayer) and which one to the cell tracer (NSCs). The rest of the options define filter sizes, threshold values and other similar parameters. For a better understanding, these tweakable parameters are indicated along the workflow explanation and are summarised on **Table 7**. The last window is different for each mode. On the pre-analysis, the user can pick up a well and field-of-view code to apply the selected parameters and visualize the workflow output in the corresponding images. This action is iteratively performed until the user decides to stop. Conversely, the analysis mode displays a dialogue box to select the wells to be analysed, from a single well to the entire experiment dataset. Once checked, the macro batch processes all the selected images and automatically stores the results.

Table 7. User-adjustable parameters found in the bioimage analysis workflow for the quantification of cell adhesion.

Parameter	Variable type	Default
Counterstain channel	String (set from array list)	First element on the list
Tracker channel	String (set from array list)	First element on the list
Maximum filter (monolayer)	Float (radius)	2.0
Threshold (monolayer)	Float (0.00-1.00)	0.10
Prominence (>)	Integer (grey level)	30
Threshold (tracker)	Float (0.00-1.00)	0.10
Minimum object size	Integer (pixels)	5

3.4. Image quality control metrics

Our quality control is intended to detect two different types of unsuitable images: those that are out of focus or contain saturated artefacts, and those that, despite being adequate in terms of image acquisition, contain an incomplete or severed monolayer.

The detection of blurring and saturated artefacts is performed by means of metrics which are widely used within the microscopy-based high content screens (Bray *et al.*, 2012; Caicedo *et al.*, 2017). As a quality control metric for out-of-focus images, the macro extracts the inverse coefficient of variation of the counterstain image intensity. Namely, the ratio of the mean and the standard deviation of the image intensity (mean/s.d.). This is a simple metric, easier to implement compared with others less sensitive to the cell count (highly variable in many high-content screens), such as the power log-log slope of pixel intensities. On our macro, this blurring metric is retrieved from the counterstain channel because it is the one typically used to set the autofocus of the microscope, as it usually shows the better signal-to-noise ratio and displays a highly homogeneous distribution of objects (nuclei). Another reason is that, while not all the fields-of-view, problematic or not, contain adhered, tracer-positive cells, the counterstained monolayer is expected to be present in all images. In order to detect saturation artefacts, the percentage of saturated pixels is the best metric described. The cell adhesion macro extracts this feature also from the counterstain channel since, despite being excited by a wide range of wavelengths, saturated artefacts are typically visualized with the ultraviolet excitation fluorescence.

To assess the monolayer extension, the macro extracts other measurements which are not as typical but, in this case, will be needed to perform an additional quality control assessment that we decided to customise and implement in our assay. Since the mean/s.d. may vary depending on the cell count, the macro also extracts an estimated cell count on the counterstain. To this aim, the counterstain channel is slightly smoothed by means of a 3x3 mean filter (radius=1). The cell count is estimated using the Find Maxima plugin with a prominence greater than 50. Cell count data of the whole dataset is normalized to a 0-1 range. Thus, fields-of-view with a confluent, unharmed monolayer will tend to 1, while those containing no cells will be close to 0. Non-confluent or damaged monolayers will show intermediate values. Finally, the ultimate output of the cell adhesion assay is the cell-adhered count per monolayer area. Therefore, as part of the bioimage analysis workflow, the monolayer area has to be measured. Once the area segmentation is performed (as explained below), it is easy to obtain the monolayer area fraction (monolayer area/field-of-view total area). The ratio must be close to 1, unless either the monolayer is not confluent or has suffered damage during any sample preparation step.

The combination of these image quality control metrics may be helpful to discard ill-quality images avoiding the visual inspection of the entire image dataset. With the aim to show the power of these metrics, we have worked with a subset of images extracted from our example dataset. By visual inspection, they were manually annotated, labelling each of them according to four different predefined classes: suited for the analysis high quality fields-of-view (HQ); images with incomplete monolayer (IM); presence of saturated artefacts (SA) or images with no cell content (NC) (**Figure 7A**). Since the ICA-2k autofocus system usually does a good job focusing the monolayer nuclei, no blurred images were found in our datas***et al***though, to our experience on other assays where similar metrics are applied, NC images show results akin to those obtained from blurry images. Once tagged, the images were artificially sorted as if they belonged to different 'wells' keeping a balanced representation of the four quality classes in all of them. Finally, the images were renamed according to the ICA-2k naming pattern in order to group fields-of-view in consonance with the annotation labels, obtaining samples of the same size for each well, thus allowing the application of the macro on the fabricated dataset. **Figure 7B** shows the potential of the elected metrics to be used to reject ill-quality images.

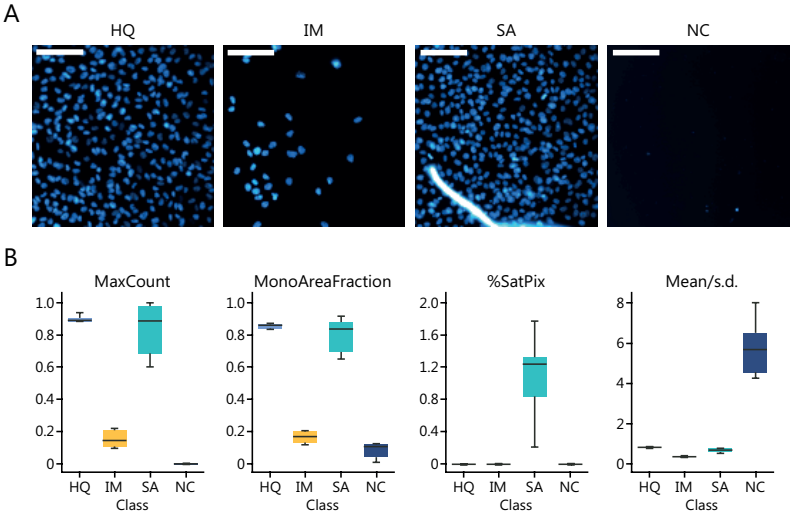

Figure 7. Image quality control (QC) metrics obtained from a subset of a cell adhesion assay dataset. Images were annotated and renamed to group them according to QC labels. **(A)** Up-left, the cell count, estimated as the count of relative maxima (MaxCount) normalized to a 0-1 range. Up-right, the area fraction of the image covered by the monolayer of fibroblasts overexpressing N-cadherin (MonoAreaFraction). Bottom-left, the percentage of saturated pixels (%SatPix). Bottom-right, the ratio of the mean to the standard deviation of the image intensity (Mean/s.d.). **(B)** Annotation examples. Counterstain channel (DAPI) displaying Fiji's Cyan Hot LUT. Scale bar 100 µm. Data was annotated using four different classes: HQ (high quality), IM (incomplete monolayer), SA (saturated artefacts), NC (no content). Box plots were generated using the seaborn.catplot function to show the distribution of the different quality control metrics across the groups. Boxes show the data from the first quartile (Q1) to the third quartile (Q3) and are split by a line showing the median, whereas whiskers show the maximum and minimum values (excluding outliers).

3.5. Detection, segmentation and feature extraction

As already mentioned, the macro obtains the two measurements required to get the final result (number of adhered tracer-positive cells and area of monolayer) working separately with the two captured channels (**Figure 8A**).

On the counterstain channel, although the macro already extracts the monolayer cell count as part of the quality check, in order to estimate the monolayer extension area, it is necessary to fill the empty space between the nuclei. To do so, a maximum filter with a radius defined by the user is applied. Images are normalized to a 0-1 range and, then, the threshold value set by the user is used for segmentation. Once generated the binary mask, the monolayer area and the monolayer area fraction are measured (**Figure 8B**).

On the NSC-tracer channel, adhered cells just need to be detected, individualized if necessary and counted. In order to carry out the segmentation different features are extracted from the images. Considering that this assay does not require the quantification of subtle densitometric differences on the tracer-labelled cells, images

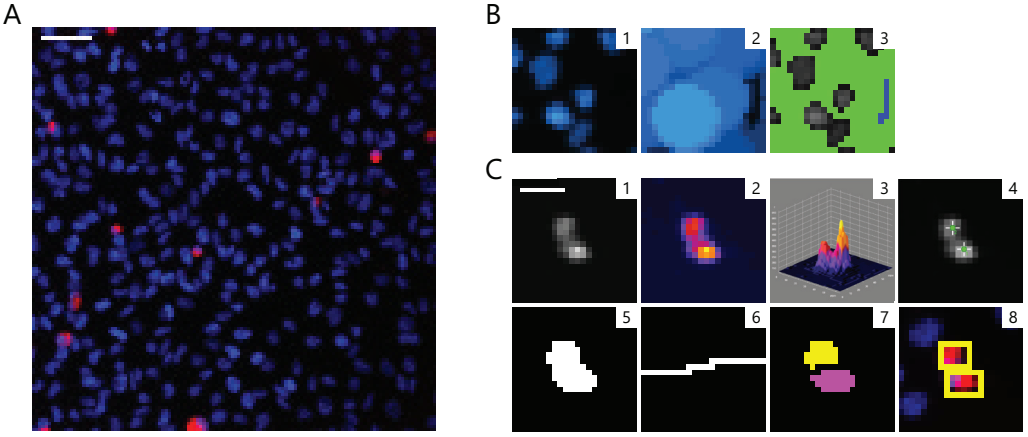

Figure 8. Bioimage analysis workflow for a static adhesion assay deployed for the assessment of N-cadherin-mediated adhesion on *in vitro* NSC cultures. (A) Representative field-of-view acquired throughout a cell adhesion assay. NSCs labelled with the DDAO-SE cell tracer (red) are left to attach to a confluent monolayer of NC-L929 fibroblasts overexpressing N-cadherin (DAPI, blue). The experimental and imaging setup aims to enable the extraction of the number of adhered cells relative to the monolayer area by means of an automated bioimage analysis workflow. Scale bar 50 µm. **(B)** Workflow for the segmentation of the counterstained monolayer. The nuclei on the foreground of the counterstain channel are mostly monolayer nuclei. However, the counterstain alone does not enable the segmentation of the complete monolayer (1). Thus, an estimated monolayer is depicted applying a maxima filter. Fiji's Cyan Hot LUT (2). Finally, the processed image is thresholded to obtain the monolayer binary mask. In the workflow pre-analysis mode, the monolayer nuclei retain their original greyscale, whereas the estimated monolayer are is color-coded in green, whereas the background is represented in blue (3). **(C)** Workflow for the segmentation of the cell tracer. The low resolution facilitates the segmentation of the DDAO-SE+ cells, except for those clumped. Scale bar 25 µm (1). The workflow uses the relative maxima on the image to identify potential cells (2-4). The image is displayed using Fiji's Fire LUT to visualize the different grey intensities across the cell bodies (2) and represented as a surface plot (3). Then, a semantic segmentation of the cells is computed (5), and the relative maxima (4) are used as markers to generate Voronoi territories (6), which are applied for the obtention of the cell instance segmentation (7). The pre-analysis mode of the workflow displays the bounding boxes of the segmented cells (yellow) on the merged, raw data (8).

are initially converted to 8-bits. This reduction in the greyscale range does not interfere with the cell counting and accelerates the calculation of other necessary features such as the coordinates of the local maxima found applying the prominence established by the user. Then, on one hand, a new image is created, and the maxima positions are defined as single-pixel objects to later divide the image into voronoi territories. On the other hand, greyscale images are normalized to a 0-1 range and segmented according to the threshold set by the user for this channel. Merged objects are separated according to the calculated voronoi boundaries. Objects below a minimum size determined by the user are rejected. Moreover, those touching the edges are rejected since it is not possible to determine their real size and might bias the results. This strategy was chosen due

to the difficulty of separating such small objects according to their convexity applying the basic watershed plugin within Fiji (**Figure 8C**). Finally, objects are filtered by the size range defined by the user (in pixels) in order to eliminate precipitates or other ill-segmented objects. It is possible to ask the macro to save the corresponding ROIs, which may be useful to visually check the output of the workflow, an increasing demand for data publication.

3.6. Output

The macro generates different outputs depending on the selected mode. The pre-analysis mode works with a field-of-view at a time and creates a two-image stack representing the segmentation of both the adhered cells and the subjacent monolayer. The first image merges the counterstain and the cell tracer channels and overlays the bounding box of the ROI obtained from the segmentation on the top of the corresponding adhered cells. Additionally, in order to visually check the monolayer segmentation output, in the second image the macro assigns a colour code to the counterstain greyscale image where: i) the nuclei pixels keep the values of the original greyscale image, ii) the artificially generated monolayer area is represented in green and iii) the remaining background is shown in blue. Conversely, the analysis mode is focused on the extraction of quantitative data. Therefore, the main output is a results table which is exported as a TXT file. The table contains metadata for its correct interpretation, as each row corresponds to one field-of-view. Moreover, the file contains both the data from the quality control metrics and the count of the tracer-positive cells and the monolayer area. Additionally, if checked, it also saves the ROIs from the cell tracer segmentation. As explained before, on both modes, the macro saves the actual set of parameters as a TXT file. This project can be loaded and applied to further analyses. Hence, once the pre-analysis generates a satisfactory output, the parameters can be easily imported to run the ultimate analysis. Furthermore, as long as new generated image datasets keep similar properties, the set of parameters applied on past analysis can probably be reused in forthcoming assays.

4. Case study: regulation of N-cadherin proteolysis in the SEZ by niche factors

The microscopy-based screening protocol was applied in a real cell adhesion experiment aimed to confirm that ADAM10 participates in the proteolysis of the N-cadherin present at the NSCs membrane, thus regulating their N-cadherin-mediated adhesion.

As previously indicated, the assay depends on two different cell cultures which have to be handled in order to be grown in parallel, a stable line of fibroblasts overexpressing N-cadherin (NC-L929) and *in vitro* neurosphere cultures. First, fibroblasts overexpressing N-cadherin (NC-L929) were seeded on flat, solid bottom, clear CELLSTAR® 96W Microplate (Sigma-Aldrich) at a density of $4x10^4$ *per* well in DMEM supplemented with 1% L-glutamine and 10% fetal bovine serum (see **Table 5** in **Material and Methods**). NC-L929 were incubated at 37 ºC and 5 % CO_2 and let grow till confluence (24-48 h after seeding). Once the monolayers were confluent, neurospheres were mechanically disaggregated on HBSS Hank's Balanced Salt Solution medium containing Hepes (5 mM) free of Ca^{2+} and Mg^{2+}. To test for the potential specific role of ADAM10, neurosphere cultures had been pretreated for 2 days with GI254023X (GIX, TOCRIS) at 50 µM, a potent ADAM10 inhibitory drug, or its vehicle (dimethyl sulfoxide, DMSO) before conducting the cell adhesion protocol. A specificity control with N-cadherin-blocking antibodies (NcadBlock) was also included. Individualized NSCs were then labelled with a membrane-permeant, fixable, far red fluorescent tracer (CellTrace Far Red DDAO-SE, ThermoFisher Scientific) at the manufacturer's recommended concentration. After 7 min at 37 ºC, DDAO-SE-containing medium was washed out and cells were resuspended in growing medium (with Ca^{2+}) and counted. Each sample was divided into two groups: half of the cells were incubated with the NcadBlock and the other half with isotype mouse immunoglobulins (IsoMsIgG). After 1 h of treatment, DDAO-SE-labelled cells were seeded onto the NC-L929 monolayer and let to attach for 1 h at 37 ºC. After this time, non-adhered cells were washed out (at least 3 washes with 5 min incubation in a Calcium-containing medium). At this point, cultures were fixed with 2 % paraformaldehyde (PFA) in phosphate buffer saline (PBS) during 15-20 min at 37 ºC. After fixation, cells were counterstained with DAPI (2 mg/mL in ddH_2O) for 5 minutes. Imaging was performed through the ICA-2k microscope as previously described, capturing a total of 49 fields-of-view *per* well with the 40x objective and a 1x1 binning (so the dataset had to be downsized later on with the developed preprocessing macro).

As expected, NcadBlock consistently reduced the NSC adhesion to the NC-L929 monolayer. Regarding the experimental condition, in case ADAM10 actually participates in the proteolysis and shedding of N-cadherin in NSCs, its inhibition would lead to increased levels of N-cadherin at the cell surface and, hence in enhanced adhesion. This was confirmed as the GIX-treated condition showed a higher count of adhered DDAO-SE-positive cells *per* monolayer (**Figure 9**).

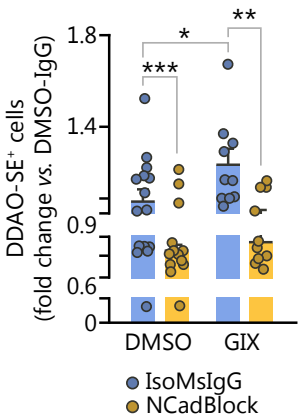

Figure 9. Quantification of the number of cells labeled with the DDAO-SE cell tracer adhered to the NC-L929 cell monolayer with respect to the monolayer area. Neurosphere were pretreated with the ADAM10 inhibitory drug GI254023X (GIX) or its vehicle (dimethyl sulfoxide, DMSO) to test the role of ADAM10 in the proteolysis of N-cadherin. A specificity control with N-cadherin-blocking antibodies (NcadBlock) or isotype mouse immunoglobulins (IsoMsIgG) was also included. The graph shows the results with respect to the values obtained with the control condition, i.e., cells pre-treated with DMSO and IsoMsIgG. The data bars correspond to the mean ± s.e.m and each point corresponds to each analyzed mouse.

* p-value<0.05; ** p-value<0.01; *** p-value<0.001

CHAPTER 2. BIOIMAGE ANALYSIS OF NSC PROLIFERATION AND APOPTOSIS

1. Biological background: image-based methods to assess proliferation and apoptosis

Cell proliferation and programmed cell death are undoubtedly two of the most studied processes in the field of cell biology. In the stem cell field, in particular, cell cycle regulation is central to understanding key stem cell properties such as their maintenance through the reversible transition between quiescence and activation or the switch from pluripotency to differentiation (Liu *et al.*, 2019; Cho *et al.*, 2019). Apoptosis, on the other hand, has emerged in the last years as an important topic in the study of stem cells since it has been found that apoptotic bodies from surrounding cells can induce stem cell proliferation (Brock, 2019) or that specific apoptotic mediators may play a role in stem cell differentiation (Fujita *et al.*, 2008; Ryoo & Bergmann, 2012; Ryu *et al.*, 2016). Classically, the study of cell proliferation and apoptosis has relied in microscopy-based methods or in flow cytometry analysis (Towne *et al.*, 2012; Yin *et al.*, 2017 Fathi *et al.*, 2019). In this chapter we will focus on methods that can be performed by image-based analysis.

Among the methods suitable to assess cell proliferation through microscopy-based analysis, pulse-chase experiments with nucleoside analogues stand out for its reliability and applicability on screening assays. This approach is based on the detection of traceable nucleosides incorporated to DNA while cells undergo the S phase of the cell cycle. To this aim, cells are incubated with modified pyrimidines, which perform as thymidine analogues, for a short period of time (pulse). After that, cells can be immediately fixated and processed for the detection of the labelled DNA, which provides an estimation of the overall proliferation in the sample. Conversely, fixation and detection can be delayed a variable amount of time to let cells continue dividing, now in the absence of the analogue (chase). During this period, each further mitosis will result in half of the tagged DNA to be distributed among the daughter cells, so the initial label gets 'diluted' and becomes undetectable after several rounds of division. However, those cells that stopped dividing after the pulse (because of terminal differentiation, return to quiescence or arrest in G1, for instance) will remain labelled and be detected. Different regimes of pulses and chase times can be applied depending on the specific question to be addressed (for examples see Ferrón *et al.*, 2007; Ponti *et al.*, 2013; Belenguer *et al.*, 2020).

Halogen-containing pyrimidines, such as BrdU (5-bromo-2′-deoxyuridine) (Eidinoff, Cheong & Rich, 1959) have been used for decades to this aim, requiring the denaturation of the DNA to reveal their presence by means of immunostaining with specific antibodies. Conversely, the more recently developed EdU (5-ethynil-2′-deoxyuridine) (Chehrehasa *et al.*, 2009) can be directly detected by means of bioorthogonal reactive chemistry. In this copper-catalyzed "click" reaction (Kolb, Finn & Sharpless, 2001; Best, 2009), the alkyne group present in the EdU molecule forms a covalent bond with a fluorophore-linked azide, making unnecessary the use of antibodies or antigen unmasking by heat or acid treatment. Both methods are equally sensitive but, in the recent years, EdU has become a popular alternative for microscopy-based screening assays (Mandavilli, Yan & Clarke, 2018) due to its ease of use, the high specificity of the "click" reaction, which generates stable and inert products, and its compatibility with multiple probes.

From the image analysis point of view, it is important to highlight that cells can incorporate different amounts of nucleoside analogue, depending on how advanced the S-phase was when the pulse started and the number and frequency of pulses administered. Additionally, if a chase period is followed, cells will 'dilute' the label according to their division rate. As a result, diverse patterns of nuclear staining can be found among samples ranging from an irregular punctate pattern of variable density and intensity to a full strong nuclear staining .

Apoptosis is a form of cell death triggered through the activation of highly regulated proteolytic cascades and characterised by stereotypical biochemical and morphological features (D'Arcy, 2019). Apoptotic processes are divided into two main subtypes, intrinsic or extrinsic apoptosis, according to the biochemical pathways involved in their regulation. On the one hand, intrinsic apoptosis depends on the permeabilization of the mitochondrial outer membrane, releasing mitochondrial proteins which are responsible for the activation of initiator caspase 9 (Chipuk, Bouchier-Hayes & Green, 2006). On the other hand, extrinsic apoptosis is mediated by two different type of membrane receptors: i) the presence of death receptors ligands lead to the activation of initiator caspases 8 and 10, ii) whereas the absence of dependence receptor ligands leads to the activation of initiator caspase 9 (Tang *et al.*, 2019).

Execution caspases 3, 6 and 7 are common effectors for both intrinsic and extrinsic pathways, and are cleaved by upstream caspases 8, 9 or 10 in order to initiate apoptosis (McIlwain, Berger & Mak, 2015; Galluzzi *et al.*, 2016). Due to its central role on the apoptosis signalling pathways, common effectors such as caspase 3 and 7 (also known as caspase-3-like proteases) are well established biomarkers for the detection of apoptotic cells (Mandavilli, Yan & Clarke, 2018) and can be easily visualized in the

nuclei by immunochemistry with the great variety of commercially available antibodies that specifically distinguish the activated form of each caspase from its pro-caspase zymogen.

2. Bioimage analysis

We have developed a bioimage analysis workflow to analyse a high content screening assay for the assessment of cell proliferation and apoptosis. It has been automated in a ImageJ macroinstruction which can be downloaded adding the NeuroMol Lab update on the Fiji updater. Requirements, installation and usage documentation, as well as an example image dataset, is to be found in GitHub (https://github.com/paucabar/cell_proliferation_assay).

This workflow is a new version of a previous script (Carrillo-Barberà, Morante-Redolat & Pertusa, 2019) which runs faster and includes new functionalities. Despite the fact that the workflow has been assembled in a single macro, some other macros from the NeuroMol Lab site may be needed to perform optional pre-processing steps. In its design, we have taken into account the following considerations:

- Since the assay relies on densitometric data, it is necessary to take into account that images acquired throughout an optical microscope are affected by vignetting, which is estimated to cause a variation on the effective illumination of 10-30 % between the different image regions (Smith *et al.*, 2014). In order to improve the quality of the data it is possible either to correct the experimental image dataset on a pre-processing step or to determine a region with minimal illumination variation in order to exclude the rest for the analysis (Jost & Waters, 2019). We provide optional pre-processing workflows to address the vignetting issue (see **2.1**).

- Image acquisition has been performed throughout the ICA-2k. Thus, it is necessary to extract the information contained on the filename metadata according to the microscope convention (see **2.2**).

- It is possible to parametrise the workflow in order to adjust the analysis for different datasets. With the aim to facilitate the selection of the workflow and its parameters, the macro includes a test mode that allows the user to test different parameter sets on a subset of images. Moreover, the current parameter set can be saved for their use in future analyses (see **2.2** and **2.4**).

- The assay collects densitometric data of different fluorescent probes that label molecules located, totally or partially, on the cell nuclei but display diverse staining patterns. In consequence, segmentation is performed on the nuclear counterstain channel. In order to achieve an accurate nuclei segmentation, the macro includes two differentiated strategies: a workflow based on classical image processing methods and a deep learning (DL) approach (see **2.3** and **2.4**).
- The use of high-throughput microscopes enables the acquisition of large dataset in an automated way. Despite its advantages, this imaging approach can also lead to the capture of ill-quality images. Since the analysis of such screening datasets preclude the visual inspection of the images, it becomes necessary to apply methods for the automatic identification and exclusion of those images, in order to prevent a misled interpretation of the results (see **2.5**).

2.1. Illumination correction (recommended)

The workflow includes an optional step aimed to correct uneven illumination. Retrospective multi-image methods are the common choice to perform the illumination correction on screening approaches (Caicedo *et al.*, 2017), since the strategy benefits from the large image datasets which are typically acquired for these experiments. However, this method requires the previous generation of illumination correction functions (flat-field images). Therefore, we decided to create an independent workflow to perform this task which is also available on the Neuromol Lab update site **[NeuroMol Lab > other macros > Illumination Correction]**.

Our workflow uses BaSiC, a retrospective multi-image method which has shown a series of advantages compared with other previously developed tools. Among the BaSiC qualities it stands out that requires fewer images to achieve a higher accuracy and is more robust in the presence of image artefacts (Peng *et al.*, 2017). The macro uses the BaSiC plugin implemented within Fiji to calculate the flat-field image of each channel. The workflow starts extracting the metadata to identify the different channels on the dataset. Then, all the images corresponding to the same channel are imported as a stack to be used as the BaSiC input. The flat-field calculation is relatively fast when working with several hundreds of images, but the process is RAM-consuming so larger

datasets can slow down the performance if working with a regular laptop. In the end, the generated correction functions are saved as TIF files that will be needed during the initial steps of the main workflow. Nonetheless, in case the user prefers to generate the corrected images before running the main analysis workflow, the optional correction macro also allows to directly apply the calculated correction functions, i.e., to divide each experimental image by its corresponding flat-field function (see **Figure 10A**).

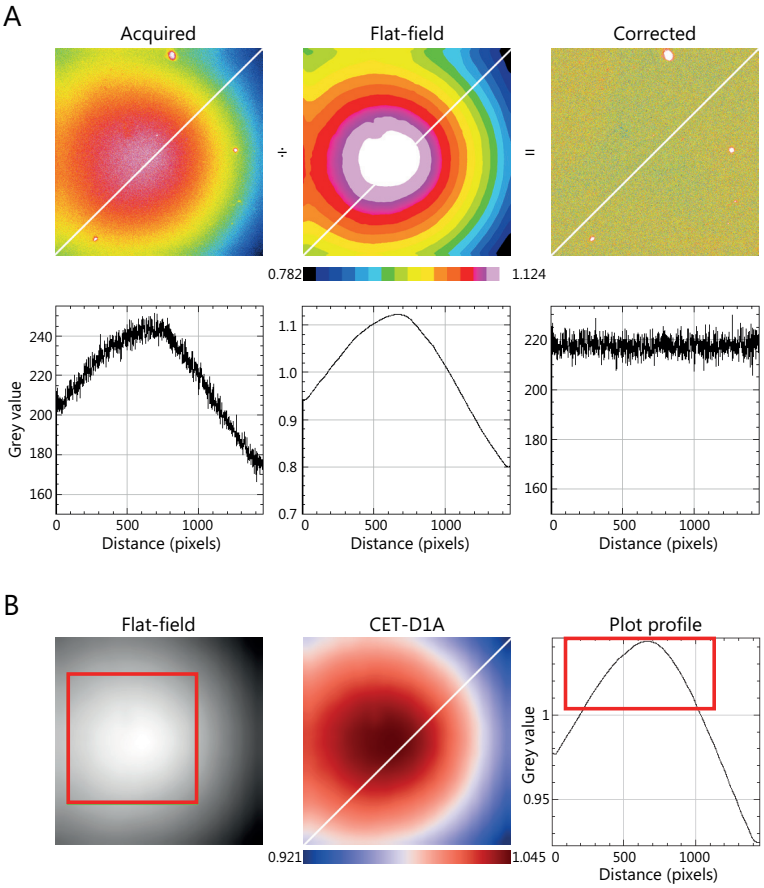

Figure 10. Applications of the calculated illumination correction functions, also referred to as flat-field images. (A) Illumination correction is performed dividing the acquired image by the calculated flat-field (top). In order to show the changes on the effective illumination across the different images (acquired, flat-field, corrected), the intensity profile of each image is plotted (bottom). Plot profiles were generated over a 1-pixel thick line crossing the images from the left-bottom to the right-top corners (the line is represented in white) in Fiji. For a better representation of uneven illumination, an empty field-of-view from a real high-content imaging experiment has been selected, which does not contain cells but some small debris. The flat-field image was calculated by means of the BaSiC retrospective multi-image method from about 3,000 images acquired on the same channel (FITC) and multiwell plate. Images display Fiji's 16_colors LUT. **(B)** Flat-field images and their plot profiles can be used to determine an area with minimal illumination variation (green boxes) with the aim to restrict the bioimage analysis to these regions. The flat-field is also displayed using the CET-D1A LUT, from the Fiji update site NeuroCytoLUTs .

Alternatively, it is possible to use the obtained correction functions to define an analysable region around the centre of the optical axis (usually in the centre of the image) where illumination is most uniform, thus rejecting those peripheral areas with evident attenuated illumination. To this aim, the use of look-up tables (LUTs) for the inspection of the illumination correction functions or the calculation of intensity profiles across the flat-field images may be useful approaches to determine regions showing a minimum illumination variation (see **Figure 10B**). Once a selection has been defined, the NeuroMol Lab site includes a macro which asks for a rectangular ROI in order to crop an entire dataset **[NeuroMol Lab > other macros > Rectangle Crop Batch]** before proceeding to the analysis.

2.2. Metadata extraction and parametrisation

Metadata is extracted from filenames according to the ICA-2k naming pattern (see **section 3.2** on **Chapter 1**). In addition, parametrisation is performed throughout a GUI similar to the one described for the cell adhesion assay (see **section 3.3** on **Chapter 1**), but displaying a different set of parameters.

The main dialogue window starts by asking the user to select either the pre-analysis (test) or the analysis mode and to choose the directory containing the experimental dataset. Then, the macro offers two different approaches to accomplish segmentation. On the one hand, a classical filter-based workflow for the detection and segmentation of the nuclei. On the other hand, a method based on StarDist, a DL approach designed for the prediction of star-convex polygons especially suitable for the segmentation of cell nuclei on microscopy images (Schmidt *et al.*, 2018; Weigert *et al.*, 2020). A new segmentation protocol can be generated from scratch (parameters will be set in the next dialogue window). Conversely, a previously generated file containing all the parameters set can be loaded. The macro also allows to import illumination correction functions, either generated using the aforementioned NeuroMol Lab macro or a different method. If checked, the user must provide the directory containing the flat-field images. Finally, it is also possible to set the workflow to save the ROIs obtained from the segmentation of the nuclei (only for the analysis mode).

Next, a new dialogue window displays all the necessary parameters for image processing. Some of the parameters are common to both segmentation choices, such as the channel metadata and the corresponding channel where to apply the illumination correction in case flat-field images were loaded. Other parameters, on the contrary,

are specific of each segmentation approach and are only displayed depending on the chosen method. All the adjustable parameters are summarised in **Tables 8** and **9** and, for a better understanding, will be explained later on in their corresponding method section. Finally, the next dialogue window prompts the user to select all or just a subset of wells from the loaded dataset to run the analysis. Pre-analysis mode works slightly differently since it enables the visualization of the segmentation output obtained applying the established parameters on a series of randomly picked images. In order to do so, this mode includes an extra dialogue window where the user can set the number of images per well to be tested as well as set some parameters related to the visualization.

Table 8. User-adjustable parameters found in the bioimage analysis workflow for the quantification of cell proliferation and apoptosis (filter-based approach).

Parameter	Variable type	Default
Counterstain channel	String (set from array list)	First element on the list
Nucleoside analogue channel	String (set from array list)	First element on the list
Marker 1 channel	String (set from array list)	None
Marker 2 channel	String (set from array list)	None
Normalize	Boolean	Yes
Gaussian filter	Float (sigma)	2.0
AutoThreshold Method	String (set from array list)	MaxEntropy
Erode	Integer (iterations)	2
Open	Integer (iterations)	2
Watershed	Boolean	Yes
Size	String (min-max)	0-Infinity
Counterstain flat-field	String (set from array list)	None
Nucleoside analogue flat-field	String (set from array list)	None
Marker 1 flat-field	String (set from array list)	None
Marker 2 flat-field	String (set from array list)	None

Table 9. User-adjustable parameters found in the bioimage analysis workflow for the quantification of cell proliferation and apoptosis (StarDist).

Parameter	Variable type	Default
Counterstain channel	String (set from array list)	First element on the list
Nucleoside analogue channel	String (set from array list)	First element on the list
Marker 1 channel	String (set from array list)	None
Marker 2 channel	String (set from array list)	None
Overlap threshold	Float (0.00-1.00)	0.40
Size	String (min-max)	0-Infinity
Counterstain flat-field	String (set from array list)	None
Nucleoside analogue flat-field	String (set from array list)	None
Marker 1 flat-field	String (set from array list)	None
Marker 2 flat-field	String (set from array list)	None

2.3. Segmentation strategies

The macro starts by applying the illumination correction on the specified channels. In order to do this, each image is divided by its corresponding flat-field image. Additionally, there is an optional step within the filter-based workflow to normalize the counterstain images allowing a 0.1 % of saturated pixels, whereas the StarDist workflow is set to always normalize the images. The filtering approach is based on classical image processing algorithms, so it includes some of the most common steps on this kind of strategies (see **Table 8**). Each of the components can be set by the user during the parametrisation. First, the counterstain image is smoothed by applying a Gaussian filter and thresholded to generate a binary mask. Then, objects are submitted to operations with the binary mask to improve the segmentation (i.e., erosion or open operations). During the parametrisation step, the user needs to set the filter radius (sigma), select a thresholding algorithm among those available on the Threshold plugin and establish the iterations of the binary operations. Finally, if the option is checked, clumped objects are separated by means of the default watershed algorithm, which uses as markers the ultimate eroded points (**Figure 11A**).

Alternatively, StarDist performs the instance segmentation of nuclei applying a strategy that is specifically suited to this kind of objects (**Figure 11B**). It generally

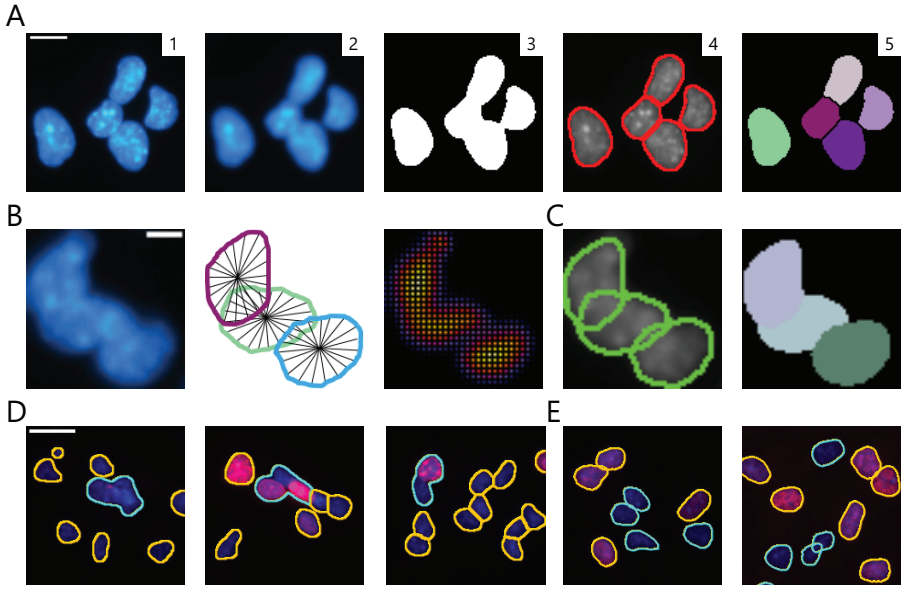

Figure 11. Bioimage analysis workflow for a cell-based proliferation and apoptosis assay on in vitro NSC cultures. (A) Filter-based approach for the segmentation of nuclei. Segmentation is performed on the counterstain channel. Scale bar 10 µm. Cyan Hot LUT (1). The image is smoothed using a Gaussian filter (2) before applying a thresholding method to obtain a semantic segmentation (3). Finally, a watershed operation is performed to separate clumped objects. The final instance segmentation is displayed as an overlay (4) and labelled image (5). Labels are colour-coded with the glasbey on dark LUT. **(B)** StarDist is a generalist deep learning approach which predicts object probabilities and star-convex polygons parametrised by radial distances for the segmentation of nuclei. Figure adapted from Schmidt et al., 2018. Scale bar 5 µm. **(C)** The StarDist method can be set to enable the predicted instances to overlap (left) or to generate non-overlapping labels (right, labels are colour-coded with the glasbey on dark LUT). **(D-E)** The pre-analysis mode can be used to check the segmentation performance. Additionally, it is possible to label the instances (coloured outline) setting thresholds based on object features. Scale bar 20 µm. **(D)** Solidity is a useful feature for the detection of merged nuclei. Objects with a solidity greater than 0.9 are outlined in orange, whereas those instances with a lower score are outlined in cyan. **(E)** Densitometric features are typically used for the classification of cells labelled with fluorescent probes. A mean grey value threshold has been established on the red channel for the classification of cells according to their EdU content.

obtains better results than other DL approaches that are based either on i) computing a semantic segmentation in order to form objects by splitting the obtained mask or ii) predicting bounding boxes of individual objects which are then submitted to a local semantic segmentation. Conversely, for each pixel, StarDist predicts the probability of being part of an object and the distance to the object boundary along a series of radial directions. Thus, a star-convex polygon is proposed as a candidate region per every pixel inside an object, which generates a large number of redundant shapes which are

then filtered using non-maximum suppression in order to prune those regions that likely correspond to the same object. As a supervised approach, it is necessary to annotate a ground-truth to train a StarDist model. However, there are also pre-trained models for the segmentation of 2D nuclei, e.g., for fluorescent (single channel) or haematoxylin & eosin (RGB) images. In the case of fluorescent images, the model was trained on labelled images from diverse microscopy modalities (Schmidt *et al.*, 2018). However, this pre-trained model does not ensure a proper segmentation of any fluorescent image, since it can be affected by several factors such as the resolution of the image.

In our experience, the fluorescent pre-trained model provided within StarDist accurately segments nuclei of NSCs, which are smaller than those of other cell types in our *in vitro* assays, on images acquired by means of the ICA-2k using the 40x objective and a 2x2 binning. Therefore, our macro runs the StarDist 2D plugin included in Fiji set to use the pre-trained 'Versatile (fluorescent nuclei)' and to send the predicted nuclei as ROIs to the ROI Manager. This way, even highly clumped nuclei can be properly individualized and segmented, since the algorithm estimates each ROI including its overlapping region with other nuclei (overlap threshold percentage can be set during the parametrisation step) (**Figure 11C**). As a supervised learning approach, it relies on annotated ground truths, which implies an additional effort in exchange for enabling its application by users without image processing prior knowledge.

Finally, after all the instances have been obtained, either through the filter-based or the StarDist workflow, some objects are rejected before proceeding to the feature extraction. Specifically, both nuclei touching the image borders and those not meeting the size threshold set on the parametrisation step are removed. Since segmentation by filter approach works with binary masks whereas StarDist method obtains ROIs, this post-processing step requires different strategies. Unwanted binary masks are easily removed using the Analyze Particles plugin which already includes an option to remove border-touching objects and a size filter. However, this is not as straightforward when working with ROIs. For this reason, we have built two dedicated functions: the size selection function measures the area of the ROI set in order to filter them, whereas the border kill function obtains the bounding rectangle coordinates in order to identify the border-touching ROIs and discard them.

2.4. Quantification and output

The macro generates different outputs depending on the selected mode. The pre-analysis mode generates a stack of RGB images, each one composed by the merge of the

nuclear counterstain and the nucleoside analogue images of a randomly picked field-of-view. In order to facilitate the visual inspection of the segmentation output, the outlines of the segmented objects are also drawn on the image with a colour code according to the visualization settings introduced by the user during the parametrisation step (**Figure 11D**). This allows to distinguish between objects according to a selected measurement (e.g., densitometry parameters or shape descriptors) and manually set threshold. For example, it is possible to label objects with a low solidity, which may be useful, e.g., to set filters for the rejection of ill-segmented objects, such as merged or split nuclei (to be applied after the bioimage analysis workflow). Alternatively, this can be used to look for simple rules to separate cell populations according to fluorescent staining signals (**Figure 11E**).

The output of the analysis mode, on the contrary, is quantitative information extracted per image and per object. On the one hand, the script calculates some of the image quality metrics already described in **Chapter 1**, **section 3.4** using the counterstain channel. On the other hand, the macro redirects either the obtained binary masks or the ROIs (depending on the segmentation method) to each channel grey image to obtain densitometry parameters (mean intensity and integrated density). Counterstain nuclear channel is not measured since it is only used for segmentation. In addition, size and shape descriptors are calculated since, as aforementioned, these parameters can be applied for the rejection of ill-segmented objects, but also for the identification of cell phenotypes. Finally, the analysis workflow generates a CSV results table containing all these measurements per each segmented nucleus. Furthermore, since field-of-view quality metrics are redundant on the previous table (i.e., all the nuclei from the same image show the same quality scores), these are also stored on a separated CSV file containing only per image measurements. Moreover, if set by the user, the analysis mode saves the obtained ROIs corresponding to each field-of-view as ZIP files. Both modes generate a CSV file containing the workflow settings, so it can be imported for future analysis.

2.5. Field-of-view quality control using a machine learning approach (optional)

Complementary to the basic quality metrics we have included so far in our workflows, we have developed a separated pipeline built on CellProfiler to classify the images in a dataset according to their quality. Following the metadata extraction, the pipeline uses the CalculateImageQuality to compute a series of metrics on the nuclear counterstain channel. These parameters include intensity (field-of-view intensity stats),

saturation (percentage of pixels with the maximum or minimum intensity) and blur (e.g., power log-log slope, focus score assessed or image correlation) metrics (Bray *et al.*, 2012; Caicedo *et al.*, 2017). Then, the FlagImage module is used to tag images as saturated or non-saturated and blurred or non-blurred. Images are flagged as saturated when the percentage of pixels with the upper value represents more than the 0.1 % of the total pixels. Conversely, blur metrics, more complex to be interpreted, are applied according to a set of rules established by means of a supervised ML algorithm.

In order to train the classifier, it was necessary to generate the annotation of two balanced sets of images, i.e., in-focus and blurry images. Nevertheless, as expected if capture settings are correctly established, out-of-focus images in the dataset are scarce, so it is difficult to assemble a sufficient amount of blurry images for the training. Thus, along with the experimental dataset obtained to test the macro, we decided to generate two additional datasets composed of intentionally slightly and severely out-of-focus images, to be used in the training. Then, a combined dataset was obtained mixing more than 200 fields-of-view of each of the three acquisitions (experimental, slightly blurred and severely blurred).

Classifier was trained on the Fast Gentle Boosting algorithm provided within CellProfiler Analyst (Jones *et al.*, 2008). To this aim, we used a similar pipeline to calculate the image quality metrics computed from the combined dataset and to export them into a SQL database. On CellProfiler Analyst, random images were fetched and annotated as in-focus or out-of-focus to train the classifier, which was tested on a different dataset of 100 annotated images. The performance of the classifier proved to be robust, with all the blurry images correctly flagged whereas in-focus fields-of-view showed a 0.96 true positive rate (see **Figure 12**). These results were achieved using a single metric, the power log-log slope.

3. Case study: NSC response to DNA damage

The workflow performance was tested on a real cell proliferation (by a short EdU pulse) and apoptosis (by detection of activated caspase 3 by immunocytochemistry) screening. We selected a strategy combining BaSiC-computed flat-field images with StarDist for illumination correction and segmentation, respectively. The goal of the assay was to evaluate the response of NSCs to DNA damage *in vitro*, which was induced by short exposure to the alkylating agent methyl methanesulfonate (MMS).

To do so, previously grown neurospheres were enzymatically disaggregated using Accutase® Cell Detachment Solution to obtain individual NSCs. Cells were seeded on

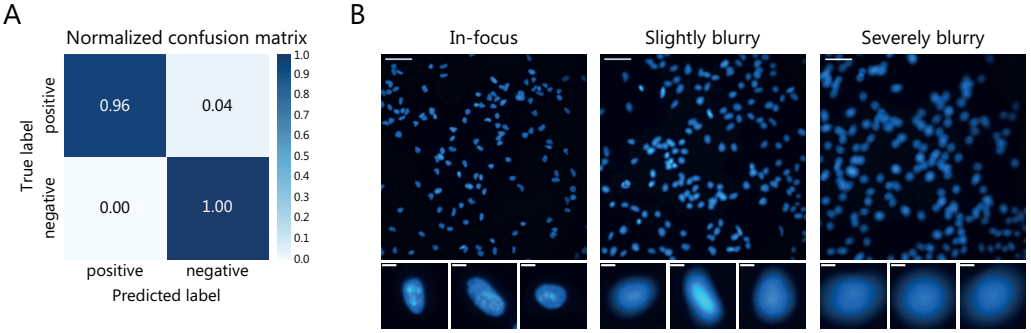

Figure 12. Prediction of blurring quality control (QC) rules using machine learning (ML). (A) A ML classifier was trained to distinguish in-focus (positive) from blurred (negative) images and tested on a set of images annotated as positive or negative. The normalized error matrix represents the performance of the QC rules generated by the supervised ML classifier, as each row represents the instances from an annotated class (True label), whereas each column represents the instances from a classifier predicted class (Predicted label). **(B)** Representative images from a fabricated dataset generated for the training of the classifier. To this aim three different subsets were generated acquiring the counterstain channel of cultured cells: i) in-focus, ii) slightly blurry and iii) severely blurry images. Both slightly and severely blurry fields-of-view were annotated as negative, whereas in-focus cells were annotated as positive. Scale bar 50 µm. Zoomed nuclei are placed below their corresponding field-of-view. Scale bar 5 µm. Counterstain is displayed using Fiji's Cyan Hot LUT.

Matrigel®-coated, flat, solid bottom, clear 96-well microplates at 2 x 10^4 cells *per* well in growing medium. Cells were incubated for n 24 h at 37 ºC in a 5 % CO2 humidified incubator in NSC medium supplemented with mitogens before treatment. Then, cells were exposed to either a low (0.005 %) or a high (0.02 %) concentration of MMS, for 4 h. At the end of the treatment, NSCs were submitted to a 1 h EdU pulse and fixed with 4% PFA in cytoskeletal buffer (Hua & Ferland, 2017) at 37 ºC during 20 min. EdU was prepared and its presence revealed by click chemistry combined with Alexa Fluor® azide according to the manufacturer's instructions (Thermo Fisher Scientific). Cells undergoing apoptosis were labelled by means of immunocytochemistry with cleaved caspase 3 specific primary antibodies. To this aim, once fixed, samples were blocked at room temperature for 1 h in PBS (0.9% NaCl in PB) with 0.2 % Triton X-100 supplemented with 10 % Fetal Bovine Serum (FBS). Cells were incubated overnight at 4 °C in a 1:400 dilution of primary rabbit-polyclonal antibody for cleaved caspase 3 (Asp175) (Cell Signaling). Then, cells were incubated in a 1:600 dilution of secondary antibody Alexa Fluor® anti-rabbit (Jackson InmunoResearch) for 45 min at room temperature. Finally, nuclei were stained with DAPI, as explained before. Image acquisition was performed with the high content microscope ICA-2k using a 40x objective and 2x2 binning. The dataset was acquired within 4 different channels to image: i) nuclei counterstain, ii) EdU, iii) cleaved caspase 3 and iv) brightfield. Focal plane was established using laser autofocus on the DAPI channel as reference, slightly adjusting the z position for the different channels.

As expected, treatment effects on cell proliferation were dramatic. While low MMS led to an important decrease in EdU positive cells, high MMS caused a complete cell cycle arrest (**Figure 13A**). Moreover, we observed an evident drop of the mean intensity and integrated density values of the EdU channel in the low MMS treated EdU⁺ cells (**Figure 13A**, lower panels). This is not surprising since a well-established cellular response to moderate DNA damage is to induce a transitory cell cycle arrest to let the DNA repairing machinery overhaul the situation.

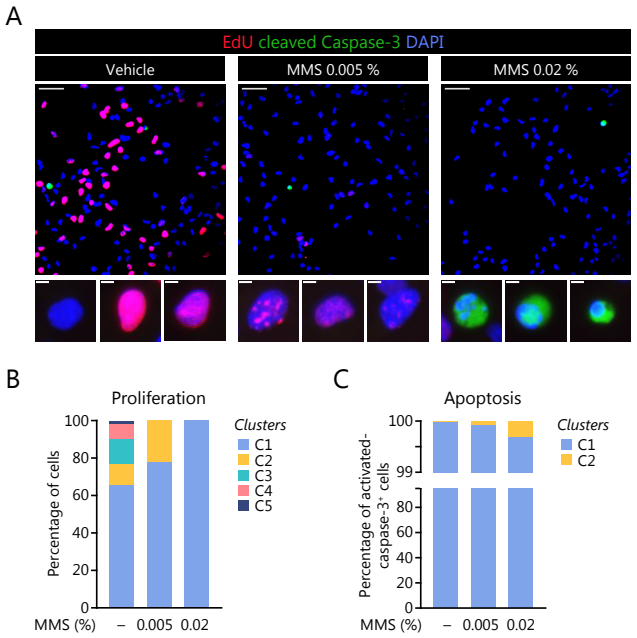

Figure 13. Proliferation and apoptosis results. (A) Representative images of proliferating NSC cultures in adherent conditions after treatment with low (0.005%) or high (0.02%) concentration of the genotoxic drug MMS. DMSO was used as vehicle. Immunocytochemistry for EdU (red) as a proliferation marker and cleaved Caspase-3 (green) as an apoptotic read-out (upper panels, scale bar 50 µm). DAPI (blue) was used to counterstain nuclei. Single-cell high-magnification images of different patterns of DAPI (EdU--cleaved Caspase 3-), EdU and cleaved Caspase-3 staining are shown (lower panels, scale bar 5 µm). **(B)** Automatic stratification by the k-means clustering method to analyse proliferation of MMS-treated cells. The algorithm divides cells into five clusters (C1-5), where non-cycling cells (EdU-) are allocated in C1. **(C)** Automatic stratification by the k-means clustering method to analyse apoptotic cell death after MMS treatment. The algorithm divides cells into two clusters: C1, non-apoptotic cell ; C2, apoptotic cell.

In case DNA integrity is successfully restored, proliferation is resumed whereas apoptosis or senescence are triggered if reparation fails (Meek, 2009). As a complementary approach to study this phenomenon, we decided to perform an automatic stratification of the cells in the sample by means of the k-means clustering method. The algorithm was set to divide cells into five clusters (C1-5), which led to non-cycling cells (EdU^-) being allocated in C1, whereas cycling cells were distributed among the remaining four clusters according to their EdU signal (C2 to C5 from lower to higher intensity). As shown in **Figure 13B**, proliferative cells in low MMS condition were preferentially allocated in C2, most probably due to the transient interruption of the S-phase. Regarding apoptosis, it is important to highlight that it is an extremely rare phenomenon in NSCs cultured in regular *in vitro* conditions (less than 0.03 %). Therefore, despite the fact that low MMS caused a 2.5-fold increase and high MMS a 10-fold increase, the highest registered apoptosis rate did not surpass the 0.4 % (**Figure 13C**).

CHAPTER 3. BIOIMAGE ANALYSIS FOR THE STUDY OF NSC CLONAL CAPACITY AND SELF-RENEWAL

1. Biological background: the study of NSC clonality and self-renewal in neurosphere formation assays

NSCs, as introduced before, are defined by their clonal and self-renewal capabilities and their multipotent nature. The development since the early nineties of the *in vitro* culture conditions of these stem cells (Reynolds & Weiss, 1992) has enabled the *in vitro* assessment of their defining characteristics. On one hand, NSC multipotency can be evaluated by means of a clonal differentiation assay in which the presence of an adherent substrate and serum, along with the withdrawal of mitogenic stimulation triggers the production of all three differentiated neural cell types. On the other hand, both clonality and self-renewal assessment rely on the controlled formation of floating clonal aggregates known as neurospheres during the called 'neurosphere formation assay'. The assay starts obtaining individual cells either from the dissection and dissociation of the SEZ tissue or from the disaggregation of previously grown neurospheres. Then these cells are seeded at a standardised cell density in multi-well plates in a defined serum-free medium supplemented with mitogens. After several days *in vitro* (DIV), the number of formed neurospheres accounts for the clonal capacity of the culture, whereas their disaggregation and re-seeding in further rounds of neurosphere formation provides information about their self-renewal (Belenguer *et al.*, 2016). Due to the nature of this assay, the most crucial parameter to be taken into account is cell density. Excessively high cell densities lead to cell aggregation and neurosphere coalescence, which must be avoided in order to ensure that each formed neurosphere is a clone originated from a single cell. Additionally, paracrine signals may influence the proliferation of the culture. There exist two main approaches to achieve clonality on an *in vitro* cell culture, single-cell or low-density assays.

Single-cell assays ensure true clonal density since they are performed by culturing individual cells independently, i.e., seeding just one cell per well. These pure clones can be obtained either by means of limiting cell dilutions or using cell separation methods to isolate and handle individual cells such as Fluorescence-Activated Cell Sorting (FACS). However, these procedures are not always easy or convenient to perform. Furthermore, cell separation methods can be detrimental to the cell viability which may bias the output of the assay. Very-low-density assays, on the other hand, are a straightforward alternative that, if well conducted, may also generate consistent results. It has been demonstrated by our laboratory and others that a cell density of less than 5 NSCs *per*

µL (up to 1,000 cells *per* well in a conventional 96-well plate), allows the reproducible formation of clonal neurospheres from individual cells without signs of aggregation (Ferrón *et al.*, 2007). Nonetheless, when working with highly proliferative conditions or cell phenotypes even a lower cell density may be required. To differentiate these assays from the genuinely clonal ones, they are commonly referred as 'semi-clonal' or, more correctly 'pseudo-clonal' assays. Besides the critical role of cell density, other issues also require special attention when setting the assay. Firstly, it is critical to ensure the complete disaggregation of the tissue or pre-existing neurospheres to guarantee that all the seeded cells have been individualized. Additionally, cells must be uniformly distributed along the culture surface upon seeding or at least separated enough to avoid neurosphere contact. Finally, it is of paramount importance to keep the multi-well plates in a flat evenly levelled incubator tray, to minimize possible vibrations and to refrain from manipulating them until the neurospheres have been formed. Otherwise, there is a great risk of aggregation and hence underestimation of the neurosphere number (Ferrón *et al.*, 2007; Belenguer *et al.*, 2016).

Independently of the chosen strategy, the aim of this assay is to quantify the number of neurospheres formed, usually after 5-7 DIV, relative to the number of individual seeded cells (or to the number of seeded wells in single-cell assays). Provided that NSC cultures are considered of heterogeneous nature in terms of both neurosphere forming capacity and proliferation rate, not all of the seeded cells give rise to a clone. This is due to the fact that *in vitro* culture conditions keep a population of self-renewing NSCs but cannot prevent the generation of committed progeny as well. This is the case of transit amplifying progenitor cells (Bjornsson *et al.*, 2015; Bond, Ming & Song, 2015), a highly proliferative subpopulation of progenitors that has been reported that are able to generate neurospheres, albeit just for a few passages (Doetsch *et al.*, 2002; Reynold & Rietze, 2005; Belenguer *et al.*, 2020). As a consequence, only truly self-renewal NSCs will be able to form neurospheres in each passage and ensure the long-term expansion of the culture.

The procedure to quantify the outcome of neurosphere assays has typically been the direct observation of the culture plate through a phase-contrast inverted microscope, so researchers score the number of clonal aggregates by visual inspection as they manually scroll through the multi-well plate. Apart from being tedious and time-consuming, especially in experiments with several technical and biological replicates and experimental conditions, it requires a certain training and is not devoid of observer bias. Otherwise, in some experimental paradigms, besides the number of clones, the size of the formed neurospheres might also be informative and help to characterize a particular

phenotype. Changes in the proliferative rate or in the survival of cells in the culture, for instance, might lead to changes in the size of the formed clones, even when their number remains constant between conditions. It has also been reported that the most self-renewing NSCs might give rise to bigger neurospheres (i.e., more than 100 microns of diameter) (Louis *et al.*, 2008). However, neurosphere size is very dependent on the culture conditions and days of incubation. On the other hand, changes in neurosphere size might be deceiving since there is not a direct correlation between proliferative rate and clonal and self-renewal capacity. Therefore, neurospheres size must be taken in consideration with caution. In any case, this measure cannot be directly obtained during the manual counting of neurospheres as described before. It would require to capture representative images of the culture surface and the subsequent measure of the size of the sampled neurospheres.

2. Experimental and imaging setup: screening-like imaging of pseudo-clonal neurosphere formation assays

For our assay, we chose a pseudo-clonal approach because it is much easier to perform on a daily basis in a regular cell culture lab without the need of cell sorting equipment and requires just minor cell manipulation. However, in order to optimize the analysis and allow the simultaneous and automatic assessment of both the number and size of the neurospheres, we decided to develop a screening-like imaging protocol to be followed by an automatic bioimage analysis workflow (**Figure 14**).

To begin with, we had to set a reproducible imaging strategy. The easiest approach would have been to acquire a representative sample of each well for the analysis. However, neurospheres do not always show a homogeneous distribution across the well. Therefore, just sampling an arbitrary number of fields-of-view most probably would lead to biased results. As an alternative, we decided to capture a 5x5 ordered grid of partially overlapping images covering the whole well surface and combine them later to get a complete reconstruction of each well. This strategy circumvents the uneven sampling problem as well as prevents the rejection of incompletely sampled neurospheres on the image edges.

To automatize the imaging step, we used the ICA-2k system but being aware of its limitations in this specific case due to the floating nature of the neurosphere culture. Grown neurospheres do not normally attach to the plastic but remain settled at the bottom of the well as a result of gravity, while keeping their 3D roughly-spherical shape. Moreover, as they display different sizes, the exact focal plane corresponding to their maximum

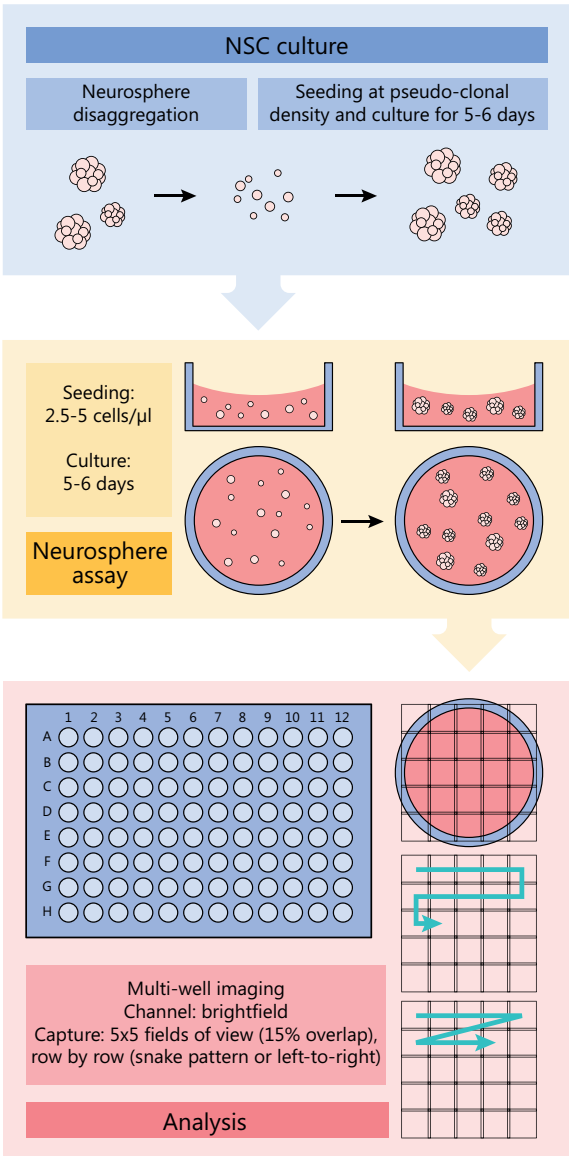

Figure 14. Schematic representation of the main steps of the experimental and imaging setup of the Neurosphere

circumference varies among clones. However, the ICA-2k high-content microscope can only acquire 2D images. As a consequence, finding an appropriate focal plane to get a focused representative image of all the neurospheres in the well is not an easy task. Indeed, laser autofocus software, typically applied to find cells adhered to the well surface, largely fails in the attempt to focus neurospheres. Therefore, our imaging protocol relies on input provided by the operator to set the best possible focal plane.

As happened in our 'adhesion assay' (see **Chapter 1**), the output of the neurosphere assay (count and size) is not based on densitometric information but instance segmentation of the image is necessary to extract per-object measurements. However, regular neurosphere cultures are not fluorescently labelled, unless for specific applications. Consequently, the system must acquire transmitted light images of living cells that are usually very low-contrasted, converting segmentation in a challenging task. With the aim to counteract these limitations, we decided to acquire high-resolution images so that texture and other image features could help to alleviate deficiencies in object detection due to the very low contrast found on some fields-of-view.

3. Bioimage analysis

We have developed a bioimage analysis workflow to analyse the pseudo-clonal neurosphere assay acquired as explained above. The workflow has been automated by means of several scripts which combine Fiji and ilastik. The ImageJ macroinstructions presented in this chapter can also be downloaded just by adding the NeuroMol Lab update site within Fiji. Requirements, installation and usage documentation, as well as an example image dataset and a series of ilastik classifiers, are to be found in GitHub (https://github.com/paucabar/neurosphere_assay).

The basic core of the workflow consists of two sequential ImageJ macroinstructions, the second of which integrates with ilastik to apply a pixel classifier trained on this bioimage analysis collection. We have also designed a third optional script that allows the quick reanalysis of the pre-generated output images in case the user is not satisfied with the obtained segmentation. This option does not require relaunching the pixel classification, since this is the most expensive step in terms of computational time. In the workflow design we have taken into account the following considerations:

- Since image acquisition has been performed by means of the high-content microscope ICA-2k, the naming convention already described (see **3.2** at **Chapter 1**) is the base of the metadata extraction.
- The macro allows the user to adjust some of the parameter sets in order to deal with the expected variability between experiments. Although all the scripts begin by popping-up their corresponding dialogue boxes, all the settings related with image segmentation are parameterized on the GUI of the second and the third (optional) macroinstruction (see **3.1**).
- Capturing the whole culturing area of a round well in a transparent plastic multi-well plate by means of a grid of square images entails two main problems with great impact on the bioimage analysis. On the one hand, pictures in the periphery of the grid will contain a portion of the well border along with an out-of-focus section of the plastic that surrounds it. Those areas outside the well boundary must be excluded from the analysis. On the other hand, there is the problem of the uneven illumination introduced by the well wall reflecting light and/or casting variable shade patterns on the captured areas. In fact, this phenomenon is so prominent that masks the typical uneven illumination that affects any image acquired using a microscope. To cope with this, the first script in the workflow serves as

a pre-processing macro aimed to correct the non-uniform illumination which is expected to be different on each field-of-view (see **3.2**).

- As already explained, the image dataset will be composed by very low-contrast pictures captured using transmitted light, since high-content imaging devices do not usually enable phase-contrast microscopy. As a consequence, neurospheres are most likely to be detected because of their texture rather than their absolute intensities. Therefore, it may be more helpful to compute several features rather than applying a filter-based approach to improve object detection. For that reason, we decided to rely on a ML strategy to facilitate the semantic segmentation of the image components. Specifically, the workflow includes a pixel classification step based on ilastik but integrated in the ImageJ macroinstruction that includes all additional image processing steps to complete the analysis. Therefore, after the preprocessing macro, all the remaining workflow steps from both ilastik (pixel classification for the generation of a probability map) and Fiji (stitching, segmentation and data extraction) are performed in a single run (see **3.3**).

- Although the illumination correction and the ilastik pixel classification are performed on the individual field-of-view images, the macroinstruction obtains a composed single image of each of the wells before undertaking the core of the analysis. In order to get a combined image that contains all the relevant information required, the script first merges in a tile the corrected brightfield image and its calculated probability maps for each field-of-view. Then, it applies a stitching algorithm included within the Fiji core that has two main requirements: i) a proper parametrisation of the tile metadata contained on the filename, so the algorithm can solve the puzzle and interpret correctly the spatial relationship between images; ii) certain degree of overlapping between tiles, so the algorithm can find the exact correspondence among fields-of-view and prevent skewed images in the fusion areas. The use of the tiles may provide additional information to improve the performance of the stitching algorithm, whereas it also ensures that the soldering process will keep a faultless alignment between channels (see **3.4**).

- The main goal of the assay is to count the number of neurospheres and to measure their size. Once stitched, segmentation is performed on the generated probability maps. Obtained by means of a supervised

ML approach, probability maps are now processed using a filter-based approach and the resulting instance segmentation is improved by means of some mathematical morphology operations. Specifically, two different probability maps are used to accomplish different aims. First, the neurospheres probability image of each well is the input to perform the instance segmentation of the clonal aggregates. However, since the training of the ML model is focused on the well content, it may happen that some pixels outside its boundaries are classified as neurospheres. However, we choose not to correct this misclassification during the classifier training, as it might be counterproductive to the actual neurosphere recognition. Conversely, the border probability is processed in order to define the area corresponding to the well culture surface and then keep only those objects within it (see **3.5**).

- Unlike previously described workflows, the script deployed for the neurosphere assay does not include a pre-analysis mode. Since the computational time required to perform the image segmentation is negligible if compared with the elapsed time of the pixel classification, we chose to save the files generated by means of this process (stitched probability maps) so that they could be reused to run a shorter workflow in case segmentation requires further optimization. To make this practical, there is an optional script which is limited to the image processing components applied after the pixel classification and the stitching steps (see **3.6**).

3.1. Parametrisation and metadata extraction

The successful output of a ML classifier is highly dependent on the training step, which requires some input from the user. However, once trained, the classifier can be applied within the workflow in a fully automated way. It is important to set the workflow to take into account some imaging parameters which will significantly influence preprocessing steps such as illumination correction and stitching. Besides, the classifier is set to generate probability maps rather than a semantic segmentation. This way, probability images can be further processed before running the final instance segmentation. A reduced number of parameters defined to perform this task are to be set by the user. For a better understanding, these tweakable parameters are indicated along the workflow explanation and are summarised on **Table 10**.

Table 10. User-adjustable parameters found in the bioimage analysis workflow for the neurosphere formation assay (pixel classification and stitching script).

Parameter	Variable type	Default
Grid	String (set from array list)	First element on the list
Tile overlap (%)	Integer (0-100)	15
Mean filter	Integer (radius)	2.0
Threshold (neurospheres)	Float (0.00-1.00)	0.35
Open	Integer (iterations)	15

Moreover, metadata extraction is a critical step to perform both illumination correction and stitching. These processes are sequentially performed within two different macroinstructions, and each one requires different spatial information which is extracted from the file name, according to the ICA-2k naming convention (see **3.2** at **Chapter 1**). Of note, contrary to previous chapters, in this workflow channel information is irrelevant and hence not recovered, since the dataset only includes brightfield images. Additionally, the illumination correction function is calculated for each field-of-view (see **3.2**), so this first macro only needs to comprehend the correspondence of the different fields among the dataset images. Finally, in order to perform the stitching, the algorithm requires: i) to identify and group every set of images belonging to the same well, and ii) to properly map them in the spatial distribution of the fields-of-view, which depends on the imaging settings provided by the user (see **3.4**).

3.2. Illumination correction

The first macro is a preprocessing script with a single purpose: to perform the shading correction of the image dataset. The parametrisation is quite simple, as it is possible to perform illumination correction by either retrospective multi-imagel or prospective methods. The retrospective workflow uses the BaSiC plugin (Peng *et al.*, 2017) to calculate the correction functions. On the contrary, the prospective workflow requires the use of reference images. Whatever the option, images will be divided by the correction functions and exported as HDF5 files using the ilastik plugin. The NeuroMol Lab update site already includes a macro to perform illumination correction. However, it would not be suitable in this case since correcting the illumination aberrations found in this assay requires a specific correction strategy (**Figure 15A**). Whereas the macro explained in the last chapter calculates correction functions computing all the dataset

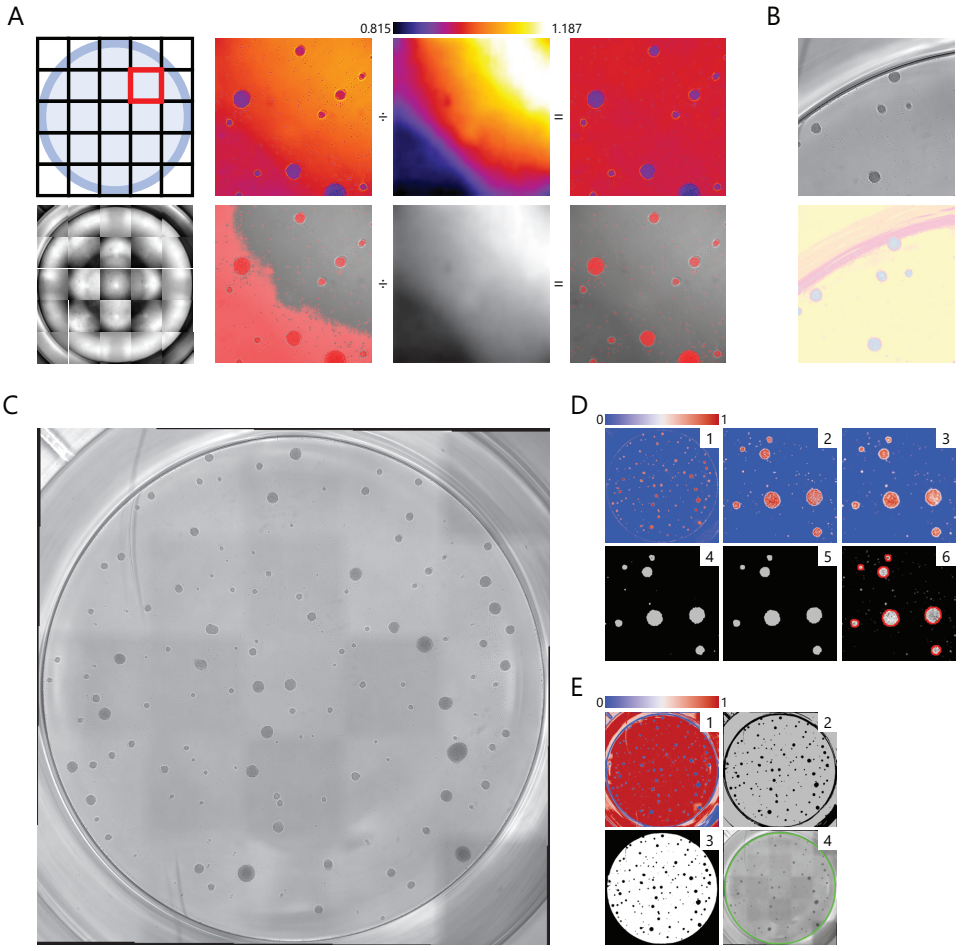

Figure 15. Bioimage analysis workflow for a pseudo-clonal neurosphere formation assay. (A) Illumination correction strategy for the neurosphere formation assay. The established imaging setup of the neurosphere assay aims to acquire whole wells by capturing a 5x5 grid of overlapping tiles which includes the well borders (top, left). As a consequence, each field-of-view presents a different pattern of uneven illumination, which greatly depends on the corresponding position with respect to the well border (bottom, left). Example of illumination correction performed on the field-of-view outlined in red. The acquired image is divided by the flat-field to obtain the corrected image. For a better visualization of the uneven illumination, images are displayed using Fiji's Fire LUT (top, right). Illumination correction can facilitate the neurospheres segmentation. On the example, illumination correction enables the segmentation (red overlay) by means of the 'Default' thresholding method within Fiji (bottom, right). **(B)** Corrected images (top) are submitted to pixel classification to obtain probability masks (bottom) pre-trained to identify three labels: background (yellow), well edge (red) and neurospheres (blue). **(C)** Whole wells are reconstructed through a stitching process. **(D)** Workflow for the segmentation of neurospheres, which is performed on the neurosphere probability map. The established probability to be classified as a neurosphere pixel is displayed using the CET-D1 LUT (1-2). Neurospheres are smoothed (3) and thresholded to obtain a binary mask (5). Then, mathematical *(continued...)*

morphology operations are applied to the mask to fill holes and remove isolated pixels (6). Segmentation overlay (red) over the neurosphere probability map. **(E)** Workflow for the segmentation of the well, , which is performed on the background probability map. The established probability to be classified as a background pixel is displayed using the CET-D1 LUT (1). The probability is smoothed (not shown) and thresholded to segment the background (2). A size filter is applied to keep just the well background (3) and its convex hull is computed (green overlay in 4).

images corresponding to the same channel, this one only computes together those fields-of-view sharing the same position in each well. The reasoning behind this approach lies in the fact that, as explained above, shading artefacts are extremely dependent on the location of the sampled area relative to the well edges. Therefore, the retrospective strategy generates 25 different correction functions for a single channel. Conversely, the prospective method asks the user for reference images, namely, images acquired using the same microscope and settings but with no sample on the foreground. However, despite the difference between methods, the correction strategy remains the same: to enhance each tile composing the well by applying a unique correction function, different from the other tiles. Therefore, prospective illumination correction also requires 25 reference images. It is also important to highlight that the use of HDF5, the preferred ilastik file type, has the advantage of being a lossless format but entails the loss of the image metadata. For this reason, the image scale is extracted and stored in a CSV file for its future retrieval.

3.3. Pixel classification

Detection is performed on the corrected images using an ilastik pixel classification workflow (Berg *et al.*, 2019). Here it is important to discriminate between two different procedures: the training of the classifier and its subsequent application on an image dataset. Training the classifier is a critical step that could be time-consuming and computationally demanding. However, as long as researchers are able to keep consistent conditions during the sample preparation and imaging protocols, the trained classifiers should be reusable and the training step skipped for future experiments. Either one way or the other, the ilastik-based classifier is an essential part of the workflow which is embedded on the second Fiji macroinstruction.

As a supervised ML approach, pixel classification requires predefined classes and user annotations. These annotations are performed on a subset of arbitrary images that would serve as a representative sample of the diversity found among the fields-of-view in the dataset. To facilitate the process, illumination in these images must be previously corrected. It is essential to generate an efficient, useful classifier since, as

explained above, the particularities of the imaging protocol used for the neurosphere assay generate great dissimilarities between different well areas (e.g., presence/absence of edges and neurospheres) and, despite the big efforts made to standardise image acquisition, all images are unlikely to be equally focused. Regarding the classes, the workflow uses three different labels: 'background', 'neurospheres' and 'well edges'. The classifier combines features provided within ilastik (intensity, edge and texture features) using filters of different sizes but, in the end, it is programmed to export the output images in the form of probability maps instead of applying a semantic segmentation. Looking for a reasonable balance between segmentation quality and computational time, we have used four different sets of features to assess the performance of the classifiers and the required computational time (see **section 4**): i) one set including all the forty default features provided by ilastik (AF40); ii) a set of 10 features selected by means of the Filter Method implemented within ilastik (FM10); iii) a set of 20 features selected by means of the Filter Method implemented within ilastik (FM20); iii) the five features established applying the Wrapper Method with a 0.5 Size Set Penalty (WM5). These classifiers can be downloaded along with an image dataset following the instructions of the aforementioned GitHub repository.

The parametrisation of the second Fiji macro is more complex, as the script contains the main part of the bioimage analysis workflow, to be performed after the illumination correction. However, regarding the pixel classification, the user just needs to set a couple of input parameters: i) the image dataset to be analysed which, like the subset of images used to train the classifier, must have been previously corrected by means of the first script; ii) the trained classifier. Because after illumination correction images are exported as HDF5 files, this workflow uses the HDF5 importer from the ilastik plugin to load those images within Fiji. The next step accomplishes the major goal of this section: to use the ilastik plugin to compute the pixel classification following the rules established on the selected trained classifier generating a probability map (**Figure 15B**) in the form of a 3-channel stack (one channel per pre-defined class) of 32-bit images normalized from 0 to 1. Since it is not required for the analysis, the background channel is next removed and substituted by the corrected brightfield image, that must be previously converted to 32-bit and normalized from 0 to 1 in order to enable the merge. This process yields a new 3-channel image that is temporarily stored as a TIF file.

3.4. Stitching

The next step is stitching the tiles, now in the form of composite images including the corrected and normalized brightfield data and probability maps, to reconstruct the

wells (**Figure 15C**). To this aim, the macro applies the Grid/Collection stitching plugin (Preibisch, Saalfeld & Tomancak, 2009), which was implemented as part of the Fiji core. Of the large set of parameters customizable within this plugin, we have selected just a few of the most critical to ask for user input. Firstly, the plugin needs to map the spatial coordinates of one image to another to register and stitch them properly. Each image filename includes a digital code that identifies its position in the originally set grid, and the macro automatically recognises the ICA-2k notation for its registration. Secondly, it is important to take into account that the ICA-2k automated system acquires the 25-fields-of-view grid row by row (or column by column) but can be programmed to do it either one by one from left to right (or up to down if acquired by column) or following a snake pattern (**Figure 14**). The user must indicate the chosen capturing method so the plugin can order properly the fields-of-view. Finally, the percentage of overlapping between tiles, as it was set on the imaging protocol, is a valuable information to perform the image registration, a critical step to compute the stitching algorithm. Once stitched, a huge composite image is obtained which is made up of three channels, each of them of an approximate size of 314 MB. The composite image is then split and channels are saved independently.

3.5. Segmentation and feature extraction

Segmentation is performed on probability maps, which are 32-bit images with a greyscale range from 0 to 1. To improve the object identification, a series of operations are performed on the neurospheres probability map image (**Figure 15B**). First, the application of a mean filter followed by thresholding for mask generation. Then, the macro fills the holes of the binary masks and applies a series of opening iterations to finally reject those objects smaller than 1,000 pixels (**Figure 15D**). As in previous workflows, some of these operations such as the mean filter radius, the thresholding values and the number of opening iterations can be adjusted by the user. Occasionally, this approach may segment particles that are placed outside the well boundaries and hence, cannot be accounted as neurospheres. To obtain a mask that only covers the well culture surface, the macro processes the edge probability map image. First, a median filter is applied to the probability map, which is then segmented using a 0.5 threshold. Finally, the smaller particles are removed and the convex hull of the remaining mask is obtained (**Figure 15E**).

At this point, the macro has generated two different masks, one containing the neurospheres and the other one defining the well surface. In order to keep only the particles inside the well, a binary reconstruction is performed using the well mask as

seed. The algorithm that performs this task is the implementation provided within the Landini's Morphology update site. However, it is also common to get ill-segmented particles in the neurosphere mask around the inner region of the edges, where shadows and other imaging artefacts may be misinterpreted by the pixel classifier despite the illumination correction. To remove these objects from the assay, the well mask is slightly eroded before proceeding to the binary reconstruction.

Once the macro has segmented and filtered the neurospheres, they are ready to be counted and measured. Nevertheless, the reconstructed images do not keep the original set scale so, in order to measure area units instead of just pixels, the original scale is set again from the previously stored CSV file.

3.6. Output, reanalysis and data curation

Finally, features are extracted and stored on a CSV file. Apart from the object count (number of neurospheres) and the area and maximum Feret diameter (neurosphere maximum diameter), shape descriptors are also calculated, which may allow users to identify ill-segmented objects, e.g., looking for outliers. Additionally, the macro saves the segmented object ROIs and the three stitched images (corrected brightfield, neurospheres probabilities and edges probabilities) as separated TIF files. On one hand, the brightfield reconstruction can be used in combination with the stored ROIs to perform a visual inspection of the segmentation output. Besides, if researchers consider it necessary, these files can also be used for data curation in Fiji or a different software.

Finally, a third separated macroinstruction allows the user to reset the segmentation parameters in order to look for a better segmentation without having to run again the pixel classification and the stitching. Since these two steps account for most of the computational time required to perform the second workflow, this third optional macro allows a rapid test of the segmentation on the already generated images.

4. Case study: comparison between the proposed classifiers for neurosphere segmentation

For the training of the classifiers and the assessment of the workflow performance we conducted a neurosphere formation assay. Previously grown neurospheres were enzymatically disaggregated using Accutase® Cell Detachment Solution to obtain individual cells. Cells were counted and seeded on flat, solid bottom, clear CELLSTAR® 96W Microplate (Sigma-Aldrich) at a cell density of 5 cells per µL (1000 cells per well)

suspended in growing medium. This type of microplates was selected because the well edges appear just as a fine line in the captured images instead of as a thick dark border obtained when using other commercial brands. Cells were grown for 4-5 DIV at 37 ºC in a 5 % CO_2 humidified incubator. Imaging was performed using the automated microscope ICA-2k acquiring only brightfield images with the 10x objective and 1x1 binning. A grid of 5x5 fields-of-view covering the whole well was set with a 15 % of overlap between contiguous pictures, and acquired on snake by rows fashion. These conditions allowed us to capture the whole well within 25 pictures. A static focal plane was set for each well to offer an overall, well-focused vision of the sample.

Randomly selected fields-of-view were annotated within ilastik for pixel classification. The same annotations were used for the different classifiers. Since we assayed four different classifiers, each based on a different number of extracted features (see **section 3.3**), we set up to compare their performance in the object segmentation. In order to do so, we ran our neurosphere workflow applying each of the four classifiers keeping constant the set of the tunable parameters (**Table 10** in **section 3.1**). Moreover, a ground truth was manually annotated by an expert on the stitched images obtained from the transmitted light (corrected) channel, which was used to generate target masks. Then, we compared the segmentation output (predicted masks) obtained through our bioimage analysis workflow applying the four classifiers with the reference annotations (target masks). To this aim, we computed the average *F1* score of all the annotated images across a range of *IoU* thresholds, starting from 0.5 up to 0.9, incrementing its value by 0.05 each round (see **Figure 16A**). Plotting this range of *F1* scores it is possible to look at both the proportion of properly selected objects and the alignment between the target and the predicted masks. This metric has been used to assess segmentation performance in previous bioimage analysis studies, for instance, for nucleus segmentation both on tissue samples (Xing, Xie & Yang, 2016) and on fluorescence images (Caicedo *et al.*, 2019a-b). For our study, we implemented a Fiji macro for the calculation of the *F1* score which is available on the NeuroMol Lab update site **[NeuroMol Lab > Assess Segmentation > Instance Segmentation]**.

All the tested classifiers performed similarly well on identifying target neurospheres, since all of them got *F1* scores greater than 0.95 in the threshold range between 0.5 and 0.65 (**Figure 16A**). From there, the score starts to slowly decay with a steep drop after 0.8. This indicates that, despite the fact that most of the neurospheres are properly identified, the alignment between the ground truth and the prediction is not perfect. Although the pattern is similar for all the classifiers, they go apart specially from 0.75 to 0.85, when the maximum divergence is observed. In this range, the best performing classifier is WM5 showing 15 points of advantage over the worst one (WM5= 0.63 vs FM10=0,47).

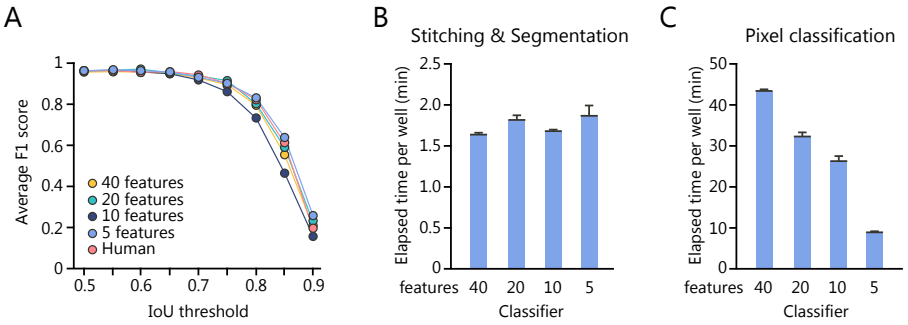

Figure 16. Evaluation of the segmentation performed by the neurosphere assay workflow by means of the identification of object-level errors. (A) F1 score plot for segmentation performance applying four different pixel classifiers (40, 20, 10 and 5 features) trained in ilastik or manually annotated by an expert (other than the one who annotated the ground truth). **(B, C)** Quantification of the computational time required by the workflow to perform stitching and segmentation (B) and pixel classification (C) when applying the different classifiers.

Therefore, in spite of the good results obtained with the four classifiers, WM5, being the classifier relying on fewer features, is the one performing better. Indeed, no major differences were observed between the *F1* score obtained by the WM5 classifier and the target mask manually generated by a second annotator when both were compared with the ground truth.

Additionally, we were interested in knowing the computational time required by each classifier, since this is the most time-consuming step in the workflow. To this aim, we added a function within the second macro to calculate the computation time elapsed to perform: i) the pixel classification and ii) the stitching plus the segmentation. We ran the script thrice using each ilastik classifier to get the average elapsed time. No big differences were observed between the elapsed time required for the stitching and the segmentation among workflows, as all of them required about 1.6-2 min per well (**Figure 16B**). However, as might be expected, the number of included features during the pixel classification had a great impact on the computation time: whereas the use of AF40 took more than 40 minutes per well, WM5 showed to be the most efficient classifier, as it performed the pixel classification of an entire well in less than 10 minutes (**Figure 16C**). Overall, we conclude that WM5 is not only the classifier which performs a better segmentation, but also the fastest one. Moreover, despite the fact that pixel classification implies a considerable increase in computational time, manual annotation typically requires twice or trice the WM5 elapsed time.

CHAPTER 4. BIOIMAGE ANALYSIS FOR THE STUDY OF (RE)MYELINATION

1. Biological background: (re)myelination and the role of the inner myelin tongue

Oligodendrocytes in the CNS wrap their specialized cytoplasmic projections around axons to form the coating structure known as myelin sheath. This peculiar discontinuous cover not only insulates axons allowing for faster conduction of nerve impulses, but also confers structural protection and provides metabolic support to the underlying neuronal projections. In the CNS, OPCs give rise to myelinating oligodendrocytes both during embryonic development leading to the process of myelination and in response to injury or in the case of demyelinating pathology during the process of remyelination **(Franklin & Ffrench-Constant, 2017)**. Due to the undeniable importance of these two processes, scientists have looked for approaches to quantify changes in myelin sheath thickness to help understand myelin biology in both physiological and pathological conditions. Indeed, there is a widespread method which has been applied for over one hundred years, thus becoming the gold standard in the field. Typically, axonal myelination/remyelination is assessed by means of the parameter known as g-ratio (*G*), defined in the field as the ratio of the axon diameter *d* to the fibre (axon + wrapped myelin sheath) diameter *D*:

$$G = \frac{d}{D}$$

According to this definition, the thicker the myelin sheath, the lower the g-ratio, which is equal to one in the absence of myelin. Diameter measurements are obtained either from light or electron microscopy (EM) images of axon cross-sections. However, section surfaces are irregular objects which, in the best case, approximate to a circle. Therefore, diameters are estimated from section areas applying a reductionist approach that assimilates them to perfect circles. Given that a circle has an area (*A)* of πr^2, where *r* is equal to the circle radius, an estimated *r* (r_{est}) can be inferred from the area formula:

$$r_{est} = \sqrt{\frac{A}{\pi}}$$

Nevertheless, being interested in obtaining an estimated diameter (d_{est}) it is more useful to directly double the previous expression:

$$d_{est} = 2\sqrt{\frac{A}{\pi}}$$

Since the g-ratio is considered a functional and structural index of optimal axonal myelination, several theoretical approaches have tried to establish an optimal g-ratio. The first one, based on the speed of the electrical conduction along the fibres, estimated an optimal g-ratio of 0.6 (Rushton, 1951). A more recent theoretical approach suggests a more optimised axonal microstructure, especially in the CNS, where axons are usually smaller and show thinner myelin membranes. Thus, the optimal g-ratio of the central fibres was amended to approximately 0.77 (Chomiak & Hu, 2009). Conversely, it has been observed that some peripheral axons have a tendency to produce lower g-ratio values than central axons (Chau *et al.*, 2000). The smaller g-ratio of the peripheral fibres could be due to a structural design less constrained by volume. Specifically, according to the second model, approximately a 40 % reduction in the space limitation restriction would be necessary to decrease the predicted g-ratio to about the 0.6 observed on some peripheral fibres (Chomiak & Hu, 2009). Regarding remyelination assessment, areas submitted to a remyelination process are typically distinguished by their thinner myelin sheaths, i.e., lower g-ratios (Blakemore, 1974; Franklin & ffrench-Constant, 2017).

During myelination, CNS axons are discontinuously ensheathed by oligodendrocytes which harbour specialized transmembrane and membrane-associated proteins that confer myelin most of its properties. In order to do so, these cells emit cytoplasmic processes which are guided to reach the axon, maintain a close contact and wrap around to form the multi-layered and concentric cellular covering referred to as myelin internodes. How the myelin sheath is formed after the leading edge of the process contacts the axon has been debated for decades (Snaidero & Simons, 2014). This leading process is known as the inner myelin tongue, also referred as inner cytoplasmic tongue (henceforth just inner tongue) (**Figure 17**). The current model relies on an array of cutting-edge imaging and sample preparation techniques such as *in vivo* live-imaging, serial block-face imaging by focused ion beam, high-pressure freezing (HPF) and freeze substitution (FS) for a better preservation of the native myelin within EM samples. This model suggests that the myelin thickening is due to the wrapping of the apical inner tongue around the axon by progressing underneath the pre-formed wrap. In addition, each myelin layer has lateral pockets rich in cytoplasm, which are extended in close contact to the axon surface towards the future node allocated on the space between sheaths (Snaidero *et al.*, 2014).

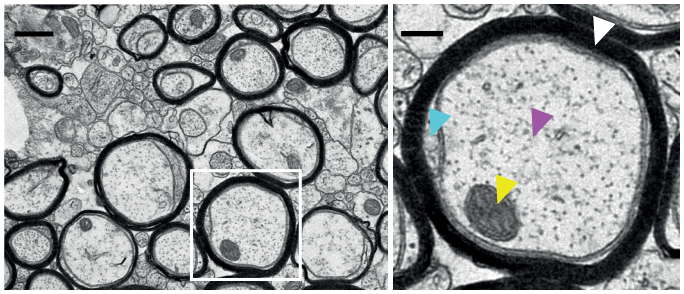

Figure 17. Axonal fibre cross-section structure. Transmission electron microscopy (TEM) image of a myelinated zone in the corpus callosum (scale bar 0.5 µm). A zoomed image (right, scale bar 0.2µm) of a myelinated axon shows its characteristic ultra-structure: the axoplasm (magenta arrowhead), often containing mitochondria (yellow arrowhead), is wrapped by the myelin sheath (white arrowhead); additionally, the inner tongue (cyan arrowhead) is the first layer of the myelin sheath that contacts the axon during myelination and remains uncompacted, as myelin compaction is carried out from the outer to the inner layer of the sheath without reaching the innermost area.

Myelin compaction is driven by the membrane-associated MBP, starting just after a few wraps. Indeed, membrane growth and myelin compaction take place in a coordinated manner occurring first in the outermost, first-formed membrane wraps to avoid the untimely compaction of the innermost growing zone. Compaction is then progressively spread inwards, always lagging behind the growing region. During myelination, the inner tongue is enlarged and is rich in F-actin. Nonetheless, as myelin matures, the tongue narrows and F-actin dwindles (Snaidero & Simons, 2014; Michalski & Kothary, 2015). Once active myelination is completed, a smaller inner tongue remains, although usually shrunken. Indeed, adult CNS fibres still preserve non-compacted cytoplasm at the ends of the myelin spiral, i.e., the inner and the outer tongues (Chang, Redmond & Chan, 2016).

Surprisingly, despite the importance of the inner tongue on the myelination process, it has been for long neglected when assessing myelination. As a matter of fact, the g-ratio disregards its existence. It may be due to diverse causes, but we could highlight two major reasons: i) it is an easily understandable and applicable method which, most decisively, has been proven to be reliable; ii) not all the imaging techniques enable the visualization of the inner tongue or they lack the sufficient detail for it to be accurately delineated. However, there are imaging techniques which empower the inner tongue acquisition, such as EM.

Due to the great popularity of the g-ratio, a considerable number of bioimage analysis tools have been deployed over the years to assess the myelin thickness or even for a more complex quantification of the tissue microstructure. Nonetheless, among these methods, just a few are publicly available. To date, a wide variety of approaches have been conducted, most of which are based on classical image processing algorithms usually implemented in semi-automated workflows that often require several post-processing steps. Among these, there are methods based on thresholding algorithms followed by mathematical morphological operations (Romero *et al.*, 2000), region growing (Zhao *et al.*, 2009; More *et al.*, 2011), watershed (Wang *et al.*, 2012; Liu *et al.*, 2012) or active contours (Bégin *et al.*, 2014; Zaimi *et al.*, 2016). Furthermore, DL methods can also be found (Zaimi *et al.*, 2018; Moiseev, Hu & Li, 2019). Some of them rely on very basic approaches just estimating axon radius and myelin thickness while others opt for more thorough analyses. ACSON, for instance, is an interesting pipeline for the 3D analysis of the axonal ultrastructure which enables the segmentation of myelin, axons (either myelinated or unmyelinated), mitochondria, vacuoles and surrounding cells (Abdollahzadeh *et al.*, 2019). Each method has its assets and caveats, being some of them really promising approaches. However, none of them implement the segmentation of the inner tongue. That pushed us to be, to the best of our knowledge, the first ones attempting this job.

The proposed analysis requires images obtained by EM which is the sole microscopy technique that allows reliable visualization of the inner tongue. In this particular case, TEM images had already been generated, following the protocol included in the Material and Methods section.

2. Bioimage analysis

Unlike other approaches aimed to enable the analysis of images acquired throughout a wide range of imaging techniques (Zaimi *et al.*, 2018), our goal is to be able to segment the inner tongue. Indeed, our approach enables the semi-automated segmentation of the three main fibre constituents: axoplasm, inner tongue and myelin, provided that the image dataset shows the inner tongue with sufficient detail. Therefore, we focused on TEM (**Figure 18A**). This can be eventually combined with the use of other advanced sample preparation techniques (Möbius *et al.*, 2010; Snaidero & Simons, 2014; Steyer, Ruhwedel & Möbius, 2019), such as HPF and FS. Although not strictly necessary, these sample preparation techniques might greatly enhance the workflow performance. Our strategy (see **Figure 18**) relies on supervised machine-learning methods implemented in ilastik to improve the segmentation and combines automated image processing with

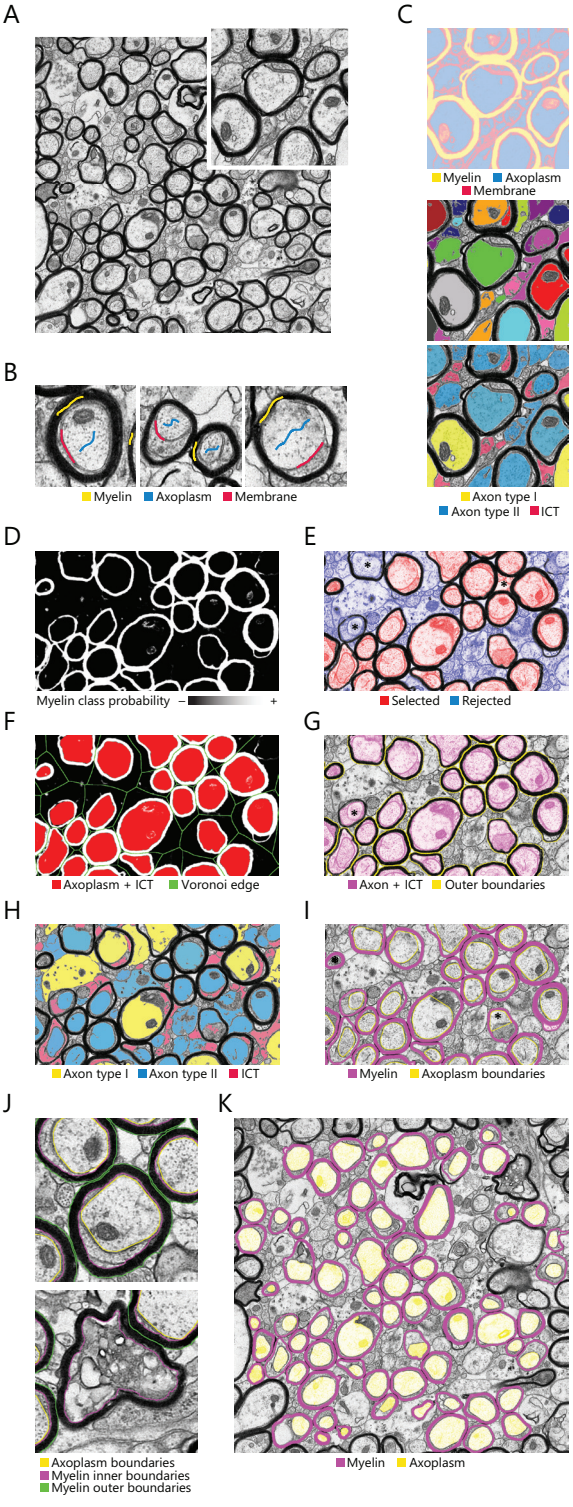

Figure 18. Semi-automated bioimage analysis workflow for the segmentation of the compacted myelin, the inner tongue and the axoplasm on fibres cross-sections. **(A)** Raw data input. **(B)** Pixel classification scores each pixel as: myelin, axoplasm or membrane. The classifier is trained drawing labels over the raw data. **(C)** The output of the pixel classification is a probabilities map (top), much easier to process than the TEM raw data. Pixels belonging to the axoplasm class are computed to obtain object instances (middle). Object classification scores each instance as axons or inner cytoplasmic tongues (ICT), though two different classes are defined for the axons according to size (bottom). Objects outside myelin will not affect the analysis since they will be eliminated later on. The classifiers can be reused for different image datasets. **(D-I)** A human-supervised workflow follows the ML steps. User-required edition (asterisk). **(D)** The myelin probabilities data are taken as input. **(E)** The myelin is processed and inverted to select potential myelinated axons (myelin inner boundary). The user can refine the selection. **(F)** Voronoi territories are defined after the selected objects in order to split the myelin. **(G)** Then the user can improve the selection of the myelin outer boundaries. **(H)** After that, the object prediction from ilastik is imported. **(I)** ICT are rejected and only axons wrapped by myelin are recovered. Users can also improve the axoplasm boundaries. **(J-K)** The macro stores the regions of interest (ROI) generated in three different sets: axoplasm, myelin inner and myelin outer boundaries. **(J)** Each axon data is measured from its three ROI (top). Axons on the image edges only generate the myelin inner boundaries, so it will be counted but not measured. Users also can reject the measurement of ill-quality axons deleting the outer myelin boundaries during the human-supervised process (bottom). **(K)** Myelin and axons overlay of the measured axons.

interactive user-edition stages. Requirements, installation and usage documentation, as well as an example image dataset and its corresponding ilastik projects, are provided in GitHub (https://github.com/paucabar/axon_aim).

Currently, our tool consists of several independent workflows to be run sequentially. Segmentation relies on both pixel and object classification based on classifiers trained in ilastik. To make the files recognizable by ilastik, if necessary, an optional ImageJ macroinstruction can be applied to pre-process the dataset before the pattern recognition step. After the ilastik workflows, the output of both classifiers is used as the input of a semi-automated segmentation workflow. Finally, an ImageJ macro script automatically corrects and integrates the previously generated data before generating the corresponding results table. In the workflow design, we have taken into account the following considerations:

- The initial steps of the workflow are performed in ilastik which, unlike Fiji, recognises a limited number of image formats. For this reason, we decided to include an optional step to convert an image dataset into a file format compatible with ilastik. Moreover, this workflow also allows to apply some basic adjustments that may be useful to make a specific dataset more similar to the one used on a previously generated ilastik classifier (see **3.1**).

- TEM acquires high resolution images, enabling the visualization of the inner tongue among many other structures. Nonetheless, the complexity of such images also makes the segmentation of its different components more difficult just by means of classical image processing algorithms. As aforementioned, in order to facilitate the segmentation of the fibres and their different compartments we apply several machine-learning methods implemented within ilastik (see **3.2**).

- After that, the ilastik output is used to perform the sequential segmentation of: i) the object defined by the inner myelin boundary (IMB), i.e., the axoplasm plus the inner tongue, ii) the whole fibre (axoplasm + inner tongue + myelin sheath) and iii) just the axoplasm without any oligodendrocyte-derived structure. Then, working with these regions, it is possible to automatically estimate the myelin thickness, the inner tongue area or the axon diameter, among many other parameters. Nonetheless, despite the usage of machine-learning methods, the complexity of the TEM datasets still makes it difficult to generate a perfect automatic segmentation. Therefore, we decided to deploy a semi-automated workflow in which the ImageJ macro automatically obtains the corresponding ROIs and then

stops, enabling the user to check the selection subset and, if required, edit the output before proceeding to the next phase (see **3.3**).

- Prior to the final measurement and construction of the results table, the macro includes several more steps intended to: i) check the manual amends introduced by the user and make sure they are meaningful, and ii) integrate the extracted objects by linking together all the identified ROIs belonging to the same fibre in order to allow a comprehensive analysis. Data correction, integration and quantification is a fully-automated process (see **3.4**).

3.1. Pre-processing

Before starting the training, our workflow includes an optional, short ImageJ script to convert the image dataset into TIF or HDF5 files. To exemplify this step, images in our GitHub available example dataset are in DM3 format, which is not recognized by ilastik. Therefore, they must be converted into an ilastik-readable format using the pre-processing macro. Additionally, the macro can also be set either to reduce the bit-depth to 8-bit or to normalize the dataset as 32-bit images.

3.2. Pixel and object classification

Machine-learning methods and, particularly, pixel classification, have been demonstrated to be a useful approach to overcome the segmentation of EM images (Kreshuk *et al.*, 2014; Kreshuk & Zhang, 2019). Therefore, the starting point of our workflow are two classifiers trained using supervised machine-learning tools implemented within ilastik. Specifically, an initial pixel classification results in a probability map that is used as input for the second classifier. Note that there is a difference between the training of the classifier, which can be skipped once successfully performed since it might be applied to similar datasets, and processing the image dataset applying a previously generated classifier, an essential stage of the workflow (see **3.3** at **Chapter 3**).

The training is performed in a small subset of images randomly selected as the training set for both pixel and object classification. It classifies pixels according to three different labels: i) compacted myelin, ii) cytoplasm, either from the fiber (axoplasm) or the oligodendrocyte (the inner tongue, regions of non-compacted myelin or the cell bodies), and iii) cell membranes, either the axolemma or the inner tongue membrane. The classifier requires user annotations and a set of features to be trained

(**Figure 18B**). In our classifier, features were automatically selected using the Wrapper Method implemented within ilastik with a 0.5 Size Set Penalty. Output images after pixel classification are exported as probability maps and, together with the raw data, constitute the input of the subsequent object classification. This second process performs an instance segmentation (i.e., extracts objects) to classify the instances. In order to do so, the cytoplasm probability map is smoothed (0.6 sigma), thresholded (0.5 threshold) and size-filtered (objects smaller than 2500 pixels are rejected because in this experimental design they cannot correspond to objects of interest). Unlike ilastik's pixel classification, where annotations are added by painting brushstrokes on the raw input images, annotation in the object classification step is carried out mouse-clicking on the segmented objects. Moreover, as a supervised machine-learning technique, it also requires pre-defined classes to train the classifier. We have defined three different classes: two different axoplasm cross-sections (larger or smaller) and inner tongue cross-sections. The rest of the objects obtained through the instance segmentation, such as cells or unmyelinated axons are not annotated during the training process, and thus their predictions ignored. Regarding the object features, for the provided training we just included all those implemented within ilastik, with the exception of the location features. Once trained, predicted objects are exported on a labelled image where background pixels are black (0), whereas foreground pixels take the value of the assigned object class: 1 and 2 for axoplasms or 3 for the inner tongues (**Figure 18C**).

Unlike the neurosphere assay workflow, ilastik classifiers are not integrated within a Fiji macro but kept as independent processes to be run separately. The reason behind this decision lies in the fact that we have developed a semi-automated workflow that will require the user intervention at some point. As shown in the previous chapter, pixel classification can be a demanding process in terms of computational time and memory use. Consequently, having the ilastik classifiers (both pixel and object classification) combined with the rest of the workflow in a single run would keep the user waiting for too long, making the supervision process much less convenient. Therefore, the classifiers must be run as a previous step before the human-supervised segmentation. Additionally, we decided to keep each classifier as an independent step, despite the fact that ilastik enables the generation of workflows combining pixel and object classification. However, this combination requires more computational time and is specially RAM-demanding, which may limit its operation in many computers. The classifiers must be run sequentially, since the object classification relies on both the raw (or pre-processed data) and the probability map generated by means of the pixel classification. Probability maps are exported as HDF5, 3-channel files, whereas object predictions are exported as labelled TIF images.

3.3. Human-supervised segmentation of the fibre cross-section

As a semi-automated tool, unlike the batch processes described in previous chapters, the workflow is limited to analyse only one image at a time. Since no parametrisation is required, the user just needs to select an image and the segmentation workflow will start after verifying that both the corresponding probability map and object prediction are available on the same folder. The workflow is divided in three stages (one per each fibre cross-section region to be independently segmented) each of them split into an automated and a user-edition sub-stages (**Figure 18D-I**).

On the stage 1, the macro starts by importing the probability map (HDF5 file) corresponding to the image to be analysed using the ilastik plugin. Then, the script works with a duplicate of the myelin probability, but with the aim to segment just the IMB (i.e., the fibre without the myelin wrap). First, a rough oversegmentation of the myelin is performed (0.2 threshold), duplicated and inverted. Then, the generated objects are split into two different images, one containing the incomplete objects touching the edges and the other one with the rest (i.e., complete objects). Afterwards, objects are filtered by circularity, being more permissive with incomplete objects (keep 0.3-1.0) than complete objects (keep 0.4-1.0), which also are submitted to a size filter (reject < 1000 pixels). Finally, all objects are combined on a single image using the Boolean OR. This selection constitutes the IMB objects automatically suggested to the user. The process stops to enable the visual inspection and, if needed, manual correction of the selection. To this aim, selected IMB objects are sent to the ROI Manager and displayed on the original raw image. Moreover, the raw data is merged in a composite image with two additional channels: the mask of the selected objects is set on the red channel, whereas the mask containing all the rejected objects (during the filtering process) is set on the blue channel. This facilitates the manual incorporation of incorrectly rejected objects, which can be selected just using the ImageJ wand tool (blue channel is automatically set to enable this function). Additionally, the user is free to apply any ImageJ selection tool to amend the selection before the script automatically saves the IMB-ROI set and proceeds to the next stage.

On the second stage, the workflow uses the IMB-ROI set to generate Voronoi territories with the aim of separating touching fibres cross-sections. Therefore, the macro employs the ROI set generated during the first stage to obtain the corresponding binary mask. Then, the Voronoi command generates an 8-bit image of the territory borders that is segmented (including 1-255 grey values, i.e., all the pixels except those with a value of 0), dilated (2 iterations) and inverted, thus obtaining the characteristic Voronoi cells. The Boolean AND is next applied between the myelin segmentation obtained

on the first stage and the Voronoi masks, so touching myelin sheaths are separated according to the IMB segmentation. After this, isolated myelin-sheath-objects are filled to obtain fibre objects and those touching the image borders are excluded. Finally, fibres are submitted to an open operation (20 iterations) in order to smooth their edges. Moreover, oversegmented prominences are pruned, and pruned ends removed. At this point, the workflow waits for the user supervision displaying the obtained fibre-ROIs on the raw data. Moreover, raw data is merged with the IMB mask, set on the magenta channel, in order to help the user to easily visualize which objects were part of the final selection during the first stage. In this case, no additional channels are added. Because the whole strategy does not require filtering there are no objects which could have been rejected by mistake, so the only automatically rejected objects are the fibres touching the borders, due to their incomplete area. Conversely, during the IMB segmentation, incomplete objects were not removed for two reasons: i) these objects are necessary to generate accurate Voronoi territories at the beginning of this stage and ii), this allows to count the number of total myelinated axons (i.e., complete and incomplete axons on the image), an additional relevant parameter when assessing remyelination. Furthermore, as in the previous stage, the user can still edit the selection before exporting the fibre-ROI set and proceeding to the last stage.

On the third stage, the macro opens the object probabilities to perform the axoplasm segmentation. Since it is a labelled image, this is easily thresholded including the axoplasm classes obtained by means of the object classification (1-2 range). Then, objects are submitted to an open operation (5 iterations) and filled before applying the Boolean operator AND in order to reject those pixels which are not covered by the IMB mask. This generated mask is still post-processed since their segmentation is initially based on the axoplasm probability map, resulting objects may sometimes appear incomplete, e.g., due to the presence of mitochondria or other organelles. Nonetheless, taking into account that axoplasms are the most convex objects of the three sets, to circumvent the problem of incomplete masks, the convex hull of the objects is computed and suggested as the axoplasm mask. After this automated process, the macro stops and asks for the user supervision for the last time, showing the suggested axoplasm-ROI set on the raw image (**Figure 18J-K**). Additionally, objects classified as inner tongues are also segmented (label 3) and submitted to a post-processing similar to the one applied to the axoplasms. The resulting masks are then merged (set on the blue channel) with the raw data. As in the first stage, this enables the addition of incorrectly rejected axoplasms just using the wand tool. Additionally, the myelin sheath mask of the complete fibre sections (those with their corresponding IMB-ROI and fibre-ROI) is set as an additional channel (magenta), so the user can easily identify a complete

fibre missing its corresponding axoplasm-ROI. Finally, the user can edit the selection before storing the axoplasm-ROI set.

3.4. Automated correction, integration and quantification of the ROI sets

Once the three ROI sets have been obtained, the last macro quantifies their corresponding areas. However, some additional steps are required before proceeding to the feature extraction. First, images lacking any of the three ROI sets are avoided, so the workflow can be applied to an entire folder even if the dataset segmentation has not been fully accomplished. Conversely, those images ready to be quantified may require a correction step to improve the quality of their ROI sets. On one hand, user-edition stages may lead to the introduction of artefacts within the different ROI sets. This last workflow automatically fixes the most typical issue that we have observed: the macro automatically removes individual or small groups of pixels isolated from the actual ROI. It usually happens as a result of a partial erase of some ROIs looking for a better accuracy, as some users may not realize of the residuary pixels when performing this kind of freehand edition. Moreover, in order to avoid unnecessary work, the lack of the axoplasm-ROI for a certain fibre cross-section is interpreted as the absence of inner tongue on the fibre (due to an almost total shrinkage), which prevents the user from having to generate two identical ROIs (since IMB and axon surfaces are exactly the same in this specific case) during the previous semi-automated workflow. Instead, an axoplasm-ROI is automatically generated as a copy of the IMB-ROI, thus completing the partial axoplasm-ROI set and circumventing any conflict regarding the IMB-axoplasm area coverage. Last but not least, the workflow codifies the ROIs in order to bound the different components belonging to the same fibre between the three ROI sets, which is a critical step to perform a meaningful quantification. In addition, codes will allow the user to trace fibres components back from the results table to the image dataset.

Since this process requires the conversion of the ROI sets into either binary masks or labelled images, once checked that an image has its corresponding ROI sets, the macro gets the raw image scale and dimensions. Then, a new black, 8-bit, scaled, equally-dimensioned image is created and the IMB-ROIs imported, so the macro iteratively generates the mask of each ROI and checks how many particles are obtained per ROI keeping only the larger one. These filtered masks are progressively added to the black image using the Boolean operator OR. Formerly, Analyze Particles plugin is used to generate the new, corrected ROIs and a labelled image, i.e., a greyscale image where background pixels are set as black (0) while the filled outlines of the analysed particles are painted with the value corresponding to the object number (1, 2, 3…). Moreover,

ROIs are renamed using a three-digit code of the object number and saved overwriting the old ones. Later on, the macro also obtains a labelled image of the fibre-ROIs. In this case it is not necessary to filter the masks, since the final fibre-ROIs will be reconstructed from IMB coordinates, thus avoiding residuary pixels. In this case, the use of labels enables the separation of fibres touching each other when working with the labelled image instead of the ROIs. Despite the fact that our image processing approach cannot generate touching masks, we decided to take this precaution because it is possible for the user to introduce touching fibre-ROIs by mistake. Regarding the axon-ROIs, just a conventional binary mask is created.

At this point, the macro has already generated a set of IMB-ROIs ready for quantification, while the fibre labelled image and the axon binary mask are just intermediate steps. The area of the IMB-ROIs is calculated, as well as the starting coordinates of the Feret's diameter. We extract these coordinates instead of the centroid ones, since, although unlikely enough in the case of the fibres cross-section, the centroid may not necessarily be located inside the object boundaries. The coordinates are used to check the corresponding pixel value within the fibre-labelled image. If the value is greater than zero, the fibre cross-section is selected by means of the wand tool. Since it is done on a labelled image, only the corresponding section is selected, even if neighbour sections are in direct contact. The wand selection is added as a ROI, renamed with the three-digit code of the corresponding IMB-ROI and its area is measured. However, if the pixel value is equal to zero the three area measurements (axoplasm, IMB and fibre) are set as NaN (not a number). This way, in the absence of an IMB-ROI, the fibre will be skipped for the analysis. Conversely, fibres with only the IMB-ROI (but not the other two corresponding sets) are included within the results table but with their area measurements stored as NaN, so the myelinated axon is counted but not measured. It allows to count ill-quality fibres (e.g., damaged during the sample preparation process) or incomplete fibres (i.e., those touching the edges of the image) without including biased size measurements.

In the end, fibres with data set as NaN are automatically skipped in the last axon correction and quantification steps. For the rest, the masks of each IMB cross-section are iteratively obtained to calculate its corresponding axon mask by means of the Boolean AND. In case more than one particle is obtained, only the larger one is measured, added as a ROI and renamed according to the corresponding IMB-ROI three-digit code. Conversely, if no mask is found, a copy of the corresponding IMB-ROI, identically sized and coded, is added as the axoplasm-ROI. As aforementioned, this is due to the fact that fibre cross-sections with no inner tongue do not need different ROIs for the IMB and the axoplasm sections. Finally, the obtained results table is set to include one row per each

identified fibre while columns store both metadata (image filename and fibre code) and the area of the three components: axoplasm, IMB and fibre.

3. Case study: evaluation of the fibre, inner myelin boundary and axoplasm segmentation on an experimental dataset

In order to quantitatively assess the performance of the workflow, we compared the segmentation output obtained using the macro described in this chapter with a ground truth manually annotated by an expert. This was performed on TEM images different from those used to train the classifiers. TEM *in vivo* images were obtained from CC remyelinating areas previously submitted to a demyelination lesion by the injection of the toxin LPC. As already mentioned, one critical point in our design are the user-supervised steps intended to correct the automatic segmentation. Therefore, to evaluate the impact of such manual steps, we compared the expert's fully manual ground truth with to different workflow outputs: i) one completely automated, without any user intervention and, ii) one semi-automated including all the user supervised steps but just allowing either to delete ROIs or to add new ones using the wand tool to select the instances automatically suggested by the Fiji macro, avoiding the usage of the freehand selection tool for the ROI edition. To make it comparable, the expert annotations avoided axons touching the image edges, since the script only extracts quantitative measurements from complete axons. Additionally, the sample preparation process for TEM imaging can affect the integrity of some axons, e.g., causing the deformation of the fibre or damaging its structure to an extent which precludes the recognition of its components. As artefacts, these fibres were not annotated either.

Regarding the experimental datasets, both automated and semi-automated predictions were processed in the same manner after the corresponding segmentation strategy. However, since discarding of the border-touching objects is performed later on the workflow, in order to make the predictions comparable just after the segmentation step, edge-touching ROIs were deleted using the function described for the StarDist workflow (see **section 2.3** on **Chapter 2**). This function is also provided as an independent macro within the NeuroMol Lab site **[NeuroMol Lab > other macros > roi exclude edges]**. Finally, the resulting sets were submitted to the automated correction provided on the last script of our tool (see **section 3.4**). The metric used to assess the performance of our method was the *F1* score. Evaluation was performed by means of the macro described in the Materials and Methods section. The average *F1* score of all the annotated images was calculated across a range of IoU thresholds, starting from 0.5 up to 0.9 (increasing by 0.05). Scores were computed for fibre, IMB and axoplasm

instances independently.

As shown in **Figure 19**, the automated approach demonstrated a considerable capability to predict the fibre constituents, being the fibre the object that the method seems to identify the better. Moreover, as might be expected, these results can be significantly improved by allowing the user to revise and amend the segmented objects, even with the limitation of not allowing to draw ROIs with the freehand tool. This enhancement is most noticeable in the fibre segmentation, with an average *F1 score* improvement close to 0.06 among the different IoU thresholds, with its maximum (0.09) when a 0.9 IoU threshold is set. The axoplasm has been confirmed to be the most difficult element to be segmented and the less prone to be enhanced without a greater user intervention (limiting the use of freehand selection tools). This makes sense since, as the last segmented objects, the axoplasm set is affected by the errors accumulated during the first two stages, which determine what is and what is not an

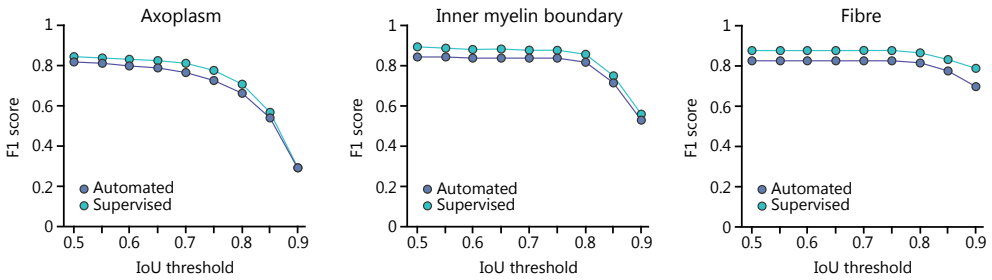

Figure 19. Evaluation of the fibre components (axoplasm, inner myelin boundary and fibre) segmentation performed either in a fully automated or a supervised, machine-aided way. The assessment is performed calculating the object-level metric known as F1 score, which is plotted for increasing IoU thresholds for the estimation of shape-matching accuracy in both the automated and the supervised results.

axon. Additionally, the axoplasm segmentation faces other issues such as the axolemma thinness, which occasionally precludes its detection, and the presence of electron-dense bodies within the axoplasm, such as mitochondria or neurofilaments. Regardless, good-quality axoplasms are nicely segmented in general, which highlights the importance of the sample preparation for the workflow output. Finally, as a semi-automated method, ill-segmented objects can be improved on-the-fly benefiting the segmentation of subsequent stages. Indeed, this semi-automated approach has demonstrated to be much more efficient than the fully-manual strategy previously applied. Semi-automation reduces considerably the time dedicated to manual annotation, thus enabling the analysis of a greater number of fibres. As a matter of fact, before the implementation of

our semi-automated tool, manual annotation was restricted to half of each TEM image surface in order to make the analysis feasible, whereas now the annotation process is much faster even analysing whole images.

Discussion

C: 0
M:96
Y:57
K: 0

R:231
G: 24
B: 74

The bioimaging field has quickly evolved during the last years with the implementation of hardware and software for greater automation at the different stages that compose a microscopy-based experiment. The topmost representatives of these forefront methodologies are those combining high-content imaging with automated bioimage analysis protocols, although there is a whole spectrum of intermediate levels of throughput up to the manual analysis that is still practiced in many fields. Therefore, a big effort is still to be made in order to spread the use of cutting-edge imaging technologies throughout the life science fields relying on image-based experiments.

In this thesis, we have aimed to generate bioimage analysis workflows, in some cases including the development and optimization of the experimental and imaging setups, for the study of brain-specific processes in the field of regeneration. On one hand, we hypothesised that it would be possible to adopt microscopy-based screenings combined with automated bioimage analysis for the in vitro study of the subependymal NSCs with an emphasis in well-conducted pre-processing steps, which have involved the adoption of different illumination correction strategies or the search for more optimised protocols to generate rules for the detection of fields-of-view affected by blur. In the present work we show that automated bioimage analysis protocols developed for the study of cultured NSCs improve the throughput and the reproducibility of the in vitro assays of different kinds and analytical complexity.

On the other hand, we looked at the possibility to semi-automate the TEM analysis of in vivo experiments for the assessment of remyelination. We also show that the combination of supervised ML with semi-automated segmentation of fibre cross-sections on TEM images contributes to enhance the analysis throughput of experiments aimed to quantify classic metrics just as the g-ratio, whereas it also empowers the inclusion of novel metrics by including inner-tongue-based features to assess new parameters.

The study of the NSC biology, despite reaching its greatest level of complexity when performed in vivo, heavily relies on in vitro practices that allow much easier and versatile decomposition and manipulation of the system variables. As a matter of fact, the emerging field of postnatal mammalian neurogenesis in the eighties leapt forward thanks to the establishment of in vitro conditions to selectively culture and expand primary neurospheres from adult brain neurogenic niches, which demonstrated the existence of adult stem cells in the organ (Reynolds & Weiss, 1992). Since then, a series of assays have been developed to address numerous hypotheses that may sometimes be difficult to confirm just conducting in vivo experiments. Among these in vitro assays, the most extensively used are aimed to assess the inherent properties of the stem cells,

i.e. self-renewal and multipotency. However, the versatility of the in vitro techniques enables the development of additional assays to address other aspects of the NSC biology such as proliferation rate, transcriptional profile, metabolism, intracellular signalling or adhesion, among many others. Despite the convenience of these assays, the value and potential of the neurosphere cultures is not devoid of detractors. In fact, there are several limitations of the in vitro NSC cultures that cannot be overlooked: the lack of surrounding niche elements and signals, the fact that there is no easy direct correlation between neurosphere cells and the SEZ cell types found in vivo, the assumed heterogeneity of the culture which is supposed to contain both NSCs and progenitors along with more committed progeny, or the limited number of passages that NSCs can be maintained before starting to be unreliable due to excessive adaptation to the culture conditions and/or telomere shortening (Jensen & Parmar, 2006; Ferrón *et al.*, 2009; Belenguer *et al.*, 2016). Nonetheless, the field has experienced exciting advances during the past few years. For example, our lab has recently identified diverse populations with distinct proliferative dynamics in neurosphere cultures, suggesting that NSCs in different states of activation might be found in the culture. We have shown that slow-proliferating cells with a molecular profile compatible with in vivo primed-NSCs coexist with activated NSCs with a higher proliferative rate in in vitro cultures (Belenguer *et al*, 2020). This observation opens a new road for the study of this interesting and unexplored NSC state. Another exciting in vitro approach which may contribute to a better understanding of the NSC properties is the deployment of protocols for the maintenance of the cultured cells in a quiescence-like state (Martynoga *et al*, 2013). Most of these advancements have been possible thanks to the adoption of FACS-based protocols, which along with the classical in vitro assays, have become an essential tool for the field. In this context, we considered that the development of high-content screening protocols based on some of the most common NSC in vitro assays could provide powerful tools to address these new challenges. Additionally, by applying high-content imaging and automated bioimage analysis strategies for the study of NSCs in vitro cultures, not only we can increase the throughput of such assays but also eliminate the user-introduced bias during the analysis. Finally, in the present thesis, we have introduced several experimental and imaging setups that would allow better standardisation. Hence, we have been able to apply our tools in experimental case studies obtaining reliable results. Thus, in our opinion, fostering the adoption of microscopy-based screening methods has the potential to become a new boost on the field by, e.g., enabling quantitative analysis of image-based protocols previously unquantifiable or the possibility to assess multiple experimental conditions at the same time, among other advantages.

Mechanistic studies of remyelination mostly rely on well established in vivo models of chemical-induced demyelination. These methods enable the assessment of remyelination without the confounding variable of the concomitant demyelination process typically occurring in pathological scenarios. For the analysis of these experiments, it is necessary to extract quantitative data about the newly-formed myelin sheaths after the recruitment of OPCs. The gold standard for quantifying myelin, the g-ratio index, is extensively used in remyelination research, among other fields studying the properties of the white matter. It is used as an approximation to the thickness of the myelin ensheathment and is typically measured in fibres cross-sections in images acquired by diverse microscopy techniques. However, in spite of its well-proven usefulness, the method is limited by the necessity to assimilate fibre cross-sections to a perfect circle. This has led researchers to look for complementary metrics with the aim to better describe the reality of the complex morphology of axonal fibres. Some examples of companion parameters are the myelin thickness, the fibre cross-section area or the diameter of the fibre and the axon (Giacci *et al.*, 2018; Ferrari Bardile *et al.*, 2019). Most of these metrics can be extracted from the same annotations which are required for the calculation of the g-ratio. Notwithstanding, the g-ratio approach neglects a key player in the (re)myelination process, the inner tongue. Indeed, the assessment of metrics related with the inner tongue is gaining popularity and some new parameters have been proposed, such as a modification of the classical g-ratio consisting in the subtraction of the inner tongue area from the total fibre area for the calculation of the fibre diameter (Meschkat *et al.*, 2020). Thus, a corrected fibre diameter (D_{corr}) is first calculated after the quantification of the compact myelin area (A_{my}), the non-compact myelin, i.e., the inner tongue area (A_{it}) and the axoplasm area (A_{ax}):

$$D_{corr} = 2\sqrt{\frac{(A_{my} - A_{it} + A_{ax})}{\pi}}$$

Therefore, the corrected g-ratio (G_{corr}) is a ratio of the axoplasm diameter (d) to the D_{corr}:

$$G_{corr} = \frac{d}{D_{corr}}$$

In this case the additional annotation of the inner tongue is required for the analysis. Therefore, we considered that a tool for the assistance during the annotation of the myelin sheath, the inner tongue and the axoplasm on fibre cross-sections could be helpful to overcome the bioimage analysis bottleneck. Indeed, our user-supervised approach increases the throughput of the assay and enables the quantification of the

classic g-ratio along with many other complementary metrics. The use of multiple metrics has the potential to enable the characterisation of diverse phenotypes that could not be appreciated quantifying a single, even if meaningful, parameter. For example, this may enable the application of gating strategies or ML methods for the classification of fibres. Moreover, the development of novel DL methods highly depends on the generation of richly-annotated datasets, which is a tedious and time consuming task. Thus, the existence of user-friendly tools for the annotation of ground truths may also benefit the field.

Furthermore, although we focused on the in vivo models, it is also possible to isolate and culture OPCs for the study of their properties (Chen *et al.*, 2007; Medina-Rodríguez *et al.*, 2013). In the context of my stay at the MRC Centre for Regenerative Medicine I had the opportunity to work on a bioimage analysis pipeline for the quantification of cell phenotypes on OPC cultures (https://github.com/paucabar/oligodendrocyte_differentiation) that we have not included in the Results section. Although we did not attempt the adoption of high-content imaging methods for these assays, our experience suggests that it could be an interesting approach. However, OPC cultures present some limitations compared with neurosphere cultures, being the major one that often subtle cellular changes lead to phenotypic drift over the passages (Lin *et al.*, 2006).

Setting up a high-content screening assay: the neverending story?

As already mentioned, the proper optimisation of the experimental conditions and imaging protocols has a profound beneficial impact on the development of the analysis workflow. In fact, the positive influence can be bidirectional if both the experimental setup and the analysis strategy are developed in parallel (Boutros, Heigwer & Laufer, 2015). As a matter of fact, there are many factors in the experimental and imaging setup that can be improved to facilitate the segmentation of the desired objects, such as the establishment of the staining procedures, the magnification, exposure time or binning during the capture or even not so obvious variables such as the chosen labware or the experimental strategy itself. For example, the images that we initially obtained in the neurosphere assay by seeding the NSCs in the culture multiwell plates that we regularly used in the lab at that moment, displayed a prominent dark ring in the periphery of each well caused by an aberration introduced by the plastic wall. This simple fact turned into an irresolvable bioimage analysis issue as, despite the application of several restoration operations, it prevented the segmentation of the neurospheres in the well border. Curiously, a simple change of brand solved one of the main obstacles of the analysis.

Otherwise, the first adhesion assays were performed allowing sufficient time for the NSCs to attach the monolayer and express their morphological phenotype before labelling by means of nestin immunostaining, since activated NSCs express the EGF receptor and nestin **(Codega *et al*, 2014; Mich *et al*, 2014; Chaker, Codega & Doetsch, 2016)**. However, this approach made it difficult to individualise attached cells in close proximity, which implied a much complex parametrisation for the bioimage analysis. Therefore, we decided to shorten the time that NSCs are let to attach after seeding, proceeding immediately to the washing and fixation steps. Additionally, we substituted the immunostaining step by the previous loading of cells with a cell tracker, a procedure that increases the throughput of the assay and avoids the extensive washing during the immunocytochemistry protocol, which can lead to the damage of the monolayers and/or the detachment of some adhered NSCs. One particular choice with great impact on the analysis strategy design is how the monolayer cells are detected. In order to obtain cleaner images and to avoid interferences with the detection of the adhered NSCs and the need of extra repetitive washing steps, we decided to perform a simple nuclear counterstain. This way, the number of cells in the monolayer could be easily counted, but the image area corresponding to their cytoplasms had to be estimated through image processing operations. We are aware that this may lead, in some cases, to a certain deviation between the real and the calculated monolayer area. Other experimental approaches could have been used to visualise the cytoplasm such as staining of F-actin with fluorescent phalloidin or any other general staining **(Chambers *et al.*, 2018)** or using ML for the segmentation of transmitted light images. However this would have implied additional sample manipulation steps or the acquisition of images difficult to segment. Taking into account that we visually check the confluence and integrity of the monolayer at the beginning of the assay, discarding those wells with underconfluent or severed monolayers, we believe that our method simplifies the analysis strategy without compromising the accuracy of the obtained results.

Another critical step, closely related to the analysis strategy itself, that requires adequate optimisation is image acquisition. For example, regarding the neurosphere assay, being able to acquire whole wells on a single field-of-view could have great advantages. On the one hand, a single laser autofocus plane for the whole well would reduce the variability often found among images. On the other hand, the stitching step on the bioimage analysis workflow would no longer be necessary. This would require the use of 2x objective, currently not available in our ICA-2k configuration. In any case, although it would greatly benefit the imaging and the initial image processing, it might introduce an additional problem since the sampling resolution at 2x might not be enough to the accurate measurement of the smaller neurospheres.

The nature and characteristics of the biological sample itself can neither be disregarded, not only for the imaging setup but also when it comes to designing the analysis strategy. Cell biology approaches are moving fast towards the implementation of 3D cultures, such as spheroids, organoids or mini-organs, in which cells are cultured in multicellular, three-dimensional structures, imitating the architecture of the parental tissue more accurately than is possible in 2D models (Kapałczyńska *et al.*, 2018). This poses significant challenges for imaging and analysing cell culture data. Neurospheres are 3D aggregates that grow in suspension, so the neurosphere cultures also have the potential to be imaged applying optical sectioning methods for a greater comprehension of the cell populations which conform a clone and coexist in the spheroid. These approaches are still uncommon in the NSC field, but have been performed (Malik *et al.*, 2015). However, in our case, we set to acquire 2D images in spite of the fact that neurospheres are 3D floating structures and decided to give continuity to the typical surface measurements extracted from these assays. Neurosphere formation assays have been traditionally analysed either counting neurospheres under the microscope or manually annotating the clones estimated major cross-sections (assimilated to the neurosphere diameter) on images acquired through a non-automated phase-contrast microscope. Naturally, it would be arguable that this 3D-to-2D assimilation introduces an excessive bias in the obtained measurements and that the adoption of methods for the 3D analysis of neurospheres would be much more adequate. In fact, using a fixed focal plane to capture brightfield flat images of an heterogeneous mixture of 3D spheroids of variable size, certainly leads to certain inaccuracies such as out-of-focus clones, excessive contribution of the light diffraction creating halos around the neurospheres or the presence of a drop shadow effect cast by the clones themselves. However, it is important to keep in mind the biological context of the measurement, since the precise and absolute quantification of the neurosphere size might not be really necessary. It has been reported that neurospheres greater than 100 µm are more self-renewing and capable of long-term expansion (Louis *et al.*, 2008) and this type of quantification is usually presented as the percentage of clones in size ranges (< 50 µm, 50-100 µm, > 100 µm) compared among genotypes or between control and experimental conditions. Therefore, the small percentage of variation between the real and the estimated neurosphere size would have a minor impact on the percentage of neurospheres in each size category and, in any case, would affect similarly all the compared conditions.

Illumination correction: a necessary but tricky operation

The introduction of a pre-processing illumination correction step is almost compulsory when it comes to the quantitative analysis of images acquired through a microscope. Since in this thesis we were mainly focused in the deployment of bioimage analysis tools for high-content screenings we have only applied the most common correction strategy for such experiments, the retrospective multi-image method, which takes advantage of the large experimental datasets to calculate a single correction function per channel and plate. However, as we have seen in the case of the neurosphere assay, it may be necessary to calculate different flat-field images per field-of-view This requirement becomes a drawback, since the method relies on the computation of a large number of images, and this limits the groups to a single image per well. In our case, however, we have experienced that the BaSiC algorithm is capable of generating valid flat-fields even with a low number of images (i.e., 40). Alternatively, if the number of acquired images precludes the application of retrospective multi-image methods, it might be still possible to rely on single-image methods. In fact, the use of retrospective single-image methods is a popular approach, as most of the bioimage analysis collections include tools for the estimation of individual flat-fields by performing operations limited to assess single images. This is also an interesting approach if every image on the datasets presents different illumination patterns, which prevents the use of multi-image methods.

Independently of the applied method, it is advisable to test the performance of the calculated flat-fields and not simply apply them and run the analysis blindly. Neglecting this may instead lead us to spoil the experimental dataset. For the sake of the assay throughput, it is convenient to establish well-defined criteria which can be easily addressed. For example, the visual inspection of the obtained flat-fields may be very informative. The ideal illumination correction function can be pictured as an image where the illumination peak falls in the central point (centre of the optical axis) while fading as moving away from the centre. Alternatively, it may appear as a directed (horizontally, vertically…) intensity ramp. Obtaining a pattern that diverges from these expected ones, unless justified by the specific features of the image dataset, might be suggestive of an inappropriate performance of the illumination correction method. However, even if the flat-field images 'look fine', it does not necessarily mean that they can be trusted. Indeed, over- and under-correction are issues derived from the performance of an ill-calculated flat-field, which can add error to quantitative intensity measurements. A common approach to test this is to generate plot intensity profiles of the acquired and corrected images looking for a relatively flat distribution of the intensity baseline (Jost

& Waters, 2019). Since imaged objects introduce variations on the intensity profile, in this thesis, we have checked images without cells on the foreground. A more efficient approach could be to deliberately acquire this kind of images (e.g., in wells where no cells were grown) to test the flat-field performance.

Implementation of internal quality controls: the road to full automation

The upswing of automated microscopy and bioimage analysis has led to a notorious advance in the bioimaging field. Nonetheless, there is still a long road ahead before fully automated tools can be broadly accepted by life scientists, especially with the great deal of trust generally invested on visual inspection. In fact, it is not uncommon to find bioimage analysis users who feel uncomfortable when applying automated workflows and even re-analyse the image dataset manually in order to compare the results. The fact is that, however convenient, automated tools are far from flawless so a certain amount of prudence when interpreting the results generated through fully automated protocols is more than advisable. For example, though quite optimised, autofocus methods may eventually fail causing the acquisition of blurred images. In addition, the blind acquisition of large datasets prevents the detection of issues derived from the sample preparation, such as saturated debris. Most likely, these ill-quality images will remain unnoticed among a set of mainly well captured images and, if not excluded from the analysis, they can impair the results of the assay, as stated by the GIGO concept. As a side note, apart from these drawbacks, non-human intervention also has its advantages apart from the automation itself, primarily the unbiased acquisition of imaging data that, in the end, is the raw data which should answer our biological question. Seen this way, and if we take into account that there are methods to quantify the quality of the images but not the degree of bias introduced during their capture, it seems that we should care more about the latest.

With all this in mind, the necessity of including adequate quality controls properly distributed along the automated workflow steps becomes evident. One common strategy consists of the extraction of diverse metrics aimed to quantify different image quality issues. Indeed, the most common metrics have been designed to quantify the blurring and the presence of saturated artefacts, both included in the workflows incorporating quality control checks in this thesis. As we have observed, while saturation may be easily quantified, the identification of out-of-focus images might be more complex and many different metrics have been proposed for this purpose (Caicedo *et al.*, 2017). During the set up of the cell proliferation and apoptosis assay, we decided to investigate which

metrics would perform better in our cell-based assays using supervised ML for the identification of quality control rules. The most relevant among the tested metrics was found to be the log-log slope of the power spectrum of pixel intensities, which has been also reported to be the most effective metric in other high-content screening assays (Bray et al., 2012). However, a limitation of these metrics is that it is often necessary to readjust the rules for each experimental dataset. Thus, it may be required to train a classifier every time that an experiment is performed. While this could be overcome relatively quickly if there were a similar proportion of in-focus and blurred images, actually the probability to fetch blurred fields-of-view is quite low if the acquisition of the dataset was properly set up. Therefore, to annotate enough images to train and assess the classifier is time consuming and it may even become an impossible task. This can be eased by looking for outliers plotting different metrics, e.g., in CellProfiler Analyst. Instead, we decided to try a different approach based on the capture of additional out-of-focus images to balance the proportion of the different classes, which highly enhanced the training throughput.

In spite of the importance of quality control, there is a fully automated bioimage analysis workflow in the present thesis which does not include any quality checkpoint. It is the case of the neurosphere formation assay. On the one hand, many of the mentioned metrics would be useless on the transmitted light images. On the other hand, since our imaging setup includes the manual setting of the focal plane for each well no major acquisition issues are expected to happen. Moreover, since the output of the bioimage analysis workflow includes the stitched well, it is relatively easy to quickly check for any imaging or stitching issue across the dataset, as issues are quite evident. In any case, in future updates of this tool, it would be advisable to include a preview mode to let the user check the result of the illumination correction and the output of segmentation before running the whole analysis. This would be particularly useful to evaluate the re-usability of pre-trained classifiers. Conversely, the cell adhesion workflow includes customised quality control metrics apart from some of the most typically used. We decided to implement these metrics due to the importance of the feeder monolayer for the assay, since a damaged or non-confluent monolayer spoils the results already at the experimental stage. These metrics have been proven helpful for the rejection of incomplete monolayers from the analysis.

Some considerations on cell phenotype quantification

The development of methods for the segmentation of overlapping nuclei on 2D images, such as StarDist or the multilayer gas of near-circles (MLGOC) model (Molnar,

Kato & Jermyn, 2012), represents a big advantage for counting clumped cells and for a more accurate determination of their nuclear morphologies. The latest can be of paramount importance for the identification of some phenotypic behaviour on cell populations, questions typically addressed on high-content screening assays or tissue scanning. Thus, we aimed to implement a workflow including the option to apply these methods on our NSC in vitro cultures, so the proliferation and apoptosis workflow can be set to apply the StarDist built-in Versatile (fluorescent nuclei) model. In our experience, this generalist DL model performs an accurate segmentation on our cell-based high-content screening assays, for which we adapted an specific imaging setup. Additionally, by adding an alternative filter-based workflow we aim to ensure that any assay can be analysed, even if the generalist approach fails, whatever the reason.

When it comes to extract densitometric information there are some considerations to make which are typically neglected when analysing binary, non-overlapping masks. This is related to a property of images acquired through conventional widefield microscopes: the intensity values determined by the microscope sensors are proportional to the concentration of fluorescent particles on the sample. Hence, we can assume that, using low NA objectives, the intensities from superposed nuclei are additive. Therefore, if the intensity values of regions where cells overlap is approximately the sum of each individual cell intensities, the intensity contribution of two cells growing on top of each other doubles that of a single cell (assuming that both cells contain the same concentration of fluorescent molecules and a similar thickness on the superposed regions). Indeed, MLGOC was extended incorporating a new data term capturing this property, thus increasing the performance of their segmentation model (Molnar *et al*, 2016). Since we were not looking for subtle phenotypes, for our cell proliferation and apoptosis workflow we chose to extract the densitometric data from whole segmented ROIs, without applying any correction or rejecting overlapping regions. In spite of carrying this error, this approach allowed us to identify the different proliferative behaviours and the detection of apoptosis events applying clustering methods. Nonetheless, if other users do not desire to deal with such issues, we consider the possibility of adding the alternative option of obtaining a labelled image instead of an ROI set as segmentation output. These type of images keep the label of the most probable nucleus on the top of other overlapping instances. While this affects the morphological features of the erased nuclei, this approach may limit the error in the extraction of densitometric features. Maybe an interesting strategy could be to combine both overlapping and non-overlapping instances to get the better metrics fitted for each approach. Labelled images can be easily analysed within Fiji, e.g., by adding the MorphoLibJ update site (Legland, Arganda-Carreras & Andrey, 2016).

Our workflow was intended to serve as a tool for the quantification of cell proliferation and apoptosis on high-content imaging assays of in vitro NSC cultures. However, beyond our initial goal, this workflow has also the potential to be used for the quantification of up to four nuclear markers, thus enabling the identification of different phenotypes by combining the densitometric analysis of nuclear and/or ubiquitous molecules and the morphological features of the nuclei. The workflow, however, does not include the possibility to segment cytoplasms or cytoplasmic rings. To this aim, we have deployed a dedicated CellProfiler pipeline (https://github.com/paucabar/stsm_i3s) which enables the segmentation of nuclei, cells and cytoplasms (see **Figure 2**) either for the identification of cell phenotypes or for the localization of labelled proteins which can translocate between subcellular compartments, a useful approach for the quantification of cellular processes such as cell proliferation (Spencer *et al*, 2013). Along with this pipeline, initially built during a Short Term Scientific Mission in the BioScreening Platform at the Instituto de Investigação e Inovação em Saúde (Universidade do Porto), we include a companion pipeline for the computation of illumination correction functions using a retrospective multi-image approach within CellProfiler. Additionally, the pipeline is set to be combined with an ilastik pixel classification for the segmentation of cells without using any additional staining. The decision to use CellProfier for the segmentation of different cell compartments is based on the fact that it is a bioimage analysis collection specifically developed for the quantification of cell phenotypes, which enormously facilitates the instance segmentation of cells and subcellular compartments. Unfortunately, CellProfiler does not implement yet the possibility to apply DL models to overcome such tasks, as currently is eminently based on a filtering approach. Therefore, it is not possible to benefit from generalistic approaches such as StarDist. In this sense, a novel promising strategy for cell phenotyping is the combination of StarDist and Cellpose (Stringer *et al*, 2021), a generalistic DL method for cellular segmentation.

Metrics for the automatic evaluation of segmentation: a way of quantitatively assess if the computer 'sees' what we see

The assessment of the segmentation performance has been generally approached using metrics which look for differences between the segmented or predicted mask and a reference or ground truth mask, generated either manually annotating the target objects or using state-of-the-art segmentation methods. For our performance evaluation we decided to use a metric aimed to identify object-level errors. Therefore, in spite of the fact that both evaluated methods (**Chapters 3 and 4**) apply pixel classification which allocates pixels to different classes (semantic segmentation) but does not actually

identify objects on images, we were interested in the assessment of the final output of the workflow (instance segmentation) rather than the pixel classification performance. As a side note, although we did not assess semantic segmentation on the present thesis, the NeuroMol Lab update site includes a macro for the computation of the most common metric used for this aim, the IoU, also known as Jaccard index (Van Valen *et al.*, 2016). Other methods focused on evaluating pixel-wise segmentation accuracy are the root-mean-square deviation (Gudla *et al.*, 2008) or the bivariate similarity index (Dima *et al.*, 2011). However, these methods fail to quantify object-level errors.

We decided to implement the F1 score metric within the NeuroMol update site, as it is a widely used performance metric based on the IoU, though computed per object, thus enabling the quantification of errors at the object level looking at the overlap degree between the predicted and the target masks (Caicedo *et al.*, 2019a-b). We have applied this metric to assess the instance segmentation of different components from fibre cross-sections and neurospheres cross-sections. In the case of the fibre segmentation, we were interested in addressing the object segmentation accuracy that our workflow can reach without human supervision or limiting the human intervention to improvements suggested by the macroinstruction. According to the F1 score, the step which requires a greater intervention is the axoplasm annotation. Naturally, the thin membrane which separates the axon from the inner tongue may be more difficult to estimate than the electron-dense myelin sheath. This often depends on the sample quality, as TEM sample preparation is prone to introduce artefacts which may complicate the segmentation. In our experience, though not devoid of error, this strategy helps to overcome the bioimage analysis bottleneck caused by the manual annotation of the TEM images. Regarding the neurosphere formation assay, according to the F1 metric, the workflow developed in the present work was able to obtain a score comparable with the performance of a human annotator. If we consider that the method consists in a fully automated bioimage analysis workflow, this allows us to improve the throughput of the assay on a great extent while extracting comparable quantitative data.

Current challenges for the bioimage analysis community

The blooming of quantitative and computational bioimaging has led to the creation of new structures for networking and for providing support to the bioimage analysis community, such as NEUBIAS in Europe or COBA (Center for Open Bioimage Analysis) in the United States, and dedicated publication platforms, e.g., the most recent open access journals Biological Imaging or Frontiers in Methods and Tools for Bioimage

Analysis. Such is the impact of this growing field that a new profession has arisen to join other bioimaging specialists (i.e., life scientists, microscopists and developers). The main role of the so called bioimage analysts is to bridge the gap between developers and life scientists by providing practical bioimage analysis workflows based on components built by developers. To a large degree, all the objectives of the present thesis were related to this notion. Specifically, one of our main goals was to increase the throughput of the proposed assays to alleviate the bottleneck that the analysis of image-based experiments often involves. This is not a minor issue according to an inquiry conducted by NEUBIAS, which surveyed almost 2,000 researchers (mainly life scientists) in 2015. They concluded that the investments in European bioimaging infrastructures are not well balanced, since most of these platforms do not have the capacity to analyse all the produced image data. It is possible to extract some important hints to improve the current situation from the researchers' answers: 68 % agreed that there is a lack of training to overcome the bioimage analysis hurdle; indeed, 60 % stated that bioimage analysis is the more difficult step on projects relying on bioimaging. Moreover, approximately 58 % of the bioimaging acquired data is never quantitatively analysed. The survey has been recently launched for a second time, so maybe soon we will know the impact of the community efforts during the last *lustrum*.

Probably, as a response to these limitations, it will become increasingly common in the next few years to find bioimage analysis specialists working alongside microscopists at bioimaging facilities and as researchers integrated within interdisciplinary research groups. Actually, in my experience, this is already happening in many research institutions. Apart from that, we also consider that it is important to include basic bioimage analysis training in the university curriculum for life scientists, as it has been the case with other flourishing techniques during the last decades. For example, this could help improve the setup of image-based experiments, which are typically designed and performed without considering how the analysis will be conducted. Moreover, without a basic understanding, users can often be at a loss when it comes to setting some workflows, since a certain amount of user intervention during parametrisation is almost inescapable. Actually, several parameters can be easily comprehended by life scientists, such as object size, but others that may be less familiar for them, such as filter types and kernel sizes. Thus, a basic understanding of the applied concepts would give a major independence to life scientists for the analysis and even allow them to customise already deployed workflows for their particular needs.

In order to provide user-friendly tools, all the practical workflows presented in this thesis include a GUI for parametrisation, which saves users from coding or learning to

use a CMI. In addition, we have tried to reduce the number of tweakable parameters as far as possible and to provide documentation to guide the installation and usage along with example datasets to practise. Moreover, we have introduced what we named pre-analysis workflows, which allow the users to conduct a pilot run on a subset of fields-of-view across the image dataset, after having set the parameters. This alternative analysis mode is intended to help users parameterise the workflow without having to run the analysis on the whole dataset. For that purpose, instead of quantitative data, the pre-analysis mode displays the segmentation output, usually color-coded to facilitate its visual inspection. If the user is not satisfied with the obtained result, parameters can be easily re-adjusted and the output easily re-evaluated. However, despite all these efforts, in our experience this alone does not allow users to totally circumvent the need of prior knowledge, which is the reason why we stand in favour of extending the bioimage analysis training to the end users. Additionally, the use of user-friendly, supervised ML approaches, such as ilastik, may provide practical solutions with the exchange of prior knowledge by an investment on training the computer to 'see' what the user is keen to find.

This raises some interesting questions, such as how the field will adapt to the age of DL, which, despite its drawbacks, is providing more generalist solutions that do not necessarily require prior bioimage analysis knowledge. Will the current trends lead to the disappearance of the classic image processing and ML methods? From an historical point of view, we can easily imagine a time when the appearance of the now classic ML methods surely raised similar doubts. However, ML has peacefully coexisted with the filter-based algorithms and other image analysis strategies. As it often happens, each approach has its own advantages and caveats. While most filter-based operations come from image processing, ML is a field within artificial intelligence. Due to its arithmetic nature, filter-based approaches are computationally faster whereas some ML approaches may increase the required memory and computation time. However, ML provides more flexibility since a classifier can be trained to use features which are more likely to be reusable across different image datasets, although this depends to a great extent on the training setup. This often implies the annotation of large datasets to train supervised classifiers. Conversely, as aforementioned, the use of filters usually requires the setting of a larger number of workflow parameters which hardly ever are entirely transferable for its use in different datasets and require prior knowledge. Nowadays, the current tendency is to rely on DL models for a variety of tasks such as image restoration (Weigert *et al.*, 2018), virtual staining (Rivenson *et al.*, 2019) or segmentation (Gómez-de-Mariscal *et al.*, 2019a). While DL has become in many cases the cutting-edge method to address a specific bioimage analysis problem, usually overperforming filter-

based and classical ML approaches, the requirement of (expensive) IT infrastructures has sometimes been a limitation. However, initiatives like DeepImageJ (Gómez-de-Mariscal *et al*, 2019b), a plugin for the generic use of pre-trained DL models (provided by their developers) in Fiji, are contributing enormously to democratise DL among the bioimage analysis community.

Resuming our question, the success of DL has led to theorizing about the extinction of the classical methods of bioimage analysis. However, in my opinion, it is most likely that all the methods will coexist, although DL, as it has happened in other fields, will have increasing relevance. Nonetheless, if we attend the bioimage analysis concept exposed in the Introduction section, practical workflows are made of different components and, as we have done in some workflows presented in this thesis, components based on different bioimage analysis paradigms can be combined to get the best of them. Indeed, as an illustrative example, the aforementioned DeepImageJ plugin enables the possibility to run any kind of preprocessing components along with the DL model, and then continue with the image processing. Namely, DeepImageJ offers the possibility to build a sequence where a DL model is embedded as the key component but it needs complementary image processing components to produce a practical bioimage analysis workflow. For example, a typical preprocessing step for the application of DL models is normalisation, since it aims to be applied to datasets generated from different microscopes which may have different bit-depths.

Indeed, the tendency is not only to provide easily executable DL models, but also to facilitate the training of new models by bioimage analysts and end users. This raises two possible strategies. One would be to generate a limited range of pre-trained DL models and put the effort into developing imaging setups and classic workflows aimed to get or transform each particular dataset to fit one of the available models. Alternatively, a more effective strategy could be to train a dedicated model on your own annotated data, as part of each analysis workflow. Regarding the first one, in the cell proliferation and apoptosis assay (**Chapter 2**), we decided to adapt the analysis setup in order to be able to use a pre-trained model from StarDist. Interestingly, it proved to be a very useful approach since not only prevented us from having to train the model ourselves, but also helped us to realise that we were previously oversampling our experiments and that a 2x2 binning provides sufficient resolution. Although convenient and faster, the usefulness of this modus operandi would be probably restricted to the segmentation of basic and common objects, as is the case of the DAPI stained nuclei. Complex image datasets from more specific biological scenarios would probably be difficult to accommodate to the demands of a generalist model and require their own training. On

the other hand, although our strategy in the neurosphere assay (**Chapter 3**) is not based in DL but in a ML random forest classifier, it may serve as an example of an assay where the application of generalist training models might not be as straightforward. In this case, the intrinsic characteristics of the experimental setup and the biological sample impose several technical difficulties (well-plate-specific strongly uneven illumination, slightly different focal plane between objects, three-dimensional nature of objects of interest...) that pose a great challenge for segmentation. In fact, we have deployed a complex workflow that includes an ilastik-based training for semantic segmentation that, even having included a very effective illumination correction step, generates a training model that is not always possible to reuse in a different dataset. Actually, in our experience, there is a great deal of experimental variability in this assay that, whereas it does not affect the manual analysis since the experimenter can easily make sense of the complexity and tell neurospheres from noise and artefacts, often prevents sharing the trained model between different experiments. Therefore, although the type of objects of interest in this assay (i.e., neurospheres) meets the requirements for the application of the generalistic StarDist 'star-convex shape' model, the mentioned aberrations might still impede this strategy. Having to train the model or the classifier for each dataset is, on the other hand, not that unreasonable if it were not for the increased computational time that it requires. To mitigate this, specially if the analyses are to be performed in a laptop instead of in a professional workstation (which in most cases should be the most efficient approach) it could be possible to adapt the workflow for the use of GPU-accelerated image processing with CLIJ (Haase *et al.*, 2020) for a faster performance.

The importance of sharing code, (meta)data and annotations

Reproducibility is a key element of science and it cannot be achieved without a rigorous and transparent process of reporting the methods and strategies employed to obtain the scientific data. This is of paramount importance, being the validation of scientific results by peer review a gold standard of science. Indeed, the interest of sharing data goes beyond the importance of reproducibility, being the improvement of data reusability an urgent goal for the scientific community. To this aim, a great effort is being made to endorse science with the FAIR Data Principles (Wilkinson *et al.*, 2016) for data management. Bioimage analysis is not unbound to these principles. As an eminently digital field, it can easily side with these practises. Consider for example the raw data: digital images are much easier to store and share than biological samples. The same happens with the bioimage analysis protocols, since they can easily be translated into code that not only contain all the workflow steps, but can also be used to execute

the same exact analysis. Additionally, image datasets include experimental and imaging metadata, which automatically store all the technical details. As for the result, apart from the raw and processed quantitative data, it is also possible to share the segmentation output or the manual annotations made by experts, reaching a level of transparency hardly achieved in the analysis of other types of biological samples. To empower the access to primary imaging data a series of community repositories have been deployed, such as the Image Data Resource **(Williams *et al*, 2017)**, a platform for the collection and integration of data acquired across many different bioimaging modalities along with relevant metadata and additional files, such as bioimage analysis scripts.

In the development of our tools, we have tried to adopt these principles and to facilitate the means to fulfil them to any user. To this aim, as already specified on the corresponding chapters, all our code is publicly available in GitHub. Moreover, for the workflows implying a greater parametrisation, the final setup is stored as a TXT file. This not only allows to reuse the parameter set on future experiments but, along with the code provided on GitHub, to share the detailed operations performed during the bioimage analysis. Additionally, all the workflows include the option to store the ROIs of the analysed objects.

Conclusions

C:66
M: 0
Y: 0
K: 0

R: 0
G:201
B:255

1. The development of high-content imaging and automated bioimage analysis methods for the study of cultured NSCs improves the throughput and the reproducibility of the *in vitro* assays.

2. The proposed experimental setup and analysis strategy for the static, cell-to-cell adhesion-based high-throughput assay is a reliable *in vitro* model for the assessment of the N-cadherin-mediated anchorage of isolated NSCs.

3. Diverse patterns of cell proliferation and viability can be identified by means of cell-based proliferation and apoptosis high-content screening assays.

4. The use of fabricated out-of-focus datasets facilitates the training of ML classifiers for the detection of fields-of-view affected by blur.

5. The automated bioimage analysis of 2D, screening-like imaged pseudo-clonal neurosphere formation assays generates data as accurate as human annotated.

6. ML-aided-human-supervised segmentation of fibre cross-sections on TEM images enables the extraction of classic and novel inner-tongue-based parameters for the study of (re)myelination and improves the bioimage analysis throughput.

Bibliography

C:41
M:78
Y: 0
K: 0

R:255
G: 0
B:255

Abdollahzadeh A., Belevich I., Jokitalo E., Tohka J. & Sierra A. (2019). Automated 3D Axonal Morphometry of White Matter. Sci Rep. 9(1):6084.

Arancibia-Carcamo I.L. & Attwell D. (2014). The node of Ranvier in CNS pathology. Acta Neuropathol. 128(2):161-175.

Arganda-Carreras I., Fernández-González R., Muñoz-Barrutia A. & Ortiz-De-Solorzano C. (2010). 3D Reconstruction of Histological Sections: Application to Mammary Gland Tissue. Microsc Res Tech. 73(11):1019-1029.

Arganda-Carreras I., Kaynig V., Rueden C., Eliceiri K.W., Schindelin J., Cardona A. & Seung H.S. (2017). Trainable Weka Segmentation: A Machine Learning Tool for Microscopy Pixel Classification. Bioinformatics. 33(15):2424-2426.

Arvidsson A., Collin T., Kirik D., Kokaia Z. & Lindvall O. (2002). Neuronal replacement from endogenous precursors in the adult brain after stroke. Nat Med. 8(9):963-970.

Baaklini C.S., Rawji K.S., Duncan G.J., Ho M.F.S. & Plemel J.R. (2019). Central Nervous System Remyelination: Roles of Glia and Innate Immune Cells. Front Mol Neurosci. 12:225.

Babaloukas G., Tentolouris N., Liatis S., Sklavounou A. & Perrea D. (2011). Evaluation of three methods for retrospective correction of vignetting on medical microscopy images utilizing two open source software tools. J Microsc. 244(3):320-324.

Bankhead P., Loughrey M.B., Fernández J.A., Dombrowski Y., McArt D.G., Dunne P.D., McQuaid S., Gray R.T., Murray L.J., Coleman H.G. et al. (2017). QuPath: Open source software for digital pathology image analysis. Sci Rep. 7(1):16878.

Bartyzel K. (2016). Adaptive Kuwahara filter. SIViP. 10:663–670.

Basak O., Krieger T.G., Muraro M.J., Wiebrands K., Stange D.E., Frias-Aldeguer J., Rivron N.C., van de Wetering M., van Es J.H., van Oudenaarden A. et al. (2018). Troy+ brain stem cells cycle through quiescence and regulate their number by sensing niche occupancy. Proc Natl Acad Sci U S A. 115(4):E610-E619.

Bégin S., Dupont-Therrien O., Bélanger E., Daradich A., Laffray S., De Koninck Y. & Côté D.C. (2014). Automated method for the segmentation and morphometry of nerve fibers in large-scale CARS images of spinal cord tissue. Biomed Opt Express. 5(12):4145-4161.

Belenguer G., Domingo-Muelas A., Ferrón S.R., Morante-Redolat J.M. & Fariñas I. (2016). Isolation, culture and analysis of adult subependymal neural stem cells. Differentiation. 91(4-5):28-41.

Belenguer G., Duart-Abadia P., Jordán-Pla A., Domingo-Muelas A., Blasco-Chamarro L., Ferrón S.R., Morante-Redolat J.M. & Fariñas I. (2020). Adult Neural Stem Cells Are Alerted by Systemic Inflammation through TNF-α Receptor Signaling. Cell Stem Cell. S1934-5909(20)30510-5.

Benner E.J., Luciano D., Jo R., Abdi K., Paez-Gonzalez P., Sheng H., Warner D.S., Liu C., Eroglu C. & Kuo C.T. (2013). Protective astrogenesis from the SVZ niche after injury is controlled by Notch modulator Thbs4. Nature. 497(7449):369-373.

Berg S., Kutra D., Kroeger T., Straehle C.N., Kausler B.X., Haubold C., Schiegg M., Ales J., Beier T., Rudy M. et al. (2019). ilastik: interactive machine learning for (bio)image analysis. Nat Methods. 16(12):1226-1232.

Best M.D. (2009). Click chemistry and bioorthogonal reactions: unprecedented selectivity in the labeling of biological molecules. Biochemistry. 48(28):6571-6584.

Bjornsson C.S., Apostolopoulou M., Tian Y. & Temple S. (2015). It takes a village: constructing the neurogenic niche. Dev Cell. 32(4):435-446.

Blakemore W.F. (1974). Pattern of remyelination in the CNS. Nature. 249(457):577-578.

Bond A.M., Ming G.L. & Song H. (2015). Adult Mammalian Neural Stem Cells and Neurogenesis: Five Decades Later. Cell Stem Cell. 17(4):385-395.

Borenstein E. & Ullman S. (2008). Combined top-down/bottom-up segmentation. IEEE Trans Pattern Anal Mach Intell. 30(12):2109-2125.

Boutros M., Heigwer F. & Laufer C. (2015). Microscopy-Based High-Content Screening. Cell. 163(6):1314-1325.

Bradski, G. (2000) The OpenCV Library. Dr. Dobb's Journal of Software Tools. 120:122-125.

Bray M.A., Fraser A.N., Hasaka T.P. & Carpenter A.E. (2012). Workflow and metrics for image quality control in large-scale high-content screens. J Biomol Screen. 17(2):266-274.

Bray M.A., Singh S., Han H., Davis C.T., Borgeson B., Hartland C., Kost-Alimova M., Gustafsdottir S.M., Gibson C.C. & Carpenter A.E. (2016). Cell Painting, a high-content image-based assay for morphological profiling using multiplexed fluorescent dyes. Nat Protoc. 11(9):1757-1774.

Breiman L. (2001). Random forests. Mach Learn. 45, 5-32.

Brock C.K., Wallin S.T., Ruiz O.E., Samms K.M., Mandal A., Sumner E.A. & Eisenhoffer G.T. (2019). Stem cell proliferation is induced by apoptotic bodies from dying cells during epithelial tissue maintenance. Nat Commun. 10(1):1044.

Brown, C.M. (2007). Fluorescence Microscopy - Avoiding the Pitfalls. J Cell Sci. 120(Pt 10):1703-1705.

Butler, L.M., McGettrick H.M., & Nash G.B. (2009) Static and dynamic assays of cell adhesion relevant to the vasculature. Methods Mol. Biol. 467, 211-228.

Caicedo J.C., Cooper S., Heigwer F., Warchal S., Qiu P., Molnar C., Vasilevich A.S., Barry J.D., Bansal H.S., Kraus O. et al. (2017) Data-analysis strategies for image-based cell profiling. Nat Methods. 14(9):849-863.

Caicedo J.C., Goodman A., Karhohs K.W., Cimini B.A., Ackerman J., Haghighi M., Heng C., Becker T., Doan M., McQuin C. et al. (2019a). Nucleus segmentation across imaging experiments: the 2018 Data Science Bowl. Nat Methods. 16(12):1247-1253.

Caicedo J.C., Roth J., Goodman A., Becker T., Karhohs K.W., Broisin M., Molnar C., McQuin C., Singh S., Theis F.J. et al. (2019b). Evaluation of Deep Learning Strategies for Nucleus Segmentation in Fluorescence Images. Cytometry A. 95(9):952-965.

Carpenter A.E., Jones T.R., Lamprecht M.R., Clarke C., Kang I.H., Friman O., Guertin D.A., Chang J.O., Lindquist R.A., Moffat J., Golland P. & Sabatini D.M. (2006). CellProfiler: Image Analysis Software for Identifying and Quantifying Cell Phenotypes. Genome Biol. 7(10):R100.

Carrillo-Barberà P., Morante-Redolat J.M., Pertusa J.F. (2019) Cell Proliferation High-Content Screening on Adherent Cell Cultures. In: Rebollo E., Bosch M. (eds) Computer Optimized Microscopy. Methods in Molecular Biology, vol 2040. Humana, New York, NY.

Chaker Z., Codega P. & Doetsch F. (2016). A mosaic world: puzzles revealed by adult neural stem cell heterogeneity. Wiley Interdiscip Rev Dev Biol. 5(6):640-658.

Chaki J. & Dey N. (2020). A Beginner's Guide to Image Shape Feature Extraction Techniques. Boca Raton: CRC Press.

Chambers K.M., Mandavilli B.S., Dolman N.J. & Janes M.S. (2018). General Staining and Segmentation Procedures for High Content Imaging and Analysis. In: Johnston P., Trask O. (eds) High Content Screening. Methods in Molecular Biology, vol 1683. Humana Press, New York, NY.

Chang K.J., Redmond S.A. & Chan J.R. (2016). Remodeling myelination: implications for mechanisms of neural plasticity. Nat Neurosci. 19(2):190-197.

Chau W.K., So K.F., Tay D. & Dockery P. (2000). A morphometric study of optic axons regenerated in a sciatic nerve graft of adult rats. Restor Neurol Neurosci. 16(2):105-116.

Chehrehasa F., Meedeniya A.C., Dwyer P., Abrahamsen G., Mackay-Sim A. (2009). EdU, a new thymidine analogue for labelling proliferating cells in the nervous system. J Neurosci Methods. 177(1):122-130.

Chen S., Lewallen M. & Xie T. (2013). Adhesion in the stem cell niche: biological roles and regulation. Development. 140(2):255-265.

Chen Y., Balasubramaniyan V., Peng J., Hurlock E.C., Tallquist M., Li J., Lu Q.R. (2007). Isolation and culture of rat and mouse oligodendrocyte precursor cells. Nat Protoc. 2(5):1044-1051.

Chipuk J.E., Bouchier-Hayes L. & Green D.R. (2006). Mitochondrial outer membrane permeabilization during apoptosis: the innocent bystander scenario. Cell Death Differ. 13(8):1396-402.

Cho I.J., Lui P.P., Obajdin J., Riccio F., Stroukov W., Willis T.L., Spagnoli F. & Watt F.M. (2019). Mechanisms, Hallmarks, and Implications of Stem Cell Quiescence. Stem Cell Reports. 12(6):1190-1200.

Chomiak T. & Hu B. (2009). What is the optimal value of the g-ratio for myelinated fibers in the rat CNS? A theoretical approach. PLoS One. 4(11):e7754.

Clausi D. A. & Ed Jernigan M. (2000). Designing Gabor filters for optimal texture separability. Pattern Recognition. 33:1835-1849.

Codega P., Silva-Vargas V., Paul A., Maldonado-Soto A.R., Deleo A.M., Pastrana E. & Doetsch F. (2014). Prospective identification and purification of quiescent adult neural stem cells from their in vivo niche. Neuron. 82(3):545-559.

Compston, A. & Coles, A. (2008). Multiple sclerosis. Lancet. 372, 1502-1517.

Crawford A.H., Tripathi R.B., Richardson W.D. & Franklin R.J.M. (2016). Developmental Origin of Oligodendrocyte Lineage Cells Determines Response to Demyelination and Susceptibility to Age-Associated Functional Decline. Cell Rep. 15(4):761-773.

D'Arcy M.S. (2019). Cell death: a review of the major forms of apoptosis, necrosis and autophagy. Cell Biol Int. 43(6):582-592.

Daynac M., Chicheportiche A., Pineda J.R., Gauthier L.R., Boussin F.D. & Mouthon M.A. (2013). Quiescent neural stem cells exit dormancy upon alteration of GABAAR signaling following radiation damage. Stem Cell Res. 11(1):516-528.

Dehghan S., Javan M., Pourabdolhossein F., Mirnajafi-Zadeh J. & Baharvand H. (2012). Basic fibroblast growth factor potentiates myelin repair following induction of experimental demyelination in adult mouse optic chiasm and nerves. J Mol Neurosci. 48(1):77-85.

Di Cataldo S. & Ficarra E. (2017). Mining textural knowledge in biological images: Applications, methods and trends. Comput Struct Biotechnol J. 15:56-67.

Dima A.A., Elliott J.T., Filliben J.J., Halter M., Peskin A., Bernal J., Kociolek M., Brady M.C., Tang H.C. & Plant A.L. (2011). Comparison of segmentation algorithms for fluorescence microscopy images of cells. Cytometry A. 79:545-559.

Doetsch F. & Alvarez-Buylla A. (1996). Network of tangential pathways for neuronal migration in adult mammalian brain. Proc Natl Acad Sci U S A. 93(25):14895-14900.

Doetsch F. (2003). The glial identity of neural stem cells. Nat Neurosci. 6(11):1127-1134.

Doetsch F., Caillé I., Lim D.A., García-Verdugo J.M. & Alvarez-Buylla A. (1999).

Subventricular zone astrocytes are neural stem cells in the adult mammalian brain. Cell. 97(6):703-716.

Doetsch F., García-Verdugo J.M. & Alvarez-Buylla A. (1997). Cellular composition and three-dimensional organization of the subventricular germinal zone in the adult mammalian brain. J Neurosci. 17(13):5046-5061.

Doetsch F., Petreanu L., Caille I., Garcia-Verdugo J.M. & Alvarez-Buylla A. (2002). EGF converts transit-amplifying neurogenic precursors in the adult brain into multipotent stem cells. Neuron. 36(6):1021-1034.

Dulken B.W., Leeman D.S., Boutet S.C., Hebestreit K. & Brunet A. (2017). Single-Cell Transcriptomic Analysis Defines Heterogeneity and Transcriptional Dynamics in the Adult Neural Stem Cell Lineage. 18(3):777-790.

Eidinoff M.L., Cheong L. & Rich M.A. (1959). Incorporation of unnatural pyrimidine bases into deoxyribonucleic acid of mammalian cells. Science. 129(3362):1550-1551.

Eliceiri K.W. (2012). Biological Imaging Software Tools. Nat Methods. 9(7):697-710.

Fancy S.P., Zhao C. & Franklin R.J. (2004). Increased expression of Nkx2.2 and Olig2 identifies reactive oligodendrocyte progenitor cells responding to demyelination in the adult CNS. Mol Cell Neurosci. 27(3):247-54.

Fathi E, Farahzadi R, Valipour B & Sanaat Z. (2019). Cytokines secreted from bone marrow derived mesenchymal stem cells promote apoptosis and change cell cycle distribution of K562 cell line as clinical agent in cell transplantation. PLoS One. 14(4):e0215678.

Ferrari Bardile C., Garcia-Miralles M., Caron N.S., Rayan N.A., Langley S.R., Harmston N., Rondelli A.M., Teo R.T.Y., Waltl S. & Anderson L.M. et al. (2019). Intrinsic mutant HTT-mediated defects in oligodendroglia cause myelination deficits and behavioral abnormalities in Huntington disease. Proc Natl Acad Sci U S A. 116(19):9622-9627.

Ferreira T.A. & Rasband W. (2012). The ImageJ User Guide – Version 1.46r. http://imagej.net/docs/guide/user-guide.pdf

Ferrón S.R., Andreu-Agullo C., Mira H., Sanchez P., Marques-Torrejon M.A. & Farinas I. (2007). A combined ex/in vivo assay to detect effects of exogenously added factors in neural stem cells. Nat Protoc. 2(4):849-859.

Ferrón S.R., Marqués-Torrejón M.A., Mira H., Flores I., Taylor K., Blasco M.A. & Fariñas I. (2009). Telomere shortening in neural stem cells disrupts neuronal differentiation and neuritogenesis. J Neurosci. 29(46):14394-14407.

Field D.J. & Brady N. (1997). Visual sensitivity, blur and the sources of variability in the amplitude spectra of natural scenes. Vision Res. 37(23):3367-3383.

Franklin R.J.M. & ffrench-Constant C. (2008). Remyelination in the CNS: from biology to therapy. Nat Rev Neurosci. 9(11):839-855.

Franklin R.J.M. & ffrench-Constant C. (2017). Regenerating CNS myelin - from mechanisms to experimental medicines. Nat Rev Neurosci. 18(12):753-769.

Franklin R.J.M. (2002). Why does remyelination fail in multiple sclerosis? Nat Rev Neurosci. 3(9):705-714.

Franklin R.J.M., ffrench-Constant C., Edgar J.M. & Smith K.J. (2012). Neuroprotection and repair in multiple sclerosis. Nat Rev Neurol. 8(11):624-634.

Franklin R.J.M., Gilson J.M. & Blakemore W.F. (1997). Local recruitment of remyelinating cells in the repair of demyelination in the central nervous system. J Neurosci Res. 50(2):337-344.

Frühbeis C., Fröhlich D., Kuo W.P., Amphornrat J., Thilemann S., Saab A.S., Kirchhoff F., Möbius W., Goebbels S., Nave K.A. et al. (2013). Neurotransmitter-triggered transfer of exosomes mediates oligodendrocyte-neuron communication. PLoS Biol. 11(7):e1001604.

Fuentealba L.C., Obernier K. & Alvarez-Buylla A. (2012). Adult neural stem cells bridge their niche. Cell Stem Cell. 10(6):698-708.

Fuentealba L.C., Rompani S.B., Parraguez J.I., Obernier K., Romero R., Cepko C.L. & Alvarez-Buylla A. (2015). Embryonic Origin of Postnatal Neural Stem Cells. Cell. 161(7):1644-1655.

Fujita J., Crane A.M., Souza M.K., Dejosez M., Kyba M., Flavell R.A., Thomson J.A. & Zwaka T.P. (2008) Caspase activity mediates the differentiation of embryonic stem cells. Cell Stem Cell. 2(6):595-601.

Fünfschilling U., Supplie L.M., Mahad D., Boretius S., Saab A.S., Edgar J., Brinkmann B.G., Kassmann C.M., Tzvetanova I.D., Möbius W. et al. (2012). Glycolytic oligodendrocytes maintain myelin and long-term axonal integrity. Nature. 485(7399):517-521.

Furutachi S., Miya H., Watanabe T., Kawai H., Yamasaki N., Harada Y., Imayoshi I., Nelson M., Nakayama K.I., Hirabayashi et al. (2015). Slowly dividing neural progenitors are an embryonic origin of adult neural stem cells. Nat Neurosci. 18(5):657-665.

Galluzzi L., López-Soto A., Kumar S. & Kroemer G. (2016). Caspases Connect Cell-Death Signaling to Organismal Homeostasis. Immunity. 44(2):221-231.

Gensert J.M. & Goldman J.E. (1997). Endogenous progenitors remyelinate demyelinated axons in the adult CNS. Neuron. 19(1):197-203.

Geurts P., Irrthum A. & Wehenkel L. (2009). Supervised learning with decision tree-based methods in computational and systems biology. Mol BioSyst. 5(12) 1593-1605.

Giacci M.K., Bartlett C.A., Huynh M., Kilburn M.R., Dunlop S.A. & Fitzgerald M. (2018). Three dimensional electron microscopy reveals changing axonal and myelin morphology along normal and partially injured optic nerves. Sci Rep. 8(1):3979.

Giachino C., Basak O., Lugert S., Knuckles P., Obernier K., Fiorelli R., Frank S., Raineteau O.,

Alvarez-Buylla A. & Taylor V. (2014). Molecular diversity subdivides the adult forebrain neural stem cell population. Stem Cells. 32(1):70-84.

Gómez-de-Mariscal E., García-López-de-Haro C., Donati L., Unser M., Muñoz-Barrutia A. & Sage D. (2019b). DeepImageJ: A user-friendly plugin to run deep learning models in ImageJ. BioRxiv. DOI: https://doi.org/10.1101/799270

Gómez-de-Mariscal E., Maška M., Kotrbová A., Pospíchalová V., Matula P. & Muñoz-Barrutia A. (2019a). Deep-Learning-Based Segmentation of Small Extracellular Vesicles in Transmission Electron Microscopy Images. Sci Rep. 9(1):13211.

Groen, F.C. Young I.T. & Ligthart G. (1985). A comparison of different focus functions for use in autofocus algorithms. Cytometry 6(2)81-91.

Grys B.T., Lo D.S., Sahin N., Kraus O.Z., Morris Q., Boone C. & Andrews B.J. (2017). Machine Learning and Computer Vision Approaches for Phenotypic Profiling. J Cell Biol. 216(1):65-71.

Gudla P.R., Nandy K., Collins J., Meaburn K.J., Misteli T. & Lockett S.J. (2008). A high-throughput system for segmenting nuclei using multiscale techniques. Cytometry A. 73:451-466.

Guiet R., Burri O. & Seitz A. (2019). Open Source Tools for Biological Image Analysis. In: Rebollo E., Bosch M. (eds) Computer Optimized Microscopy. Methods in Molecular Biology, vol 2040. Humana, New York, NY.

Guo Z.B., Su Y.Y., Wang Y.H., Wang W. & Guo D.Z. (2016). The expression pattern of Adam10 in the central nervous system of adult mice: Detection by in situ hybridization combined with immunohistochemistry staining. Mol Med Rep. 14(3):2038-2044.

Gustafsdottir S.M., Ljosa V., Sokolnicki K.L., Anthony Wilson J., Walpita D., Kemp M.M., Petri Seiler K., Carrel H.A., Golub T.R., Schreiber S.L. et al. (2013). Multiplex cytological profiling assay to measure diverse cellular states. PLoS One. 8(12):e80999.

Haase R., Royer L.A., Steinbach P., Schmidt D., Dibrov A., Schmidt U., Weigert M., Maghelli N., Tomancak P., Jug F. et al. (2019). CLIJ: GPU-accelerated image processing for everyone. Nat Methods. 17(1):5-6.

Hampton D.W., Innes N., Merkler D., Zhao C., Franklin R.J. & Chandran S. (2012). Focal immune-mediated white matter demyelination reveals an age-associated increase in axonal vulnerability and decreased remyelination efficiency. Am J Pathol. 180(5):1897-1905.

Haralick R.M. (1979). Statistical and structural approaches to texture. Proc IEEE. 67(5):786-804.

Haralick R.M., Shanmugam K. & Dinstein I. (1973). Textural features for image classification. IEEE Trans. Syst. Man Cybern. SM C-3:610-621.

Hernández Candia C.N. & Gutiérrez-Medina B. (2014). Direct Imaging of Phase Objects Enables Conventional Deconvolution in Bright Field Light Microscopy. PLoS One. 9(2):e89106.

Higham D. J. & Higham N. J. (2016). MATLAB guide (Vol. 150). Siam.

Hua K. & Ferland R.J. (2017). Fixation methods can differentially affect ciliary protein immunolabeling. Cilia. 6:5.

Hughes E.G., Kang S.H., Fukaya M. & Bergles D.E. (2013). Oligodendrocyte progenitors balance growth with self-repulsion to achieve homeostasis in the adult brain. Nat Neurosci. 16(6):668-676.

Humphries, M.J. (2009) Cell adhesion assays. Methods Mol. Biol. 522, 203-210.

International Multiple Sclerosis Genetics Consortium, Wellcome Trust Case Control Consortium, Sawcer S., Hellenthal G., Pirinen M., Spencer C.C., Patsopoulos N.A., Moutsianas L., Dilthey A., Su Z. et al. (2011). Genetic risk and a primary role for cell-mediated immune mechanisms in multiple sclerosis. Nature. 476(7359):214-219.

Jarvis RA. (1973). On the identification of the convex hull of a finite set of points in the plane. Inf Process Lett. 2(1):18-21.

Jensen J.B. & Parmar M. (2006). Strengths and limitations of the neurosphere culture system. Mol Neurobiol.34(3):153-161.

Jones T.R., Carpenter A.E., Lamprecht M.R., Moffat J., Silver S.J., Grenier J.K., Castoreno A.B., Eggert U.S., Root D.E., Golland P. & Sabatini D.M. (2009). Scoring diverse cellular morphologies in image-based screens with iterative feedback and machine learning. Proc Natl Acad Sci U S A. 106(6):1826-1831.

Jones T.R., Kang I.H., Wheeler D.B., Lindquist R.A., Papallo A., Sabatini D.M, Golland P. & Carpenter A.E. (2008). CellProfiler Analyst: data exploration and analysis software for complex image-based screens. BMC Bioinformatics. 9:482.

Jost A.P.T & Waters J.C. (2019). Designing a Rigorous Microscopy Experiment: Validating Methods and Avoiding Bias. J Cell Biol. 218(5):1452-1466.

Kamentsky L., Jones T.R., Fraser A., Bray M.A., Logan D.J., Madden K.L., Ljosa V., Rueden C., Eliceiri K.W. & Carpenter A.E. (2011). Improved structure, function and compatibility for CellProfiler: modular high-throughput image analysis software. Bioinformatics. 27(8):1179-1180.

Kan A. (2017). Machine Learning Applications in Cell Image Analysis. Immunol Cell Biol. 95(6):525-530.

Kapałczyńska M., Kolenda T., Przybyła W., Zajączkowska M., Teresiak A., Filas V., Ibbs M., Bliźniak R., Łuczewski Ł. & Lamperska K. (2018). 2D and 3D cell cultures - a comparison of different types of cancer cell cultures. Arch Med Sci. 14(4):910-919.

Kärkkäinen I., Rybnikova E., Pelto-Huikko M. & Huovila AP. (2000). Metalloprotease-disintegrin (ADAM) genes are widely and differentially expressed in the adult CNS. Mol Cell Neurosci. 15(6):547-560.

Karpowicz (2009). E-Cadherin regulates neural stem cell self-renewal. J. Neurosci. 29, 3885-3896.

Kazanis I., Evans K.A., Andreopoulou E., Dimitriou C., Koutsakis C., Karadottir R.T. & Franklin R.J.M. (2017). Subependymal Zone-Derived Oligodendroblasts Respond to Focal Demyelination but Fail to Generate Myelin in Young and Aged Mice. Stem Cell Reports. 8(3):685-700.

Kimura M., Sato M., Akatsuka A., Nozawa-Kimura S., Takahashi R., Yokoyama M., Nomura T. & Katsuki M. (1989). Restoration of myelin formation by a single type of myelin basic protein in transgenic shiverer mice. Proc Natl Acad Sci U S A. 86(14):5661-5665.

Kolb H.C., Finn M.G. & Sharpless K.B. (2001). Click Chemistry: Diverse Chemical Function from a Few Good Reactions. Angew Chem Int Ed Engl. 40(11):2004-2021.

Kreshuk A., Koethe U., Pax E., Bock D.D. & Hamprecht F.A. (2014). Automated detection of synapses in serial section transmission electron microscopy image stacks. PLoS One. 9(2):e87351.

Kreshuk A., Zhang C. (2019) Machine Learning: Advanced Image Segmentation Using ilastik. In: Rebollo E., Bosch M. (eds) Computer Optimized Microscopy. Methods in Molecular Biology, vol 2040. Humana, New York, NY

Kriegstein A. & Alvarez-Buylla A. (2009). The glial nature of embryonic and adult neural stem cells. Annu Rev Neurosci. 32:149-184.

Krull A., Vičar T., Prakash M., Lalit M. & Jug F. (2020). Probabilistic Noise2Void: Unsupervised Content-Aware Denoising. Front Comput Sci. 2:5.

Kuwahara M., Hachimura K., Eiho S. & Kinoshita M. (1976). Processing of RI-Angiocardiographic Images. In: Preston K., Onoe M. (eds) Digital Processing of Biomedical Images. Springer, Boston, MA.

Lalli G. (2014). Extracellular signals controlling neuroblast migration in the postnatal brain. Adv Exp Med Biol. 800:149-80.

Landini G., Galton A., Randell D. & Fouad S. (2019). Novel applications of Discrete Mereotopology to Mathematical Morphology. Signal Process. Image Commun. 76:109-117.

Lauterbach M.A. (2012). Finding, defining and breaking the diffraction barrier in microscopy – a historical perspective. Opt Nano. 1, 8.

Leckband DE & de Rooij J. (2014). Cadherin adhesion and mechanotransduction. Annu Rev Cell Dev Biol. 30:291-315.

Lee Y., Morrison B.M., Li Y., Lengacher S., Farah M.H., Hoffman P.N., Liu Y., Tsingalia A., Jin L., Zhang P.W. et al. (2012). Oligodendroglia metabolically support axons and contribute to neurodegeneration. Nature. 487(7408):443-448.

Legland D., Arganda-Carreras I. & Andrey P. (2016). MorphoLibJ: integrated library and plugins for mathematical morphology with ImageJ. Bioinformatics. 32(22):3532-3534.

Levine J.M. & Reynolds R. (1999). Activation and proliferation of endogenous oligodendrocyte precursor cells during ethidium bromide-induced demyelination. Exp Neurol. 160(2):333-347.

Likar B., Maintz J.B., Viergever M.A. & Pernus F. (2000). Retrospective shading correction based on entropy minimization. J Microsc. 197(Pt 3):285-295.

Lin T., Xiang Z., Cui L., Stallcup W. & Reeves S.A. (2006). New mouse oligodendrocyte precursor (mOP) cells for studies on oligodendrocyte maturation and function. J Neurosci Methods. 157(2):187-194.

Linkert M., Rueden C.T., Allan C., Burel J.M., Moore W., Patterson A., Loranger B., Moore J., Neves C., Macdonald D. et al. (2010). Metadata matters: access to image data in the real world. J Cell Biol. 189(5):777-782.

Liu L., Michowski W., Kolodziejczyk A. & Sicinski P. (2019). The cell cycle in stem cell proliferation, pluripotency and differentiation. Nat Cell Biol. 21(9):1060-1067.

Liu T., Jurrus E., Seyedhosseini M., Ellisman M. & Tasdizen T. (2012). Watershed Merge Tree Classification for Electron Microscopy Image Segmentation. Proc IAPR Int Conf Pattern Recogn. 2012:133-137.

Livneh Y., Adam Y. & Mizrahi A. (2014). Odor processing by adult-born neurons. Neuron. 81(5):1097-1110.

Ljosa V., Sokolnicki K.L. & Carpenter A.E. (2012). Annotated high-throughput microscopy image sets for validation [published correction appears in Nat Methods. 2013 May;10(5):445]. Nat Methods. doi:10.1038/nmeth.2083

Lledo P.M. & Saghatelyan A. (2005). Integrating new neurons into the adult olfactory bulb: joining the network, life-death decisions, and the effects of sensory experience. Trends Neurosci. 28(5):248-254.

Lledo P.M. & Valley M. (2016). Adult Olfactory Bulb Neurogenesis. Cold Spring Harb Perspect Biol. 8(8):a018945.

Llorens-Bobadilla E., Zhao S., Baser A., Saiz-Castro G., Zwadlo K. & Martin-Villalba A. (2015) Single-Cell Transcriptomics Reveals a Population of Dormant Neural Stem Cells that Become Activated upon Brain Injury. Cell Stem Cell. 17(3):329-340.

Lo Sardo V., Zuccato C., Gaudenzi G., Vitali B., Ramos C., Tartari M., Myre M.A., Walker J.A., Pistocchi A., et al. (2012). An evolutionary recent neuroepithelial cell adhesion function

of huntingtin implicates ADAM10-Ncadherin. Nat Neurosci. 15(5):713-721.

Löfstedt T., Brynolfsson P., Asklund T., Nyholm T. & Garpebring A. (2019). Gray-level invariant Haralick texture features. PloS one, 14(2):e0212110.

Lois C., García-Verdugo J.M. & Alvarez-Buylla A. (1996). Chain migration of neuronal precursors. Science. 271(5251):978-981.

Lou X., Fiaschi L., Koethe U. & Hamprecht F.A. (2012). Quality Classification of Microscopic Imagery with Weakly Supervised Learning. In: Wang F., Shen D., Yan P., Suzuki K. (eds) Machine Learning in Medical Imaging. MLMI 2012. Lecture Notes in Computer Science, vol 7588. Springer, Berlin, Heidelberg

Louis S.A., Rietze R.L., Deleyrolle L., Wagey R.E., Thomas T.E., Eaves A.C. & Reynolds B.A. (2008). Enumeration of neural stem and progenitor cells in the neural colony-forming cell assay. Stem Cells. 26(4):988-996.

Ludwin S.K. (2000). Understanding multiple sclerosis: lessons from pathology. Ann Neurol. 47(6):691-693.

Malik A., Jamasbi R.J., Kondratov R.V. & Geusz M.E. (2015). Development of circadian oscillators in neurosphere cultures during adult neurogenesis. PLoS One. 10(3):e0122937.

Mandavilli B.S., Yan M. & Clarke S. (2018). Cell-Based High Content Analysis of Cell Proliferation and Apoptosis. In: Johnston P., Trask O. (eds) High Content Screening. Methods in Molecular Biology, vol 1683. Humana Press, New York, NY.

Marthiens V., Kazanis I., Moss L., Long K. & Ffrench-Constant C. (2010). Adhesion molecules in the stem cell niche--more than just staying in shape? J Cell Sci. 123(Pt 10):1613-1622.

Martynoga B., Mateo J.L., Zhou B., Andersen J., Achimastou A., Urbán N., van den Berg D., Georgopoulou D., Hadjur S., Wittbrodt J. et al. (2013). Epigenomic enhancer annotation reveals a key role for NFIX in neural stem cell quiescence. Genes Dev.(16):1769-1786.

McIlwain D.R., Berger T. & Mak T.W. (2015). Caspase functions in cell death and disease. Cold Spring Harb Perspect Biol. 7(4):a026716.

McQuin C., Goodman A., Chernyshev V., Kamentsky L., Cimini B.A., Karhohs K.W., Doan M., Ding L., Rafelski S.M., Thirstrup D., Wiegraebe W., Singh S., Becker T., Caicedo J.C. & Carpenter A.E. (2018). CellProfiler 3.0: Next-generation Image Processing for Biology. PLoS Biol. 16(7):e2005970.

Medina-Rodríguez E.M., Arenzana F.J., Bribián A. & de Castro F. (2013). Protocol to isolate a large amount of functional oligodendrocyte precursor cells from the cerebral cortex of adult mice and humans. PLoS One. 8(11):e81620.

Meek D.W. (2009). Tumour suppression by p53: a role for the DNA damage response? Nat Rev Cancer. 9(10):714-723.

Mei F., Lehmann-Horn K., Shen Y.A., Rankin K.A., Stebbins K.J., Lorrain D.S., Pekarek K., A Sagan S., Xiao L., Teuscher C. et al. (2016). Accelerated remyelination during inflammatory demyelination prevents axonal loss and improves functional recovery. Elife. 5:e18246.

Meijering E., Carpenter A.E., Peng H., Hamprecht F.A. & Olivo-Marin J.C. (2016). Imagining the Future of Bioimage Analysis. Nat Biotechnol. 34(12):1250-1255.

Menn B., Garcia-Verdugo J.M., Yaschine C., Gonzalez-Perez O., Rowitch D. & Alvarez-Buylla A. (2006). Origin of oligodendrocytes in the subventricular zone of the adult brain. J Neurosci. 26(30):7907-7018.

Merrill J.E. (2009). In vitro and in vivo pharmacological models to assess demyelination and remyelination. Neuropsychopharmacology. 34(1):55-73.

Meschkat M., Steyer A.M., Weil M.T., Kusch K., Jahn O., Piepkorn L., Agüi-Gonzalez P., Ngoc Phan N.T., Ruhwedel T., Sadowski B. et al. (2020). White matter integrity requires continuous myelin synthesis at the inner tongue. BioRxiv. DOI: https://doi.org/10.1101/2020.09.02.279612

Messersmith D.J., Murtie J.C., Le T.Q., Frost E.E. & Armstrong R.C. (2000). Fibroblast growth factor 2 (FGF2) and FGF receptor expression in an experimental demyelinating disease with extensive remyelination. J Neurosci Res. 62(2):241-256.

Mich J.K., Signer R.A., Nakada D., Pineda A., Burgess R.J., Vue T.Y., Johnson J.E. & Morrison S.J. (2014). Prospective identification of functionally distinct stem cells and neurosphere-initiating cells in adult mouse forebrain. Elife. 3:e02669.

Michalski J.P. & Kothary R. (2015). Oligodendrocytes in a Nutshell. Front Cell Neurosci. 9:340.

Mirzadeh Z., Merkle F.T., Soriano-Navarro M., Garcia-Verdugo J.M. & Alvarez-Buylla A. (2008). Neural stem cells confer unique pinwheel architecture to the ventricular surface in neurogenic regions of the adult brain. Cell Stem Cell. 3(3):265-278.

Miura M., Paul-Gilloteaux P., Tosi S. & Colombelli J. (2017). Workflows and Components of Bioimage Analysis: The NEUBIAS Concept. Zenodo. DOI: 10.5281/zenodo.1042570.

Miura K., Tosi S., Möhl C., Zhang C., Paul-Gilloteaux P., Schulze U., Nørrelykke S.F., Tischer C. & Pengo C. (2016). Bioimage Analysis Tools. In: Miura K. (ed) Bioimage Data Analysis. Wiley-VCH, Heidelberg.

Möbius W., Cooper B., Kaufmann W.A., Imig C., Ruhwedel T., Snaidero T., Saab A.S. & Varoqueaux F. (2010). Electron microscopy of the mouse central nervous system. Methods Cell Biol. 96:475-512.

Mobley, J.L. & Shimizu Y. (2001) Measurement of cellular adhesion under static conditions. Curr. Protoc. Immunol. Chapter 7: Unit 7.28

Model M. (2014). Intensity calibration and flat-field correction for fluorescence

microscopes. Curr Protoc Cytom. 68:10.14.1-10.

Moiseev D., Hu B. & Li J. (2019). Morphometric analysis of peripheral myelinated nerve fibers through deep learning. J Peripher Nerv Syst. 24(1):87-93.

Molnar C., Jermyn I.H., Kato Z., Rahkama V., Östling P., Mikkonen P., Pietiäinen V. & Horvath P. (2016). Accurate Morphology Preserving Segmentation of Overlapping Cells based on Active Contours. 6:32412.

Molnar C., Kato Z. & Jermyn I. A Multi-Layer Phase Field Model for Extracting Multiple Near-Circular Objects. In ICPR 2012: Proceedings of 21st International Conference on Pattern Recognition, 1427-1430, Tsukuba, Japan, IEEE (2012).

Morante-Redolat J.M. & Porlan E. (2019). Neural Stem Cell Regulation by Adhesion Molecules Within the Subependymal Niche. Front Cell Dev Biol. 7:102.

More H.L., Chen J., Gibson E., Donelan J.M. & Beg M.F. (2011). A semi-automated method for identifying and measuring myelinated nerve fibers in scanning electron microscope images. J Neurosci Methods. 201(1):149-158.

Morizur L., Chicheportiche A., Gauthier L.R., Daynac M., Boussin F.D. & Mouthon M.A. (2018). Distinct Molecular Signatures of Quiescent and Activated Adult Neural Stem Cells Reveal Specific Interactions with Their Microenvironment. Stem Cell Reports. 11(2):565-577.

Morrison B.M., Lee Y. & Rothstein J.D. (2013) Oligodendroglia: metabolic supporters of axons. Trends Cell Biol. 23(12):644-651.

Moyon S., Dubessy A.L., Aigrot M.S., Trotter M., Huang J.K., Dauphinot L., Potier M.C., Kerninon C., Melik Parsadaniantz S., Franklin R.J. et al. (2015). Demyelination causes adult CNS progenitors to revert to an immature state and express immune cues that support their migration. J Neurosci. 35(1):4-20.

Murtie J.C., Zhou Y.X., Le T.Q., Vana A.C. & Armstrong R.C. (2005). PDGF and FGF2 pathways regulate distinct oligodendrocyte lineage responses in experimental demyelination with spontaneous remyelination. Neurobiol Dis. 19(1-2):171-182.

Myers G. (2012). Why Bioimage Informatics Matters. 9(7):659-660.

Nait-Oumesmar B., Decker L., Lachapelle F., Avellana-Adalid V., Bachelin C. & Baron-Van Evercooren A. (1999). Progenitor cells of the adult mouse subventricular zone proliferate, migrate and differentiate into oligodendrocytes after demyelination. Eur J Neurosci. 11(12):4357-66.

Nave K.A. (2010). Myelination and the trophic support of long axons. Nat Rev Neurosci. 11(4):275-283.

Nixon M.S. & Aguado A.S. (2012). Low-level feature extraction (including edge detection). In: Nixon M.S. & Aguado A.S. (eds) Feature Extraction & Image Processing for Computer

Vision (Third Edition). Academic Press.

Obernier K. & Alvarez-Buylla A. (2019). Neural stem cells: origin, heterogeneity and regulation in the adult mammalian brain. Development. 146(4):dev156059.

Obernier K., Cebrian-Silla A., Thomson M., Parraguez J.I., Anderson R., Guinto C., Rodas Rodriguez J., Garcia-Verdugo J.M. & Alvarez-Buylla A. (2018). Adult Neurogenesis Is Sustained by Symmetric Self-Renewal and Differentiation. Cell Stem Cell. 22(2):221-234. e8.

Ortega F., Gascón S., Masserdotti G., Deshpande A., Simon C., Fischer J., Dimou L., Chichung Lie D., Schroeder T. & Berninger B. (2013). Oligodendrogliogenic and neurogenic adult subependymal zone neural stem cells constitute distinct lineages and exhibit differential responsiveness to Wnt signalling. Nat Cell Biol. 15(6):602-613.

Otsu N. (1979). A thresholding selection method from gray-level histograms IEEE Trans System Man Cybernetic. 62-66.

Pastrana E., Cheng L.C. & Doetsch F. (2009). Simultaneous prospective purification of adult subventricular zone neural stem cells and their progeny. Proc Natl Acad Sci U S A. 106(15):6387-92.

Pastrana E., Silva-Vargas V. & Doetsch F. (2011). Eyes wide open: a critical review of sphere-formation as an assay for stem cells. Cell Stem Cell. 8(5):486-498.

Peng T., Thorn K., Schroeder T., Wang L., Theis F.J., Marr C. & Navab N. (2017). A BaSiC tool for background and shading correction of optical microscopy images. Nat Commun. 8:14836.

Perona P. & Malik J. (1990). Scale-space and edge detection using anisotropic diffusion. IEEE T Pattern Anal. 12(7):629-639.

Pertusa J.F. & Morante-Redolat J.M. (2019). Main Steps in Image Processing and Quantification: The Analysis Workflow. In: Rebollo E., Bosch M. (eds) Computer Optimized Microscopy. Methods in Molecular Biology, vol 2040. Humana, New York, NY.

Pfeifenbring S., Nessler S., Wegner C., Stadelmann C. & Brück W. (2015). Remyelination After Cuprizone-Induced Demyelination Is Accelerated in Juvenile Mice. J Neuropathol Exp Neurol. 74(8):756-766.

Picard-Riera N., Decker L., Delarasse C., Goude K., Nait-Oumesmar B., Liblau R., Pham-Dinh D. & Baron-Van Evercooren A. (2002). Experimental autoimmune encephalomyelitis mobilizes neural progenitors from the subventricular zone to undergo oligodendrogenesis in adult mice. Proc Natl Acad Sci U S A. 99(20):13211-13216.

Pietzsch T., Preibisch S., Tomančák P. & Saalfeld S. (2012). ImgLib2 - generic image processing in Java. Bioinformatics. 28(22):3009-3011.

Plemel J.R., Manesh S.B., Sparling J.S. & Tetzlaff W. (2013). Myelin inhibits oligodendroglial

maturation and regulates oligodendrocytic transcription factor expression. Glia. 61(9):1471-1487.

Polito A. & Reynolds R. (2005). NG2-expressing cells as oligodendrocyte progenitors in the normal and demyelinated adult central nervous system. J Anat. 207(6):707-716.

Ponti G., Obernier K., Guinto C., Jose L., Bonfanti L. & Alvarez-Buylla A. (2013). Cell cycle and lineage progression of neural progenitors in the ventricular-subventricular zones of adult mice. Proc Natl Acad Sci U S A. 110(11):E1045-1054.

Porlan E., Martí-Prado B., Morante-Redolat J.M., Consiglio A., Delgado A.C, Kypta R., López-Otín C., Kirstein M. & Fariñas I. (2014). MT5-MMP regulates adult neural stem cell functional quiescence through the cleavage of N-cadherin. Nat Cell Biol. 16(7):629-638.

Porlan E., Perez-Villalba A., Delgado A.C., Ferrón S.R. (2013). Paracrine regulation of neural stem cells in the subependymal zone. Arch Biochem Biophys. 534(1-2):11-19.

Preibisch S., Saalfeld S. & Tomancak P. (2009). Globally optimal stitching of tiled 3D microscopic image acquisitions. Bioinformatics. 25(11):1463-1465.

Qu L., Long F. & Peng H. (2015). 3-D Registration of Biological Images and Models: Registration of microscopic images and its uses in segmentation and annotation. IEEE Signal Process Mag. 32(1):70-77.

R Core Team. (2016). R: A Language and Environment for Statistical Computing. Vienna, Austria.

Rasband M.N. & Peles E. (2015). The Nodes of Ranvier: Molecular Assembly and Maintenance. Cold Spring Harb Perspect Biol. 8(3):a020495.

Reynolds B.A. & Rietze R.L. (2005). Neural stem cells and neurospheres--re-evaluating the relationship. Nat Methods. 2005 May;2(5):333-6.

Reynolds B.A. & Weiss S. (1992). Generation of neurons and astrocytes from isolated cells of the adult mammalian central nervous system. Science. 255(5052):1707-1710.

Richards L.J., Kilpatrick T.J. & Bartlett P.F. (1992). De novo generation of neuronal cells from the adult mouse brain. Proc Natl Acad Sci U S A. 89(18):8591-8595.

Rietze R.L. & Reynolds B.A. (2006). Neural stem cell isolation and characterization. Methods Enzymol. 419:3-23.

Rittchen S., Boyd A., Burns A., Park J., Fahmy T.M., Metcalfe S. & Williams A. (2015). Myelin repair in vivo is increased by targeting oligodendrocyte precursor cells with nanoparticles encapsulating leukaemia inhibitory factor (LIF). Biomaterials. 56:78-85.

Rivenson Y., Wang H., Wei Z., de Haan K., Zhang Y., Wu Y., Günaydın H., Zuckerman J.E., Chong T., Sisk A.E. et al. (2019). Virtual histological staining of unlabelled tissue-autofluorescence images via deep learning. Nat Biomed Eng. 3(6):466-477.

Rodenacker K. & Bengtsson E. (2003). A Feature Set for Cytometry on Digitized Microscopic Images. Anal Cell Pathol. 25(1):1-36.

Romero E., Cuisenaire O., Denef J.F., Delbeke J., Macq B. & Veraart C. (2000). Automatic morphometry of nerve histological sections. J Neurosci Methods. 97(2):111-122.

Rueden C.T., Schindelin J., Hiner M.C., DeZonia B.E., Walter A.E., Arena E.T. & Eliceiri K.W. (2017). ImageJ2: ImageJ for the next generation of scientific image data. BMC Bioinformatics. 18(1):529.

Rushton W.A. (1951). A theory of the effects of fibre size in medullated nerve. J Physiol. 115(1):101-122.

Ryoo H.D. & Bergmann A. (2012). The role of apoptosis-induced proliferation for regeneration and cancer. Cold Spring Harb Perspect Biol. 4(8):a008797.

Ryu J.R., Hong C.J., Kim J.Y., Kim E.K., Sun W. & Yu S.W. (2016). Control of adult neurogenesis by programmed cell death in the mammalian brain. Mol Brain. 9:43.

Samanta J., Grund E.M., Silva H.M., Lafaille J.J., Fishell G. & Salzer J.L. (2015). Inhibition of Gli1 mobilizes endogenouss neural stem cells for remyelination. Nature. 526(7573):448-452.

Sbalzarini I.F. (2016). Seeing Is Believing: Quantifying Is Convincing: Computational Image Analysis in Biology. In: De Vos W., Munck S., Timmermans JP. (eds) Focus on Bio-Image Informatics. Advances in Anatomy, Embryology and Cell Biology, vol 219. Springer, Cham.

Schindelin J., Arganda-Carreras I., Frise E., Kaynig V., Longair M., Pietzsch T., Preibisch S., Rueden C., Saalfeld S. & Schmid S. (2012). Fiji: an open-source platform for biological-image analysis. Nat Methods. 9(7):676-682.

Schmidt U., Weigert M., Broaddus C. & Myers G. Cell Detection with Star-convex Polygons. International Conference on Medical Image Computing and Computer-Assisted Intervention (MICCAI), Granada, Spain, September 2018.

Schneider C.A., Rasband W.S., Eliceiri K.W. (2012). NIH Image to ImageJ: 25 years of image analysis. Nat Methods. 9(7):671-675.

Schroeder W., Martin K. & Lorensen B. (2006). The Visualization Toolkit (4th ed.). Kitware

Serra J. (1986). Introduction to mathematical morphology. Comput Gr Image Process. 35(3):283-305.

Shamir L., Delaney J.D., Orlov N., Eckley D.M. & Goldberg I.G. (2010). Pattern Recognition Software and Techniques for Biological Image Analysis. PLoS Comput Biol. 6(11):e1000974.

Shields S.A., Gilson J.M., Blakemore W.F. & Franklin R.J. (1999). Remyelination occurs as extensively but more slowly in old rats compared to young rats following gliotoxin-

induced CNS demyelination. Glia. 28(1):77-83.

Silva-Vargas V., Maldonado-Soto A.R., Mizrak D., Codega P. & Doetsch F. (2016). Age-Dependent Niche Signals from the Choroid Plexus Regulate Adult Neural Stem Cells. Cell Stem Cell. 19(5):643-652.

Singec I., Knoth R., Meyer R.P., Maciaczyk J., Volk B., Nikkhah G., Frotscher M. & Snyder E.Y. (2006). Defining the actual sensitivity and specificity of the neurosphere assay in stem cell biology. Nat Methods. 3(10):801-806.

Singh S., Bray M.A., Jones T.R. & Carpenter A.E. (2014). Pipeline for illumination correction of images for high-throughput microscopy. J Microsc. 256(3):231-236.

Sirerol-Piquer M.S., Belenguer G., Morante-Redolat J.M., Duart-Abadia P., Perez-Villalba A. & Fariñas I. (2019). Physiological Interactions between Microglia and Neural Stem Cells in the Adult Subependymal Niche. Neuroscience. 405:77-91.

Smith K., Li Y., Piccinini F., Csucs G., Balazs C., Bevilacqua A. & Horvath P. (2015). CIDRE: an illumination-correction method for optical microscopy. Nat Methods. 12(5):404-406.

Smith K.J., Blakemore W.F. & McDonald W.I. (1979). Central remyelination restores secure conduction. Nature. 280(5721):395-396.

Snaidero N. & Simons M. (2014). Myelination at a glance. J Cell Sci. 127(Pt 14):2999-3004.

Snaidero N., Möbius W., Czopka T., Hekking L.H., Mathisen C., Verkleij D., Goebbels S., Edgar J., Merkler D., Lyons D.A. et al. (2014). Myelin membrane wrapping of CNS axons by PI(3,4,5)P3-dependent polarized growth at the inner tongue. Cell. 156(1-2):277-290.

Snijder B., Sacher R., Rämö P., Damm E.M., Liberali P. & Pelkmans L. (2009). Population context determines cell-to-cell variability in endocytosis and virus infection. Nature. 461(7263):520-523.

Snijder B., Sacher R., Rämö P., Liberali P., Mench K., Wolfrum N., Burleigh L., Scott C.C., Verheije M.H., Mercer J. et al. (2012). Single-cell analysis of population context advances RNAi screening at multiple levels. Mol Syst Biol. 8:579.

Sohn J., Orosco L., Guo F., Chung S.H., Bannerman P., Mills Ko E., Zarbalis K., Deng W. & Pleasure D. (2015). The subventricular zone continues to generate corpus callosum and rostral migratory stream astroglia in normal adult mice. J Neurosci. 35(9):3756-3763.

Spencer S.L., Cappell S.D., Tsai F.C., Overton K.W., Wang C.L. & Meyer T. (2013). The proliferation-quiescence decision is controlled by a bifurcation in CDK2 activity at mitotic exit. Cell. 155(2):369-383.

Steyer A.M., Ruhwedel T. & Möbius W. (2019). Biological Sample Preparation by High-pressure Freezing, Microwave-assisted Contrast Enhancement, and Minimal Resin Embedding for Volume Imaging. J Vis Exp. (145):10.3791/59156.

Stringer C., Wang T., Michaelos M. & Pachitariu M. (2021). Cellpose: a generalist algorithm for cellular segmentation. Nat Methods. 18(1):100-106.

Tajima R. & Kato Y. (2011) Comparison of threshold algorithms for automatic image processing of rice roots using freeware ImageJ. Field Crop Res. 121:460-463.

Tang, D., Kang, R., Berghe, T.V., Vandenabeele P. & Kroemer G. (2019). The molecular machinery of regulated cell death. Cell Res. 29:347-364.

Tavazoie M., Van der Veken L., Silva-Vargas V., Louissaint M., Colonna L., Zaidi B., Garcia-Verdugo J.M. & Doetsch F. (2008): A specialized vascular niche for adult neural stem cells. Cell Stem Cell. 3(3):279-288.

Taylor D.L., Woo E.S. & Giuliano K.A. (2001). Real-time molecular and cellular analysis: the new frontier of drug discovery. Curr Opin Biotechnol. 12(1):75-81.

Tinevez J.Y., Perry N., Schindelin J., Hoopes G.M., Reynolds G.D., Laplantine E., Bednarek S.Y., Shorte S.L. & Eliceiri K.W. (2017). TrackMate: An open and extensible platform for single-particle tracking. Methods. 115:80-90.

Towne D.L., Nicholl E.E., Comess K.M., Galasinski S.C., Hajduk P.J. & Abraham V.C. (2012). Development of a high-content screening assay panel to accelerate mechanism of action studies for oncology research. J Biomol Screen. 17(8):1005-1017.

Tripathi R.B., Rivers L.E., Young K.M., Jamen F. & Richardson W.D. (2010). NG2 glia generate new oligodendrocytes but few astrocytes in a murine experimental autoimmune encephalomyelitis model of demyelinating disease. J Neurosci. 30(48):16383-16390.

Van Rossum G. & Drake F. L. (2009). Python 3 Reference Manual. Scotts Valley, CA: CreateSpace.

Van Valen D.A., Kudo T., Lane K.M., Macklin D.N., Quach N.T., DeFelice M.M., Maayan I., Tanouchi Y., Ashley E.A. & Covert M.W. (2016). Deep learning automates the quantitative analysis of individual cells in live-cell imaging experiments. PLoS Comput Biol. 12:e1005177.

Wachs F.P., Couillard-Despres S., Engelhardt M., Wilhelm D., Ploetz S., Vroemen M., Kaesbauer J., Uyanik G., Klucken J., Karl C. et al. (2003). High efficacy of clonal growth and expansion of adult neural stem cells. Lab Invest. 83(7):949-962.

Wang Y.Y., Sun Y.N., Lin C.C. & Ju M.S. (2012). Segmentation of nerve fibers using multi-level gradient watershed and fuzzy systems. Artif Intell Med. 54(3):189-200.

Watanabe M., Toyama Y. & Nishiyama A. (2002). Differentiation of proliferated NG2-positive glial progenitor cells in a remyelinating lesion. J Neurosci Res. 69(6):826-836.

Waters J.C. (2009). Accuracy and Precision in Quantitative Fluorescence Microscopy. J Cell Biol. 185(7):1135-1148.

Weigert M., Schmidt U., Boothe T., Müller A., Dibrov A., Jain A., Wilhelm B., Schmidt D., Broaddus C., Culley S. et al. (2018). Content-aware image restoration: pushing the limits of fluorescence microscopy. Nat Methods. 15(12):1090-1097.

Weigert M., Schmidt U., Haase R. & Sugawara K. & Myers G. Star-convex Polyhedra for 3D Object Detection and Segmentation in Microscopy. The IEEE Winter Conference on Applications of Computer Vision (WACV), Snowmass Village, Colorado, March 2020.

Weiss S., Dunne C., Hewson J., Wohl C., Wheatley M., Peterson A.C. & Reynolds B.A. (1996). Multipotent CNS stem cells are present in the adult mammalian spinal cord and ventricular neuroaxis. J Neurosci. 16(23):7599-7609.

Wilkinson M.D., Dumontier M., Aalbersberg I.J., Appleton G., Axton M., Baak A., Blomberg N., Boiten J.W., da Silva Santos L.B., Bourne P.E. et al. (2016). The FAIR Guiding Principles for scientific data management and stewardship. Sci Data. 3:160018.

Williams E., Moore J., Li S.W., Rustici G., Tarkowska A., Chessel A., Leo S., Antal B., Ferguson R.K., Sarkans U. et al. (2017). The Image Data Resource: A Bioimage Data Integration and Publication Platform. Nat Methods. 14(8):775-781.

Wolff C., Tinevez J.Y., Pietzsch T., Stamataki E., Harich B., Guignard L., Preibisch S., Shorte S., Keller P.J., Tomancak P. et al. (2018). Multi-view light-sheet imaging and tracking with the mamut software reveals the cell lineage of a direct developing arthropod limb. eLife 7:e34410.

Xing F., Xie Y. & Yang L. (2016). An automatic learning-based framework for robust nucleus segmentation. IEEE Trans Med Imaging. 35:550–566.

Xing Y.L., Röth P.T., Stratton J.A., Chuang B.H., Danne J., Ellis S.L., Ng S.W., Kilpatrick T.J. & Merson T.D. (2014). Adult neural precursor cells from the subventricular zone contribute significantly to oligodendrocyte regeneration and remyelination. J Neurosci. 34(42):14128-14146.

Yin C., Fufa T., Chandrasekar G., Aeluri M., Zaky V., Abdelhady S., Rodríguez A.B., Jakobsson J., Varnoosfaderani F.S., Mahalingam J. et al. (2017). Phenotypic Screen Identifies a Small Molecule Modulating ERK2 and Promoting Stem Cell Proliferation. Front Pharmacol. 8:726.

Zaimi A., Duval T., Gasecka A., Côté D., Stikov N. & Cohen-Adad J. (2016). AxonSeg: Open Source Software for Axon and Myelin Segmentation and Morphometric Analysis. Front Neuroinform. 10:37.

Zaimi A., Wabartha M., Herman V., Antonsanti P.L., Perone C.S. & Cohen-Adad J. (2018). AxonDeepSeg: automatic axon and myelin segmentation from microscopy data using convolutional neural networks. Sci Rep. 8(1):3816.

Zawadzka M., Rivers L.E., Fancy S.P., Zhao C., Tripathi R., Jamen F., Young K., Goncharevich A., Pohl H., Rizzi M. et al. (2010). CNS-resident glial progenitor/stem cells produce Schwann cells as well as oligodendrocytes during repair of CNS demyelination. Cell

Stem Cell. 6(6):578-590.

Zhao C., Ma D., Zawadzka M., Fancy S.P., Elis-Williams L., Bouvier G., Stockley J.H., de Castro G.M., Wang B., Jacobs S. (2015). Sox2 Sustains Recruitment of Oligodendrocyte Progenitor Cells following CNS Demyelination and Primes Them for Differentiation during Remyelination. J Neurosci. 35(33):11482-11499.

Zhao X., Pan Z., Wu J., Zhou G. & Zeng Y. (2010). Automatic identification and morphometry of optic nerve fibers in electron microscopy images. Comput Med Imaging Graph. 34(3):179-184.

Zheng X., Lei Q., Yao R. Gong Y. & Yin Q. (2018). Image segmentation based on adaptive K-means algorithm. J Image Video Proc. https://doi.org/10.1186/s13640-018-0309-3

Resumen

C:85
M:61
Y: 0
K: 0

R: 0
G:102
B:255

ANTECEDENTES

La combinación sinérgica de métodos automatizados de captura y análisis de bioimagen está emergiendo como un enfoque de vanguardia para abordar muchas cuestiones biológicas. Sin embargo, hay muchos campos en los que estas técnicas aún no se implementan y, en cambio, todavía se basan en la inspección visual y el análisis manual, que inevitablemente limitan el rendimiento alcanzable y son más propensos a introducir el sesgo del investigador. Por lo tanto, aún queda un gran esfuerzo por hacer en la difusión del uso de tecnologías de bioimagen de vanguardia en los campos de las ciencias de la vida con una gran dependencia de métodos de microscopía. En la presente tesis, nuestro objetivo ha sido desarrollar y aplicar métodos de bioimagen automatizados al estudio del cerebro adulto, en particular en las áreas de estudio de la biología de las células madre neurales (NSC, del inglés *neural stem cells*) y el proceso de remielinización de axones.

Con respecto a las NSC, la zona subependimaria (SEZ, del inglés, *subependymal zone*) de los ventrículos laterales es el área neurogénica más extensa y activa en el cerebro mamífero adulto. En el nicho de la SEZ, las NSC coexistentes muestran estados proliferativos heterogéneos que pueden agruparse en dos condiciones principales, quiescencia o activación. Las NSCs activadas producen neuroblastos, que migran para integrarse como neuronas maduras en el bulbo olfatorio. El estudio de la biología de las NSC adultas, a pesar de alcanzar su mayor nivel de complejidad cuando se realiza *in vivo*, se basa en gran medida en ensayos *in vitro* que permiten una descomposición y manipulación mucho más fácil y versátil de las variables del sistema. El aislamiento y la expansión de NSCs de la SEZ de ratones adultos es posible en condiciones de cultivo definidas. Se induce un estado proliferativo mediante el crecimiento de células disgregadas en condiciones no adhesivas en presencia de factor de crecimiento de fibroblastos básico (bFGF) y / o factor de crecimiento epidérmico (EGF) como mitógenos. En estas condiciones, una pequeña población de células comienza a proliferar formando agregados clonales flotantes conocidos como neuroesferas. Las neuroesferas primarias se pueden disociar para subcultivar las células individuales obtenidas, propagando así el cultivo con la formación de neuroesferas secundarias. Además, cultivados sobre un sustrato adhesivo en presencia de suero, se pueden inducir la diferenciación de las NSCs. De este modo, los cultivos de neuroesferas se han convertido en una técnica central para el estudio de las NSC adultas en un entorno altamente controlado. En las últimas décadas se han desarrollado diferentes ensayos para evaluar específicamente sus propiedades básicas, que han permitido un gran avance en nuestro conocimiento sobre la

neurogénesis adulta y el mantenimiento y regeneración del tejido neural. No obstante, no se ha aprovechado el potencial de estos modelos *in vitro* en forma de rastreos a gran escala basados en microscopía. Por el contrario, la mayoría de los análisis actuales se realizan normalmente de forma manual o, como mucho, con la ayuda de software, pero dependiendo de la supervisión del investigador.

Por otro lado, los oligodendrocitos son las células mielinizantes del sistema nervioso central (CNS, del inglés *central nervous system*). Extienden sus procesos alrededor de los axones para formar la capa aislante rica en lípidos conocida como vaina de mielina, cuyas funciones principales son proporcionar apoyo metabólico a los axones subyacentes y potenciar la transmisión rápida de potenciales de acción a lo largo del axón. En el cerebro adulto, los oligodendrocitos mielinizantes maduros son generados por las células precursoras de oligodendrocitos (OPC, del inglés *oligodendrocyte precursor cells*) que residen en el parénquima cerebral y por las NSCs subependimarias. Para el estudio de la remielinización de axones se han desarrollado una serie de modelos *in vivo* que consisten en causar una lesión desmielinizante mediante la administración de toxinas para, más tarde, estudiar el proceso de la remielinización. El análisis de estos experimentos se ha basado clásicamente en la captura de imágenes de microscopía electrónica de alta resolución seguidas de anotación manual para la cuantificación. A lo largo de los años se han implementado algunos protocolos de análisis de bioimagen para cuantificar la envoltura de mielina por axón en la forma del parámetro conocido como *g-ratio*. Sin embargo, aunque algunos de ellos alcanzan cierto grado de automatización, su uso no se ha extendido entre los científicos. Además, todas estas herramientas se centran en el *g-ratio*, pero ninguna mide la lengua citoplásmica interna, un elemento clave en el proceso de (re)mielinización.

Este trabajo se ha realizado utilizando exclusivamente software de código abierto y gratuito. La base fundamental del software de código abierto es que su código está disponible públicamente, lo que encaja perfectamente con estándares de la ciencia como el método científico y la validación de resultados a través de un sistema de revisión por pares. En general, el trabajo se ha desarrollado principalmente en ImageJ/Fiji, uno de los softwares más populares para el análisis de imágenes científicas. Además también se han utilizado otros dos programas de código abierto. Por una parte, CellProfiler (en conjunto con CellProfiler Analyst), un software dedicado a la cuantificación de fenotipos celulares en rastreos de alto contenido utilizando imágenes de microscopía. Por otro lado ilastik, un programa que implementa una serie de flujos de trabajo de aprendizaje automático (ML, del inglés, *machine learning*).

HIPÓTESIS

Consideramos como hipótesis general que la aplicación de métodos de análisis de bioimagen y, cuando sea posible, la adopción de estrategias de rastreo basadas en microscopía, podrían beneficiar enormemente estos dos campos de estudio al aumentar tanto el rendimiento como la estandarización del análisis. Para abordar la hipótesis, seleccionamos escenarios específicos de diversa complejidad que combinaban una configuración experimental, adquisición de imágenes y desarrollo e implementación de estrategias de análisis de bioimagen.

OBJETIVOS

Teniendo en cuenta las consideraciones anteriores, los objetivos específicos que nos propusimos alcanzar fueron:

1. Implementar un ensayo de rastreo de alto rendimiento para la evaluación *in vitro* de las propiedades adhesivas y la regulación en cultivos 2D de NSCs.

2. Desarrollar un ensayo de rastreo de alto contenido para el análisis unicelular de la proliferación y apoptosis de NSCs en cultivos 2D.

3. Establecer un ensayo de rastreo de alto rendimiento para la evaluación de la autorrenovación y la capacidad clonal de NSCs a través del análisis poblacional de neuroesferas 3D.

4. Crear un flujo de trabajo semiautomático para mejorar el rendimiento del análisis de bioimagen de modelos de remielinización *in vivo* utilizando un parámetro novedoso en microscopía electrónica.

CAPÍTULO 1

Antecedentes biológicos

Las cadherinas son proteínas transmembrana de tipo 1 que establecen uniones adherentes homofílicas, célula-a-célula y dependientes del calcio a través de su dominio extracelular. Los miembros de esta familia de moléculas de adhesión celular desempeñan papeles críticos y variados durante el desarrollo y en la homeostasis adulta. Entre otras funciones, estas moléculas se han relacionado con la regulación del ciclo de activación de quiescencia en varios nichos de células madre. Nuestro laboratorio ha de-

mostrado que la adhesión de las NSC subependimarias a la capa ependimaria a través de N-cadherina (cadherina 2, Cdh2) contribuye a mantener la organización estructural del nicho neurogénico y regula la quiescencia de las NSC. Además, describimos que este papel es dinámico ya que la escisión regulada por N-cadherina por MT5-MMP, una metaloproteinasa de tipo membrana (MMP, del inglés *membrane-type metalloproteinase*), codificada por el gen *Mmp24*, promueve la activación de las NSCs en condiciones fisiológicas y regenerativas. Sin embargo, los mecanismos subyacentes a la quiescencia mediada por adhesión no se han dilucidado por completo. Por lo tanto, decidimos explorar la posible implicación en la regulación de la adhesión de las NSCs de otro miembro de la familia MMP, la adamlisina ADAM10. Esta shedasa, como otros miembros de ADAM, contiene dominios de desintegrina y metaloproteasa y se ha observado que escinde la N-cadherina en las neuronas. De hecho, es una de las proteasas más expresadas en el cerebro adulto, incluida la SEZ.

Con el fin de investigar los efectos y la regulación de la adhesión mediada por N-cadherina de las NSCs y caracterizar los factores de nicho secretados involucrados en su escisión, hemos desarrollado un ensayo funcional *in vitro* que modela el anclaje de células subependimarias mediadas por N-cadherina y automatizado su análisis mediante la adopción de una estrategia de captura de imágenes por rastreo y el desarrollo de una herramienta de análisis de bioimágenes para la extracción de los datos cuantitativos relevantes.

Configuración experimental y captura de imagen

Los ensayos de adhesión celular tienen como objetivo cuantificar el anclaje de células aisladas a superficies recubiertas con ligandos, componentes de la matriz extracelular purificados u otras células, generalmente en forma de monocapas. Para nuestro ensayo de rastreo basado en microscopía, con el fin de imitar en la medida de lo posible las condiciones *in vivo*, en lugar de utilizar una proteína recombinante purificada como recubrimiento, el sustrato adherente es proporcionado por una monocapa de células vivas que sobreexpresan el ligando de interés.

En primer lugar, las neuroesferas se someten a disgregación mecánica con el fin de preservar la integridad de los dominios extracelulares de N-cadherina, y se depositan en una monocapa confluente de fibroblastos NC-L929 que sobreexpresan N-cadherina. En caso de que las NSC interrogadas no sean intrínsecamente fluorescentes, se marcan con el trazador de células DDAO-SE para facilitar su detección. Además, para incluir un control de especificidad, parte de las células se incuban con el anticuerpo bloqueador de N-cadherina GC4 (NcadBlock) para reducir su adhesión mediada por N-cadherina. Una vez que se deja adherir durante un tiempo controlado, las células no adheridas se

lavan a fondo y los cultivos se fijan para un análisis adicional. Finalmente, los núcleos se marcan con DAPI para visualizar las células de la monocapa subyacente y las células se fijan para fotografiarlas mediante un microscopio de rastreo automático.

Para obtener datos cuantitativos del ensayo se deben realizar dos tareas diferentes: estimar el porcentaje de superficie de cultivo ocupada por la monocapa que expresa N-cadherina y detectar y contar el número de NSCs adheridas a ella. Dado que no se requiere una morfología celular precisa para lograr las tareas mencionadas, decidimos capturar imágenes de baja resolución. De hecho, las condiciones de obtención de imágenes se han configurado para llegar a un compromiso entre reducir el tamaño de la imagen al mínimo y aún poder detectar de manera eficiente los objetos de interés, lo cual supone un ahorro enorme de espacio al tratarse de un ensayo de rastreo de alto rendimiento. Concretamente, muestreamos las NSCs DDAO-SE^{+} con una longitud mínima de 5 a 10 píxeles. Tanto los parámetros de captura como los de análisis de imagen de nuestro protocolo están ajustados para trabajar fotografiar y analizar objetos en este rango de tamaño.

Análisis de bioimagen

Hemos desarrollado un flujo de trabajo de análisis de bioimagen que se ha automatizado en una macroinstrucción de ImageJ. Además, dada la importancia del tamaño de los objetos para la aplicación de esta herramienta, junto a ella proporcionamos otra macroinstrucción que permite disminuir el tamaño de las imágenes agrupando píxeles en cuadrados de 2x2, 3x3 o 4x4 que toman el valor de la media de todos los píxeles del conjunto.

Una vez las imágenes tienen una resolución adecuada se puede iniciar el flujo de trabajo principal. Dado que es probable que sea necesario ajustar el conjunto de parámetros entre análisis, la macro permite modificar la configuración para adaptarse al análisis de diferentes experimentos. De hecho, la macro incluye un modo de prueba, que permite al usuario modificar los parámetros y verificar el resultado fácilmente antes de lanzar el análisis. Además, el conjunto de parámetros se puede guardar e importar en análisis futuros.

Para favorecer el análisis no supervisado hemos incluido la medición de diferentes métricas para ser aplicadas en controles de calidad. Nuestro control de calidad está destinado a detectar dos tipos diferentes de imágenes inadecuadas: aquellas que están desenfocadas o contienen artefactos saturados, y aquellas que, a pesar de ser adecuadas en términos de adquisición de imágenes, contienen una monocapa incompleta. Tal y como se ha descrito previamente, el objetivo principal del ensayo es cuantificar

el número de células adheridas por superficie de monocapa. Para contar el número de células adheridas, la imagen correspondiente al trazador DDAO-SE se suaviza antes de determinar las posiciones de los máximos de intensidad locales. Estos máximos se utilizan como marcadores para separar la imagen en territorios de Voronoi. Además, se aplica una segmentación por umbrales para generar una máscara binaria que puede contener varias células fusionadas en un único objeto. Estos objetos son separados utilizando operadores lógicos con los territorios de Voronoi y, finalmente, los píxeles aislados y otros objetos demasiado pequeños para ser células son eliminados de la imagen binaria. Por lo que respecta a la monocapa, dado que se ha utilizado DAPI para marcar el ADN de las células, el área de la monocapa debe estimarse a partir de los núcleos de los fibroblastos. Para ello se aplica el filtro del máximo para "rellenar" los espacios de fondo que quedan entre núcleos cercanos. A continuación, se aplica una segmentación por umbrales para obtener una segmentación semántica de la monocapa. Una vez obtenidas las máscaras binarias de las células adheridas y la monocapa se utilizan para calcular el número de células adheridas y la superficie que ocupa la monocapa.

Estudio: regulación de la proteólisis de N-cadherina en la SEZ por factores de nicho

Dado que algunos de nuestros resultados preliminares *in vivo* sugerían que ADAM10 también podría estar involucrado en la escisión de la N-cadherina presente en la membrana NSC, aplicamos nuestra estrategia para abordar cuantitativamente el papel de ADAM10 en la regulación de la adhesión de las NSCs mediada por N-cadherina. Para ello, los cultivos de neuroesferas se trataron previamente con GI254023X (GIX), un potente fármaco inhibidor de ADAM10. Antes de realizar el protocolo de adhesión celular también se incluyó un control de especificidad con anticuerpos NcadBlock: la mitad de las células se incubaron con NcadBlock y la otra mitad con inmunoglobulinas de isotipo de ratón (IsoMsIgG). Tras el tratamiento, las NSCs (marcadas con DDAO-SE) se sembraron en la monocapa NC-L929 y se dejaron adherir durante un tiempo determinado antes de lavar las células no adheridas, fijarlas y teñirlas con DAPI para su posterior captura y análisis.

Tal y como se esperaba, el NcadBlock redujo consistentemente la adhesión de las NSCs a la monocapa NC-L929. Con respecto a la condición experimental, en caso de que ADAM10 realmente participe en la proteólisis y el desprendimiento de la N-cadherina en las NSC, su inhibición debería provocar un incremento en los niveles de N-cadherina en la superficie celular y, por lo tanto, en una mayor adhesión. Esto fue confirmado en nuestro ensayo, ya que la condición tratada con GIX mostró un mayor recuento de células DDAO-SE-positivas adheridas por área de monocapa.

CAPÍTULO 2

Antecedentes biológicos

La proliferación celular y la muerte celular programada son sin duda dos de los procesos más estudiados en el campo de la biología celular. En el campo de las células madre en particular, la regulación del ciclo celular es fundamental para comprender las propiedades clave de las células madre, como su mantenimiento a través de la transición reversible entre la quiescencia y la activación o el cambio de la pluripotencia a la diferenciación. La apoptosis, por otro lado, ha surgido en los últimos años como un tema importante en el estudio de las células madre, ya que se ha encontrado que los cuerpos apoptóticos de las células circundantes pueden inducir la proliferación de células madre o que mediadores apoptóticos específicos pueden desempeñar un papel en la diferenciación de las células madre.

Entre los métodos adecuados para evaluar la proliferación celular mediante análisis microscópico, los experimentos de pulso y caza con análogos de nucleósidos destacan por su fiabilidad y aplicabilidad en ensayos de rastreo. Este enfoque se basa en la detección de nucleósidos trazables incorporados al ADN mientras las células pasan por la fase S del ciclo celular. Para ello, las células se incuban con pirimidinas modificadas, que actúan como análogos de timidina, durante un breve período de tiempo (pulso). Después de eso, las células se pueden fijar y procesar inmediatamente para la detección del ADN marcado, lo que proporciona una estimación de la proliferación general en la muestra (caza).

Las pirimidinas que contienen halógenos, como BrdU (5-bromo-2′-desoxiuridina) se han utilizado durante décadas con este objetivo, lo que requiere la desnaturalización del ADN para revelar su presencia mediante inmunotinción con anticuerpos específicos. Por el contrario, la EdU (5-etinil-2′-desoxiuridina) puede detectarse directamente mediante una reacción "click" mediante la cual grupo alquino presente en la molécula de EdU forma un enlace covalente con una azida ligada a un fluoróforo, haciendo innecesario el uso de anticuerpos o el desenmascaramiento de antígenos por tratamiento térmico o ácido. Por esta y otras ventajas, EdU se ha convertido en los últimos años en una alternativa popular para los ensayos de rastreo.

La apoptosis es una forma de muerte celular provocada por la activación de cascadas proteolíticas altamente reguladas y con características bioquímicas y morfológicas estereotipadas. Los procesos apoptóticos se dividen en dos subtipos principales, apoptosis intrínseca o extrínseca, según las vías bioquímicas implicadas en su regulación. Por un lado, la apoptosis intrínseca depende de la permeabilización de la membrana

externa mitocondrial, liberando proteínas mitocondriales que son responsables de la activación de la caspasa iniciadora 9. Por otro lado, la apoptosis extrínseca está mediada por dos tipos diferentes de receptores de membrana: la presencia de ligandos de receptores de muerte conduce a la activación de las caspasas iniciadoras 8 y 10, mientras que la ausencia de ligandos de receptores de dependencia conduce a la activación de la caspasa iniciadora 9.

Las caspasas ejecutoras 3, 6 y 7 son efectores comunes tanto para la vía intrínseca como extrínseca, y son escindidas por las caspasas 8, 9 o 10 para iniciar la apoptosis. Debido a su papel central en las vías de señalización de la apoptosis, los efectores comunes como las caspasa 3 y 7 son biomarcadores bien establecidos para la detección de células apoptóticas y pueden detectarse fácilmente en los núcleos mediante inmunoquímica mediante una gran variedad de anticuerpos disponibles comercialmente que distinguen específicamente la forma activada de cada caspasa de su cimógeno pro-caspasa.

Análisis de bioimagen

Hemos desarrollado un flujo de trabajo de análisis de bioimagen para analizar un rastreo de alto contenido para la evaluación de la proliferación celular y la apoptosis. A pesar de que el flujo de trabajo se ha ensamblado en una sola macroinstrucción de ImageJ, se han diseñado flujos de trabajo adicionales para realizar pasos de preprocesamiento opcionales. Además, igual que en el capítulo anterior, este flujo de trabajo también incluye un modo pre-análisis para testar los parámetros ajustables y visualizar el resultado.

Dado que el ensayo se basa en datos densitométricos, es necesario tener en cuenta que las imágenes adquiridas a través de un microscopio óptico se ven afectadas por el viñeteado, que se estima que causa una variación en la iluminación efectiva del 10-30% entre las diferentes regiones de la imagen. Para mejorar la calidad de los datos, es posible corregir las imágenes experimentales en un paso de preprocesamiento o determinar una región con una variación de iluminación mínima para excluir el resto del análisis. El flujo de trabajo incluye un paso opcional destinado a corregir la iluminación irregular utilizando la plugin BaSiC, un método retrospectivo que utiliza múltiples imágenes aprovechando la gran cantidad de imágenes que se generan en un ensayo de rastreo.

El ensayo computa datos densitométricos de diferentes sondas fluorescentes que marcan moléculas localizadas total o parcialmente en los núcleos celulares pero que muestran diversos patrones de tinción. En consecuencia, la segmentación se realiza en el canal de la tinción nuclear (p.ej., DAPI). Para lograr una segmentación de núcleos precisa, el usuario puede elegir entre dos estrategias diferenciadas. Por un lado, un flu-

jo de trabajo basado en métodos clásicos de procesamiento de imágenes que incluye algunos de los pasos más habituales en este tipo de estrategias (filtros de suavizado, métodos de segmentación por umbrales y operaciones de morfología matemática). Por otro lado, un enfoque de aprendizaje profundo (DL, del inglés, *deep learning*) utilizando el modelo versátil (núcleos fluorescentes) de StarDist. StarDist predice la probabilidad de cada píxel de ser parte de un objeto y la distancia al límite del objeto a lo largo de una serie de direcciones radiales. de este modo, se propone un polígono de forma estrellada-convexa como región candidata por cada píxel dentro de un objeto, lo que genera una gran cantidad de formas redundantes que luego se filtran usando supresión no máxima para podar aquellas regiones que probablemente correspondan al mismo objeto. Para utilizar StarDist hemos adaptado nuestro protocolo de captura de imagen, de modo que la resolución obtenida es la más adecuada para aplicar este método.

El uso de microscopios de alto rendimiento permite la adquisición de un gran conjunto de datos de forma automatizada. A pesar de sus ventajas, el enfoque automático también puede conducir a la captura de imágenes de mala calidad. Dado que el análisis de dichos rastreos imposibilita la inspección visual de las imágenes es necesario aplicar métodos para la identificación automática y la exclusión de esas imágenes a fin de evitar una interpretación errónea de los resultados. Dado que se han propuesto muchos parámetros para la detección de imágenes desenfocadas, decidimos entrenar un clasificador utilizando métodos de ML en CellProfiler Analyst. Para aumentar el número de imágenes desenfocadas para el entrenamiento y la validación del método se capturaron dos conjuntos de imágenes adicionales: uno de imágenes ligeramente desenfocadas y otro de campos de visión afectados severamente. Los resultados demostraron la gran exactitud del método utilizando un único parámetro, el *power log-log slope*.

Estudio: respuesta de las NSCs al daño del ADN

El funcionamiento del flujo de trabajo se probó en un rastreo real de proliferación celular (mediante un pulso corto de EdU) y apoptosis (mediante detección de caspasa 3 activada por inmunocitoquímica). Seleccionamos una estrategia que combinaba funciones de corrección de la iluminación calculadas con BaSiC y segmentación de los núcleos con StarDist. El objetivo del ensayo era evaluar la respuesta de las NSC al daño del ADN *in vitro*, que fue inducido por una breve exposición al agente alquilante metil metanosulfonato (MMS). En concreto, las células se expusieron a una concentración baja (0,005%) o alta (0,02%) de MMS.

Tal y como se esperaba, los efectos del tratamiento sobre la proliferación celular fueron dramáticos. Mientras que un MMS bajo condujo a una disminución importante en

las células positivas para EdU, un MMS alto provocó una detención completa del ciclo celular. Además, observamos una caída evidente de la intensidad media y los valores de densidad integrados del canal EdU en las células EdU^+ tratadas con MMS bajo. Además, se estratificaron las células de la muestra en cinco grupos (C1-5), asignando las células EdU^- a C1 mientras que las EdU^+ se distribuyeron entre los cuatro grupos restantes de acuerdo con su señal (C2 a C5 de menor a mayor intensidad). De este modo se observó que las células proliferantes en condición de MMS baja se asignaron preferentemente en C2, muy probablemente debido a la interrupción transitoria de la fase S. Respecto a la apoptosis, se trata de un fenómeno extremadamente raro en NSCs cultivadas en condiciones regulares *in vitro*, por lo que a pesar de que un MMS provocó un aumento importante la tasa de apoptosis más alta no superó el 0,4%

CAPÍTULO 3

Antecedentes biológicos

Una de las características definitorias de las NSCs es su capacidad clonal y de autorrenovación. El desarrollo de cultivo *in vitro* de estas células madre ha permitido la evaluación de sus características definitorias. Tanto la evaluación de la clonalidad como la autorrenovación se basan en la formación controlada de agregados clonales flotantes conocidos como neuroesferas durante el denominado "ensayo de formación de neuroesferas". El ensayo se inicia con la obtención de células individuales a partir de la disección y disociación del tejido SEZ o de la disgregación de neuroesferas previamente formadas. Luego, estas células se siembran a una densidad celular estandarizada en placas multipocillo en un medio definido sin suero y suplementado con mitógenos. Después de varios días, el número de neuroesferas formadas define la capacidad clonal del cultivo, mientras que su disgregación y resiembra en rondas posteriores de formación de neuroesferas proporciona información sobre su autorrenovación.

Los ensayos de una sola célula aseguran la densidad clonal verdadera, ya que se realizan cultivando células individuales de forma independiente, es decir, sembrando solo una célula por pocillo. Sin embargo, los procedimientos para lograr esto no siempre son fáciles y pueden perjudicar la viabilidad celular. Una alternativa interesante son los ensayos de muy baja densidad (ensayo pseudo-clonal), que también pueden generar resultados consistentes. Nuestro laboratorio y otros han demostrado que una densidad celular de menos de 5 NSC por µL (hasta 1000 células por pocillo en una placa convencional de 96 pocillos) permite la formación reproducible de neuroesferas clonales a partir de células individuales sin signos de agregación. El objetivo de este ensayo

es cuantificar el número de neuroesferas formadas, generalmente después de 5-7 días, en relación al número de células sembradas.

El procedimiento para cuantificar el resultado de los ensayos de neuroesferas ha sido típicamente la observación directa de la placa de cultivo a través de un microscopio invertido de contraste de fase, por lo que los investigadores obtienen el número de agregados clonales mediante inspección visual mientras se desplazan manualmente a través de la placa. Además de ser tedioso y lento, especialmente en experimentos con varias réplicas técnicas y biológicas y condiciones experimentales, requiere un cierto entrenamiento y puede verse afectado por el sesgo del investigador. En algunos paradigmas experimentales, además del número de clones, el tamaño de las neuroesferas formadas también podría ser informativo y ayudar a caracterizar un fenotipo particular. Esta medida no se puede obtener directamente durante el recuento manual de neuroesferas, sino que es necesario capturar imágenes representativas de la superficie de cultivo y medir el tamaño de las neuroesferas muestreadas.

Configuración experimental y captura de imagen

Para nuestro ensayo elegimos un enfoque pseudo-clonal porque es mucho más fácil de realizar a diario en un laboratorio de cultivo celular normal. Sin embargo, con el fin de optimizar el análisis y permitir la evaluación simultánea y automática tanto del número como del tamaño de las neuroesferas, decidimos desarrollar un protocolo de captura de imágenes similar a un rastreo de alto contenido al que le sigue un flujo de trabajo de análisis de bioimagen automático. Dado que las neuroesferas no se distribuyen de manera heterogénea a lo largo del pocillo decidimos capturar una cuadrícula ordenada de 5x5 imágenes parcialmente superpuestas cubriendo toda la superficie del pocillo, lo que permite combinarlas más tarde para obtener una reconstrucción completa. Por otro lado, al tratarse de agregados tridimensionales, encontrar un plano focal apropiado para obtener una imagen representativa enfocada de todas las neuroesferas en el pocillo no es una tarea fácil. De hecho, el software de enfoque automático que se aplica normalmente para encontrar células adheridas al fondo del pocillo falla en gran medida al intentar enfocar las neuroesferas. Por lo tanto, nuestro protocolo de imágenes se basa en la información proporcionada por el operador para establecer el mejor plano focal posible.

Análisis de bioimagen

Hemos desarrollado un flujo de trabajo de análisis de bioimagen para el ensayo de neuroesfera pseudo-clonal. El flujo de trabajo se ha automatizado mediante varias macroinstrucciones de ImageJ combinadas con un clasificador entrenado en ilastik. En

este caso no se ha incluído un modo pre-análisis, pues el flujo de trabajo requiere más tiempo para procesar pocillos enteros. Por el contrario, se ha implementado una macroinstrucción adicional en la que se pueden probar con mayor eficiencia los parámetros de la segmentación en las imágenes de los pocillos una vez han sido reconstruidos.

Capturar toda el área de cultivo de un pocillo redondo en una placa multipocillo de plástico transparente mediante una cuadrícula de imágenes cuadradas conlleva algunos problemas para el análisis de bioimagen. Destaca la iluminación desigual introducida por la pared del pocillo, que refleja la luz. De hecho, este fenómeno es tan prominente que enmascara la típica iluminación irregular que afecta a cualquier imagen obtenida con un microscopio. Para hacer frente a esto, en primer lugar se preprocesan las imágenes del experimento para corregir la iluminación no uniforme. Al contrario que en el capítulo 2, la iluminación es diferente en cada campo de visión, según su posición respecto a la pared del pocillo. Por esta razón se ha implementado una macroinstrucción que utiliza BaSiC para generar una función de corrección para cada uno de los 25 campos de visión que conforman un pocillo.

Dado que los microscopios de alto contenido no suelen utilizar contraste de fase, es probable que las neuroesferas se detecten mejor debido a su textura más que a sus intensidades absolutas. Por lo tanto, decidimos aplicar una estrategia de ML en ilastik para facilitar la segmentación semántica de varios componentes de la imagen (fondo, neuroesferas y bordes del pocillo) mediante la clasificación de píxeles. El clasificador está integrado en la macroinstrucción de ImageJ, en el que genera un mapa de probabilidades como un paso intermedio del flujo de trabajo. A continuación se reconstruyen los pocillos (tanto las imágenes de luz transmitida como los mapas de probabilidades) utilizando el algoritmo de "costura" incluido en el núcleo de Fiji.

El objetivo principal del ensayo es contar el número de neuroesferas y medir su tamaño. Una vez reconstruidos los pocillos, la segmentación se realiza en los mapas de probabilidad generados, que son procesados mediante una estrategia basada en el uso de filtros. La imagen de probabilidad de neuroesferas se procesa para segmentar los agregados clonales. Además, el mapa de probabilidad de las paredes se invierte y para definir el área correspondiente a la superficie de cultivo del pocillo.

Estudio: comparación entre los clasificadores propuestos para la segmentación de las neuroesferas

Dado que probamos cuatro clasificadores diferentes, cada uno basado en un número diferente de características, decidimos comparar su funcionamiento en la segmentación de objetos. Para ello, ejecutamos el flujo de trabajo previamente descrito aplican-

do cada uno de los cuatro clasificadores pero manteniendo constante el conjunto de parámetros ajustables. Además, un experto anotó manualmente todas las neuroesferas en las imágenes reconstruidas del canal de luz transmitida. Luego, comparamos las segmentaciones obtenidas a través de nuestro flujo de trabajo de análisis de bioimagen aplicando los cuatro clasificadores con las anotaciones de referencia anotadas manualmente. Con este objetivo, utilizamos el parámetro F1 para evaluar el rendimiento de la segmentación, para lo que implementamos una macro de Fiji. Esto nos permitió identificar el mejor clasificador, cuyo resultado fue comparado también con el obtenido al enfrentar las anotaciones del primer experto con las generadas por un segundo anotador. De este modo demostramos que nuestro flujo de trabajo automatizado genera resultados tan precisos como los anotados manualmente por investigadores.

CAPÍTULO 4

Antecedentes biológicos

Los oligodendrocitos en el CNS envuelven sus proyecciones citoplasmáticas especializadas alrededor de los axones para formar la estructura de recubrimiento conocida como vaina de mielina. Las OPCs son las encargadas de dar lugar a oligodendrocitos mielinizantes, tanto durante el desarrollo embrionario que conduce al proceso de mielinización como en respuesta a una lesión o en el caso de patología desmielinizante durante el proceso de remielinización. Debido a la innegable importancia de estos dos procesos, los científicos han buscado enfoques para cuantificar los cambios en el grosor de la vaina de mielina para ayudar a comprender su biología en condiciones fisiológicas y patológicas. Existe un método generalizado que se ha convertido en un estándar del campo, el parámetro conocido como *g-ratio*, definido en el campo como la relación entre el diámetro del axón y el diámetro de la fibra. Según esta definición, cuanto más gruesa es la vaina de mielina, menor es el *g-ratio*, que es igual a uno en ausencia de mielina. Con respecto a la evaluación de la remielinización, las áreas sometidas a un proceso de remielinización se distinguen típicamente por sus vainas de mielina más delgadas, es decir, *g-ratios* más bajos.

Durante la mielinización, los axones del CNS son cubiertos de forma discontinua por oligodendrocitos que albergan proteínas especializadas transmembrana y asociadas a la membrana que confieren a la mielina la mayoría de sus propiedades. Para hacerlo, estas células emiten procesos citoplasmáticos que son guiados para alcanzar el axón, mantener un contacto estrecho y envolverlo para formar la cubierta celular multicapa y concéntrica conocida como vainas de mielina. El engrosamiento de la mielina se debe a

la envoltura de la lengua citoplásmica interna alrededor del axón al avanzar por debajo de la envoltura preformada. La compactación de la mielina comienza tras las primeras envolturas y es impulsada por la proteína básica de mielina (MBP, del inglés *myelin basic protein*) asociada a la membrana. De hecho, el crecimiento de la membrana y la compactación de la mielina tienen lugar de una manera coordinada, con lo que la compactación se da primero en las envolturas de membrana más externas, evitando la compactación de la zona de crecimiento más interna. Luego, la compactación se extiende progresivamente hacia el interior, siempre a la zaga de la región de crecimiento. Durante la mielinización, la lengua interna se agranda y es rica en F-actina. No obstante, a medida que la mielina madura, la lengua se estrecha y la actina F disminuye. Una vez que se completa la mielinización activa, queda una lengua interna de mielina sin compactar, generalmente encogida. De hecho, las fibras adultas del CNS aún conservan el citoplasma no compactado en los extremos de la espiral de mielina, es decir, las lenguas interna y externa.

Sorprendentemente, a pesar de la importancia de la lengua interna en el proceso de mielinización, se ha ignorado durante mucho tiempo al evaluar las propiedades de la mielina. De hecho,el *g-ratio* no la tiene en cuenta. De hecho, a pesar de la existencia de diversos métodos computacionales para la obtención del *g-ratio*, hasta ahora no se había desarrollado ninguno para la segmentación de la lengua interna. Por esa razón decidimos implementar un flujo de trabajo que permitiese calcular el *g-ratio* tradicional, pero también obtener medidas teniendo en cuenta este componente de la fibra.

Análisis de bioimagen

A diferencia de otros enfoques destinados a permitir el análisis de imágenes adquiridas a través de una amplia gama de técnicas de imagen, nuestro objetivo es poder segmentar la lengua interna. De hecho, nuestro enfoque permite la segmentación semiautomática de los tres componentes principales de la fibra: axoplasma, lengua interna y mielina, siempre que las imágenes muestren la lengua interna con suficiente detalle. Por lo tanto, nos enfocamos en imágenes TEM. Nuestra estrategia se basa en métodos de ML supervisados implementados en ilastik para mejorar la segmentación y combina el procesamiento automatizado de imágenes con etapas interactivas de edición del usuario.

Los pasos iniciales del flujo de trabajo se realizan en ilastik que, a diferencia de Fiji, reconoce un número limitado de formatos de imagen. Por esta razón decidimos incluir un paso opcional para convertir las imágenes en un formato compatible con ilastik. Además, este flujo de trabajo también permite aplicar algunos ajustes básicos

que pueden ser útiles para preprocesar las imágenes con el fin de utilizar un clasificador de ilastik generado previamente, por ejemplo, normalizando las imágenes. Una vez preprocesadas, un clasificador de píxeles entrenado en ilastik se aplica para generar mapas de probabilidad con tres clases diferentes: mielina, citoplasma y membrana. A continuación, la probabilidad del citoplasma se utiliza para generar una segmentación de instancias, a las que se les asignan clases diferentes (axoplasma o lengua de mielina) utilizando un clasificador de objetos entrenado en ilastik.

Los resultados obtenidos en ilastik se utilizan para realizar la segmentación secuencial de: i) el objeto definido por el límite interno de mielina, es decir, el axoplasma más la lengua interna, ii) toda la fibra (axoplasma + lengua interna + mielina compacta) y iii) solo el axoplasma sin ninguna estructura derivada de oligodendrocitos. Finalmente, trabajando con estas regiones será posible estimar automáticamente el grosor de la mielina, el área interna de la lengua o el diámetro del axón, entre muchos otros parámetros. No obstante, a pesar del uso de métodos de ML, la complejidad de las imágenes TEM aún dificulta la generación de una segmentación automática perfecta. Por lo tanto, decidimos implementar un flujo de trabajo semiautomático en el que la macroinstrucción de ImageJ obtiene automáticamente las ROIs correspondientes y luego se detiene, lo que permite al usuario verificar la selección y, si es necesario, editarla antes de pasar a la siguiente fase. La macroinstrucción sugiere posibles mejoras que pueden ser fácilmente aplicadas por el usuario. Alternativamente, el usuario es libre de utilizar la herramienta de selección a mano alzada de ImageJ para mejorar la selección.

Antes de medir y generar la tabla de resultados la macro incluye varios pasos automatizados destinados a: i) verificar las enmiendas manuales introducidas por el usuario y corregir errores comunes de la edición manual e ii) asociar los objetos pertenecientes a la misma fibra mediante un código de tres dígitos para permitir un análisis integral.

Estudio: evaluación de la segmentación de la fibra, el límite interno de la mielina y el axoplasma en imágenes de TEM.

Para evaluar cuantitativamente el rendimiento del flujo de trabajo, comparamos la segmentación obtenida utilizando la macro descrita en este capítulo con anotaciones manuales de un experto. La evaluación se realizó en imágenes TEM diferentes a las utilizadas para entrenar a los clasificadores. Las imágenes de TEM *in vivo* se obtuvieron de áreas remielinizantes del *corpus callosum* previamente sometidas a una lesión de desmielinización mediante la inyección de la toxina lisofosfatidilcolina. Para evaluar el impacto de la supervisión se generaron dos segmentaciones diferentes: i) una de manera completamente automatizada y, ii) otra semiautomática, incluyendo los pasos

supervisados por el usuario, pero evitando el uso de la herramienta de selección a mano alzada para la edición de ROIs.

El enfoque automatizado demostró una capacidad considerable para predecir los componentes de la fibra, siendo la fibra el objeto que el método parece identificar mejor. Además, como era de esperar, estos resultados se pueden mejorar significativamente al permitir al usuario revisar y modificar los objetos segmentados, incluso con la limitación de no permitir dibujar ROIs con la herramienta de selección a mano alzada.

CONCLUSIONES

1. El desarrollo de métodos de captura y análisis de imagen automatizados para el estudio de cultivos de NSCs mejora el rendimiento y la reproducibilidad de los ensayos *in vitro*.

2. La configuración experimental propuesta y la estrategia de análisis para el ensayo estático de alto rendimiento basado en la adhesión célula-a-célula es un modelo *in vitro* fiable para la evaluación del anclaje mediado por N-cadherina de NSCs aisladas.

3. Se pueden identificar diversos patrones de proliferación y viabilidad celular mediante métodos de rastreo de alto contenido en ensayos de proliferación celular y apoptosis.

4. El uso de colecciones de imágenes fuera de foco facilita el entrenamiento de clasificadores ML para la detección de campos de visión afectados por el desenfoque.

5. El análisis de bioimagen automatizado de ensayos pseudoclonales de formación de neuroesferas capturados en 2D genera datos tan precisos como los anotados en humanos.

6. La segmentación asistida por ML y supervisada por humanos de secciones transversales de fibras axonales en imágenes de TEM permite la extracción de parámetros clásicos y novedosos (basados en la lengua interna) para el estudio de la (re)mielinización y mejora el rendimiento del análisis de bioimagen.